A&A manuscript no.
(will be inserted by hand later)

Your thesaurus codes are:
04(03.20.4;04.19.1;08.04.1;09.04.1;10.06.2;10.19.3)

ASTRONOMY
AND
ASTROPHYSICS
1.2.2008

A new optical reddening model for the Solar neighborhood

Galactic Structure through low-latitude starcounts from the Guide Star Catalogue

R. A. Méndez[1] **& W. F. van Altena**[2]

(1) European Southern Observatory, Karl-Schwarzschild-Straβe 2, D-85748, Garching b. München, Germany, Electronic mail: rmendez@eso.org
(2) Yale University Observatory, P.O. Box 208101, New Haven, CT 06520-8101, USA, Electronic mail: vanalten@astro.yale.edu

Received; accepted

Abstract. A new optical reddening model for the Solar neighborhood is presented. The model makes use of the large-scale properties of the dust layer in the Galaxy, and of the observed clumpiness in its distribution, and it is used to compute starcounts *in* the plane of the Galaxy, which are compared to the observed counts from the Guide Star Catalogue (GSC) for a few representative regions having a range of reddening values. These comparisons provide a good test case in a wide variety of conditions with regards to both the amount and distribution of the reddening material along the line-of-sight.

This is the first systematic study of low-Galactic latitude starcounts from the perspective of a Galactic structure and reddening model, and it is demonstrated that the model can be used to obtain meaningful starcount estimates in the plane of the Milky-Way.

We find that it is possible to predict starcounts in the range $8 \leq V < 13.7$ with a mean accuracy of 15% or better for total samples of several thousand stars at $|b| < 10^{\circ}$, and for total reddening at 1 kpc of up to $E(B-V) \sim 0.7$ mag.

Self-consistency checks indicate that a differential optical absorption of 0.5 mag/kpc is adequate to reproduce, with our model, the available reddening maps in the distance range $2 \leq r \leq 6$ kpc.

Our best-fit model to three (out of six) selected regions yields a distance of the Sun from the symmetry plane of the Galaxy of $Z_{\odot} = 27 \pm 3\,(3\sigma)$ pc, while the disk's scale-length is found to be $H_{\rm Disk} = 6 \pm 2\,(3\sigma)$ kpc. While the derived value for $Z_{\odot}$ is quite sensitive to the adopted scale-height of disk stars, no big dependency of $H_{\rm Disk}$ on this parameter is found. These values should be taken, of course, with caution because of the inherent uncertainties in modeling optical starcounts in the presence of patchy reddening material.

The accuracy of the reddening and starcounts model opens the possibility of using it to estimate and compare observations of diffuse starlight to constrain the major structural parameters of the Galaxy, and to compute the distance distribution of stars self-consistently with the starcounts, in order to derive corrections to absolute parallax.

Key words: Techniques: photometric – Surveys – Stars: distances – *ISM:* dust, extinction – Galaxy: fundamental parameters – Galaxy: structure

1. Introduction

The method of starcounts as applied to the study of the general properties of the Milky Way has become a very effective way of constraining global structural parameters for the Galaxy (Reid & Majewski 1993), and novel multivariate data analysis methods are being applied to recent surveys to characterize the individual stellar distributions of each population, which would be otherwise unrecognizable (Chen 1996, 1997).

Send offprint requests to: R. A. Méndez

Evidently, most previous comparisons between observed & predicted starcounts have avoided the large-extinction, low-Galactic latitude regions (Bahcall 1986), where the dominant factor determining the observed counts is the distribution of interstellar reddening, whose complex nature would make such an analysis very difficult.

However, there are a number of situations where one may want to evaluate the expected number of stars at low-Galactic latitudes. A few examples are the need for estimating diffuse starlight in the plane of the Milky-Way for comparisons with observations (Mattila 1980a,b, van der Kruit 1986, Toller 1990), the evaluation of the corrections to absolute proper-motion and parallax (van Altena 1974, Monet 1988), and the evaluation of the expected kinematic distribution of stars at low-Galactic latitude for comparisons with the upcoming large digitized surveys (Humphreys 1993).

Méndez (1995, also Méndez & van Altena 1996) has developed a Galactic Structure model, capable of predicting starcounts *self-consistently* with the Kinematic distribution of stars for any line-of-sight. Evidently, in order to evaluate star –and color– counts, as well as the expected kinematic properties of stars at low-Galactic latitudes, we need to provide such a model with the proper reddening values. For certain applications, one could use specifically predetermined values of reddening as a function of Heliocentric distance (i.e., a *reddening map*). However, in many instances, evaluations need to be performed at locations where no specific determination of the reddening has been made, and in such cases, we need to resort to the available low-latitude reddening surveys as a means of estimating the reddening for that particular location.

For the purposes outlined above, we have developed a reddening model, based on what we know about the clumpy nature of the reddening material in the Solar neighborhood from different surveys. We have incorporated also what it is known about its large-scale structure from those surveys, in order to interpolate the reddening values at locations different from those studied in the available literature. In Sect. 2 we introduce the reddening model in detail, Sect. 3 describes our comparisons to starcounts at low-Galactic latitudes from the Guide Star Catalogue, and in Sect. 4 we present our main conclusions.

2. The reddening model

2.1. Introduction

While interstellar absorption, in general, is caused by the mere appearance of material along the line-of-sight (diffuse gas and dust grains), the observed *selective* absorption (i.e., the variation of absorption as a function of wavelength) is caused by *dust particles* that have sizes on the order of the (optical) wavelength of light.

The flux, $F_\lambda(\boldsymbol{r})$ measured by an observer at a distance $|\boldsymbol{r}|$ of a source located at position $\boldsymbol{r}$, and whose flux at the Earth, in the absence of extinction, is $F^{\rm o}_\lambda$, is given by $F_\lambda(\boldsymbol{r}) = F^{\rm o}_\lambda \exp\left(-\tau_\lambda(\boldsymbol{r})\right)$, where $\tau_\lambda(\boldsymbol{r})$ is the (dimensionless) optical-depth of the source along the path (Spitzer 1978). The optical-depth is usually expressed in terms of the number volume density of the absorbing material $n(\boldsymbol{r})$ particles/cm^3, and the average extinction cross-section per particle, κ_λ cm^2/particle, (Mihalas & Binney 1981) via the equation:

$$\tau_\lambda(\boldsymbol{r}) = \kappa_\lambda \int_0^{|r|} n(\boldsymbol{r}')\,{\rm d}|\boldsymbol{r}'| \tag{1}$$

Now, the absorption (in magnitudes) suffered by the light from this source is given by $A_\lambda(\boldsymbol{r}) = -2.5\,log\left(F_\lambda(\boldsymbol{r})/F^{\rm o}_\lambda\right) \approx 1.086\,\tau_\lambda(\boldsymbol{r})$.

The reddening to position $\boldsymbol{r}$, $E(ci)(\boldsymbol{r})$, is simply related to A_λ through the ratio of total-to-selective absorption, defined as $R_\lambda = A_\lambda(\boldsymbol{r})/\left(A_\lambda(\boldsymbol{r}) - A_{\lambda r}(\boldsymbol{r})\right) = A_\lambda(\boldsymbol{r})/E(ci)(\boldsymbol{r}) = \kappa_\lambda/\left(\kappa_\lambda - \kappa_{\lambda 1}\right)$, where ci refers to a specific color index, and λr refers to a fiducial wavelength (Spitzer 1978). As is evident from the above expression, R_λ is determined *only* by the wavelength dependence of the extinction coefficient, and it is independent of position.[1] Since most applications have involved the Johnson & Morgan's (1953) B and V passbands, it is customary to define R_λ in terms of the reddening $E(B-V)$, defined as $(B-V) - (B-V)_{\rm o}$, where $(B-V)$ is the observed (reddened) color of a star with intrinsic color $(\rm B-V)_o$. Of course, any other passbands could be implemented this way (provided that we know the extinction curve). We have adopted a value of $R_{\rm v}$ equal to 3.2 (Mihalas & Binney 1981, Scheffler 1982, Scheffler & Elsässer 1987, although see Sect. 3.2).

[1] Of course, this is valid only for monochromatic radiation, for finite-width passbands R_λ becomes a weak function of spectral type (Gutiérrez-Moreno & Moreno 1975), see Sect. 3.2, Eq. (16)

2.2. The large-scale distribution of reddening material

Parenago (1945) was the first to propose a functional variation for the reddening in the Galactic plane; he showed that an exponentially-decaying function away from the Galactic plane provided an accurate description for the distribution of reddening material as derived from the (photoelectric) color excesses of around 3 000 stars. His suggestion has been validated by later studies, most notably those of Allen (1954) on the statistical distribution of different types of stars (mainly Wolf-Rayet, O and A stars, and White Dwarfs), and by Ochsenbein's (1983) study of the Z-distribution of Am stars from the Michigan Spectral Catalogue. More recent studies have found that the reddening per unit of distance (which is proportional to $d\tau_\lambda(\boldsymbol{r})/\mathrm{d}|\boldsymbol{r}|$), as derived from a complete sample of open clusters closer than 2 kpc follows an exponential decay as a function of height above the plane (Pandey & Mahra 1987), in agreement with the assumption that $n(\boldsymbol{r})$ itself follows a vertical exponential distribution (Eq. (1)), and in agreement with earlier results by Lyngå (1982) from a more restricted sample of open clusters.

Following Parenago, we assume that the (large-scale) volume (particle) density of the absorbing material, $n(\boldsymbol{r})$, follows a decaying exponential away from the Galactic plane, as given by:

$$n(\boldsymbol{r}) \;=\; n_{\mathrm{o}} \exp\left(-|Z|/h_{\mathrm{red}}\right) \tag{2}$$

$$Z \;=\; Z_{\odot} + |\boldsymbol{r}| \,\sin b \tag{3}$$

where h_{red} is the scale-height of the reddening material defining the large-scale distribution of reddening material in a slab of exponential thickness $2 \times h_{\mathrm{red}}$, Z is the distance from the Galactic plane of an object with Heliocentric distance $|\boldsymbol{r}|$ and Galactic latitude b, and $Z_{\odot}$ is the distance of the Sun from the Galactic plane.

There have been several determinations for the scale-height of the reddening material. In Parenago's (1945) pioneer work, he found a practically constant value for h_{red} equal to 100 ± 4 pc. More recently, Lyngå (1982) found equally probable the values of $h_{\mathrm{red}} = 130$ and $h_{\mathrm{red}} = 270$ pc, although the results of Burstein & Heiles (1982) toward the Galactic Poles (which imply $A_{\mathrm{v}} < 0.1$ mag) would favor the smaller value with Lyngå's adopted value of 0.75 mag/kpc for A_{v}. Pandey & Mahra (1987) found $h_{\mathrm{red}} = 160 \pm 20$ pc from their complete sample of nearby open clusters. Additional evidence comes from direct measurements of the thickness of both neutral Hydrogen (HI) and Carbon Monoxide (CO) in the Galactic disk. It is known that $E(B-V)$ is approximately proportional to the neutral Hydrogen column density (Heiles 1976 [particularly his Fig. 13a, and references therein], Burstein & Heiles 1978 [particularly their Fig. 1a]), therefore the thickness of the reddening material should be approximately well sampled by the distribution of HI itself. Different studies (Scheffler & Elsässer 1987) have obtained thicknesses of about 130 to 150 pc from measurements of cold diffuse HI. On the other hand, Spitzer (1978) estimates that $h_{\mathrm{red}} \approx 100$ pc from the statistical properties of the dust layer within 1 kpc of the Sun. Finally, since the correlation $E(B-V)$ *vs.* $N(\mathrm{HI})$ involves a gas-to-dust ratio, it would seem reasonable to expect that $E(B-V)$ is related also to the distribution of molecular material. From a compilation of different CO surveys (Solomon et al. 1979, Table 1), we find $h_{\mathrm{red}}(\mathrm{CO}) \sim 40$ *to* 70 pc, while from their own CO survey of giant molecular clouds they find $h_{\mathrm{red}}(\mathrm{CO}) \approx 65$ pc. As a compromise value between all these different determinations, we have assumed in our reddening model a scale-height of 110 pc.

2.3. Reddening at intermediate and high Galactic latitudes

For intermediate-to-high Galactic latitudes ($|b| \geq 10^{\circ}$), reddening through "infinity" has been estimated by using Burstein & Heiles (1982, BH thereafter) reddening maps (available in computer-readable form). These reddening estimates are used in our model to compute the reddening via the equation:

$$\frac{E(B-V)(r,l,b)}{E(B-V)(l,b)_{\infty}} =$$

$$\begin{cases} 1 - \exp\left(-\frac{r\,\sin b}{h_{\mathrm{red}}}\right) \;\text{ if } b > +10^{\circ} \\ \frac{1-\exp\left(-\frac{r\,\sin b}{h_{\mathrm{red}}}\right)}{1-2\exp\left(\frac{Z_{\odot}}{h_{\mathrm{red}}}\right)} \;\text{ if } b < -10^{\circ} \text{ and } r\,|\sin b| \leq Z_{\odot} \\ \frac{1-2\exp\left(\frac{Z_{\odot}}{h_{\mathrm{red}}}\right)+\exp\left(\frac{2\,Z_{\odot}+r\,\sin b}{h_{\mathrm{red}}}\right)}{1-2\exp\left(\frac{Z_{\odot}}{h_{\mathrm{red}}}\right)} \;\text{ if } b < -10^{\circ} \text{ and } r\,|\sin b| > Z_{\odot} \end{cases} \tag{4}$$

where r is the Heliocentric distance for a point with Galactic coordinates (l,b), and $E(B-V)(l,b)_{\infty}$ is the reddening at "$r = \infty$" from the BH maps. Equation (4) has been derived by performing the line-of-sight integration to Heliocentric

distance r on our assumed density law for the absorbing material (Eq. (2) and (3)), as required by Eq. (1)). It should be noted that, if the Sun is located in the plane of symmetry of the Galaxy, then Eq. (4) reduces to the simpler case $E(B-V)(r,l,b) = E(B-V)(l,b)_\infty \times (1-\exp(-r\,|\sin b|/h_{\rm red}))$, valid for any value of the Galactic latitude (as long as $|b| \geq 10^\circ$).

Since the BH maps do not cover the entire sky, for regions where there is no data available, we have adopted Sandage's (1972) modified cosecant law, given by:

$$A_{\rm v}(b)_\infty \; = \; \begin{cases} 0.165 \times \dfrac{\left(\tan 50^\circ - \tan b\right)}{\sin b} & \text{if } 10^\circ \leq |b| < 50^\circ \\ 0 & \text{if } |b| \geq 50^\circ \end{cases} \tag{5}$$

where $A_{\rm v}(b)_\infty$ is the absorption, at infinity, that goes into Eq. (4), after conversion to $E(B-V)(l,b)_\infty$ using our adopted value of $R_{\rm v}$. Following Sandage, the above expression is only applied for $10^\circ \leq |b| < 50^\circ$, while it is assumed that $A_{\rm v}(b)_\infty = 0$ at higher latitudes. Sandage's law, based on an earlier model proposed by McClure & Crawford (1971), has been extensively criticized by de Vaucoleurs & Buta (1983). de Vaucoleurs & Buta find, on the basis of galaxy and galaxy clusters counts that a simple cosecant law (as derived from a plane-parallel absorbing layer, Dufay 1954) applies all the way to the poles, with a polar extinction of 0.2 magnitudes in $A_{\rm B}$. de Vaucoleurs & Buta also back their findings by considering the surface brightness, the hydrogen-luminosity ratio, and the integrated color indices of galaxies on the Second Reference Catalogue of Bright Galaxies (de Vaucoleurs et al. 1976). de Vaucoleurs & Buta furthermore criticized Sandage's law on the basis that it implies that the Sun is located in the common apex of two opposite dust-free cones centered at the Galactic poles (see Fig. 1 on de Vaucoleurs & Buta). Sandage's law, on the other hand, agrees with the very small color excesses found for stars and globular clusters at high Galactic latitudes. In Fig. 1 we show a comparison between the de Vaucoleurs & Buta's and Sandage's law with the longitude-averaged run of reddening from the BH maps. From this figure, it is clear that Sandage's law is a better representation of the actual variation of reddening as a function of Galactic latitude. The discrepancy between Sandage's (zero-reddening) model and the BH maps for $|b| > 50^\circ$ is not relevant in this context, as most of the missing points from the BH maps ocurr at smaller Galactic latitudes (except for the region $b \leq -60^\circ$ and $-130^\circ \leq l \leq 20^\circ$ where no data is available from the BH maps). Figure 1 also clearly shows that, at high Galactic latitudes, neither of the two laws seem to be a good representation of the BH maps. Indeed, Knude (1996) has recently found, from the color excesses derived from Strömgren photometry for a complete sample of A3-G0 stars brighter than $B = 11.5$ and with $b > +70^\circ$, that the North Galactic Pole exhibits a complex reddening distribution, with zonal variations (in latitude and longitude) which can be represented more by what he calls 'a slightly frosted window'. This shows that *any* functional representation for the total reddening, even at high Galactic latitudes, has to be taken with caution. It is also interesting to notice that Knude finds a very good agreement between the zero-point on the BH maps (derived from colors of RR Lyrae and individual stars in globular clusters) and that derived by Knude's uvbyHβ photometry of individual stars towards *both* the south and north galactic poles.

The adequacy of the interpolation scheme described above has been demonstrated recently by Méndez & van Altena (1996), by performing *simultaneous* fits to the magnitude and color counts for two intermediate-latitude fields located at $(l,b) = (123^\circ, +22^\circ)$ and $(287^\circ, +17^\circ)$. The amount and distribution of the reddening material is important for both the starcounts (where reddening affects the total number of objects in a given field-of-view) as well as the color-counts (where reddening affects the color distribution of stars). The comparisons performed by Méndez & van Altena indicate that, indeed, the exponential approximation gives a very good fit to the star- and color-counts towards these two fields having moderate extinction ($E({\rm B-V})_\infty = 0.07$ mag and 0.05 mag for the two fields-of-view respectively). We should also point out that the use of Eq. (4) for the case $Z_\odot = 0$ pc is not new: it was proposed, e.g., by van Herk (1965) in his study of the motions and space distribution of RR Lyrae stars, and it has been subsequently used in different contexts where an accurate statistical determination of the reddening is needed (e.g., Di Benedetto & Rabbia 1987, Fouqué & Gieren 1996). Indeed, Di Benedetto & Rabbia (1987) have pointed out that van Herk's model yields the same reddening estimates as those derived from the method of color-excess described by Savage & Mathis (1979) when using a scale-height of 100 pc, close to our adopted value (Sect. 2.2). Finally, Jønch-Sørensen (1994) has investigated the reddening in six fields with $|b| \geq +14^\circ$ up to distances of 10 kpc using uvbyHβ photometry. He finds quite a good agreement in the run of reddening with distance compared to that predicted by a simple exponential model similar to that of Eq. (4) (see, e.g, his Fig. 5), although he warns that simply adopting $E(B-V)(l,b)_\infty$ from the BH maps yields systematically lower reddening than observed, except for the fields with the smaller reddening values. The

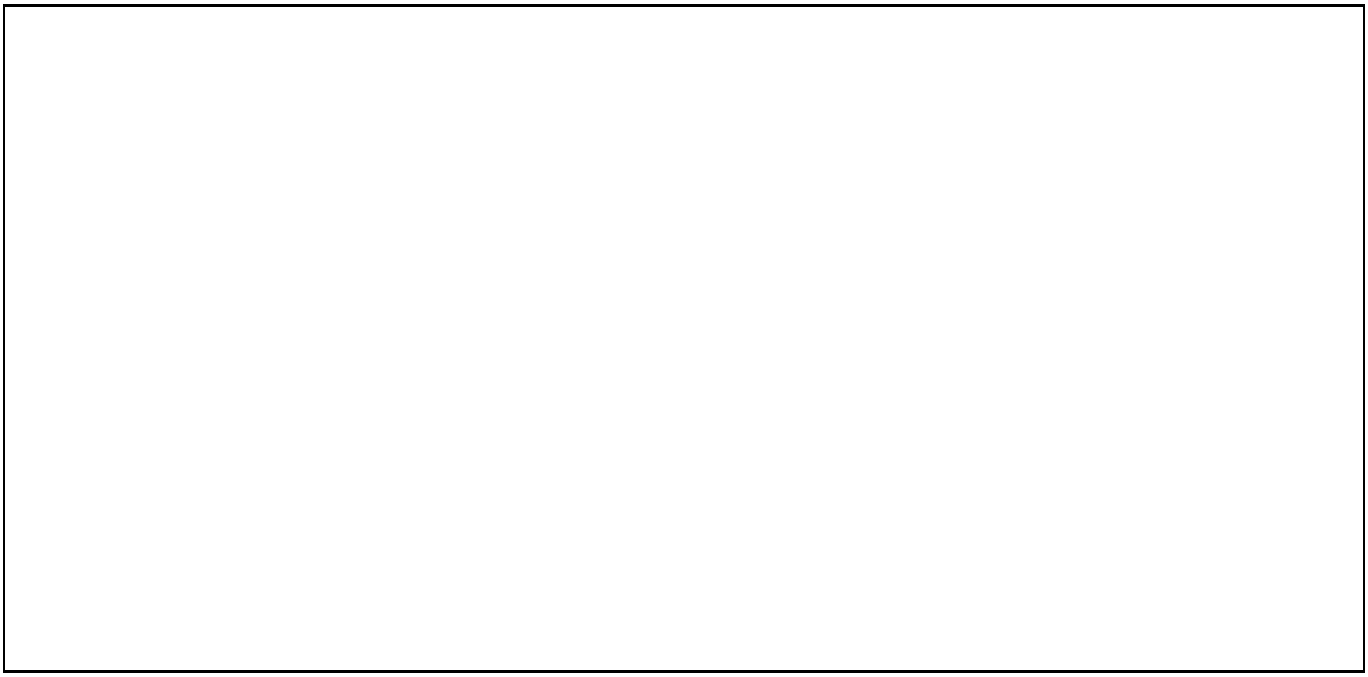

Fig. 1. Longitude-averaged reddening *vs.* Galactic latitude from the Burstein & Heiles maps (1982). Square symbols are for the northern Galaxy ($b \geq +10^{\circ}$), circle symbols are for the southern Galaxy($b \leq -10^{\circ}$). Open symbols indicate mean reddening with the corresponding error of the mean. Filled symbols indicate the standard deviation. The solid line shows Sandage's (1972) modified cosecant law, while the dashed lines indicate de Vaucoleurs & Buta's (1983) cosecant law, where we include the published range of 0.1 to 0.2 for $A_{\rm B}$ at the pole (Lu et al. 1992).

largest difference found among the six fields studied by Jønch-Sørensen amounts to 0.15 mag in $E(B-V)$, with a mean difference for the six regions of 0.081 ± 0.054 mag. This underestimation is partially a volume-sampling effect, because of the coarse angular resolution of the BH maps (derived from HI observations with a beam size of 0.6°) in comparison with the sizes of the fields studies by Jønch-Sørensen (smaller than $0.06\,\square^{\circ}$). Indeed, as pointed out by Burstein & Heiles (1982), their maps should be an accurate representation of the reddening in the Galaxy in regions where the variation of reddening with position is small over the angular resolution of the maps. Evidently, for specific applications (e.g, those involving small fields-of-view), the reddening should be determined either from multi-color photometry or from the magnitude and color counts, as done by Méndez & van Altena (1996). It is interesting to notice that, in the study by Méndez & van Altena (1996), involving two regions of about $0.5\,\square^{\circ}$ each, their derived reddening values are systematically *lower* than those from the BH maps in an amount of 0.012 mag for their NGC 188 field, and 0.042 mag for their NGC 3680 field.

2.4. Reddening at low Galactic latitudes

For low-latitudes ($|b| < 10^{\circ}$), we have used published reddening maps giving $E(B-V)$ *vs.* Heliocentric distance and Galactic position. The main optical surveys devoted to the study of the spatial distribution of interstellar reddening material in the solar neighborhood have been those of FitzGerald (1968, 1974, 1987, collectively called FG hereafter), FitzGerald & Reed (1991), and Neckel & Klare (1980, NK hereafter), with a number of other more restricted surveys (Deutschman et al. 1976, Forbes 1985, Pandey & Mahra 1987). In this study we have only included the reddening determinations by FG and NK. FG's maps include a number of regions with $|b| \approx 0^{\circ}$, while NK's maps are restricted to the range $|b| < 7.6^{\circ}$, both studies cover the range $0^{\circ} \leq l < 360^{\circ}$.

Since no computer-readable form existed for either FG's nor NK's maps, we had to read-off their adopted mean reddening curves directly from the figures in their publications (we should note that, given the resolution of the maps presented by FG and NK, we estimate a "reading" uncertainty of about 0.03 mag in $E(B-V)$, while the quoted errors for the reddening from the FG and NK maps are 0.015 mag and 0.031 to 0.063 mag respectively). This involved the key-punching of reddening maps for 75 lines-of-sight from FG's regions, and 316 lines-of-sight from NK's regions. Each line-of-sight consists itself of "node points" at different Heliocentric distances. Therefore, our low-latitude grid

consists of 388 lines-of-sight (three lines-of-sight were duplicated in both studies), with 1,263 independent node points covering the whole Galactic plane with $|b| < 10^{\circ}$. The average angular resolution in Galactic longitude is therefore around 1°, but there are fluctuations in this number due to the selective study of certain regions by both authors. Figure 2 shows the distribution of node points with respect to the Sun, projected onto the plane of the Galaxy (see also Fig. 4 in FitzGerald 1968, Fig. 9a in NK, and Fig. 4 below).

Fig. 2. Distribution of reddening node points on the plane of the Galaxy with respect to the Sun. The V axis is positive in the direction of Galactic rotation, while the U axis is positive toward the Galactic center. The Sun is located at (0,0). The size of the points is proportional to the reddening at that position, with the smallest dots having $E(B-V) = 0.03$, and the largest $E(B-V) = 1.29$ mag

In Fig. 3 we show a comparison between FG's and NK's maps for the three directions in common between these two studies. NK's values of $A_{\rm v}$ have been converted to $E(B-V)$ using his adopted value of $R_{\rm v} = 3.1$. We can see that, at $l = 121^{\circ}$, there is a good agreement between FG's and NK's values for $r < 1$ kpc, however there is an asymptotic difference in $E(B-V)$ of 0.4 mag at $r \approx 3$ kpc. The agreement at $l = 187^{\circ}$ is however very good at all distances ($r \leq 4$ kpc). Finally, at $l = 245^{\circ}$, even though there is a good agreement for $4 < r \leq 6$ kpc, FG's map shows a faster increase at small distances ($r < 500$ pc) and then it remains constant up to 3.5 kpc, whereas NK's map indicates a reddening approximately a factor of three bigger than FG's value. For these three directions we have chosen NK's values over those of FG. The general agreement of these maps at small distances ($r < 1$ kpc) is important, because most of the bright to intermediate magnitude counts come from stars located at similar Heliocentric distances. However, the noted discrepancies at large distances imply that the adoption of these mean-extinction curves has to be taken with caution, specially when trying to evaluate the reddening at large Heliocentric distances.

In the following section we describe the interpolation scheme used to obtain reddening at positions other than those specified in FG's and NK's reddening maps.

2.5. Reddening interpolation at low Galactic latitudes

2.5.1. Generalities

If the Galactic latitude of the point for which reddening is sought is such that $|b| < 10^{\circ}$, an interpolation scheme has been devised that assumes that the distribution of reddening material presents both a "smooth" component represented by an exponential distribution of dust perpendicular to the Galactic plane (Sect. 2.2), and a "clumpy" component that represents the fragmentary nature of individual molecular clouds along the line of sight, represented

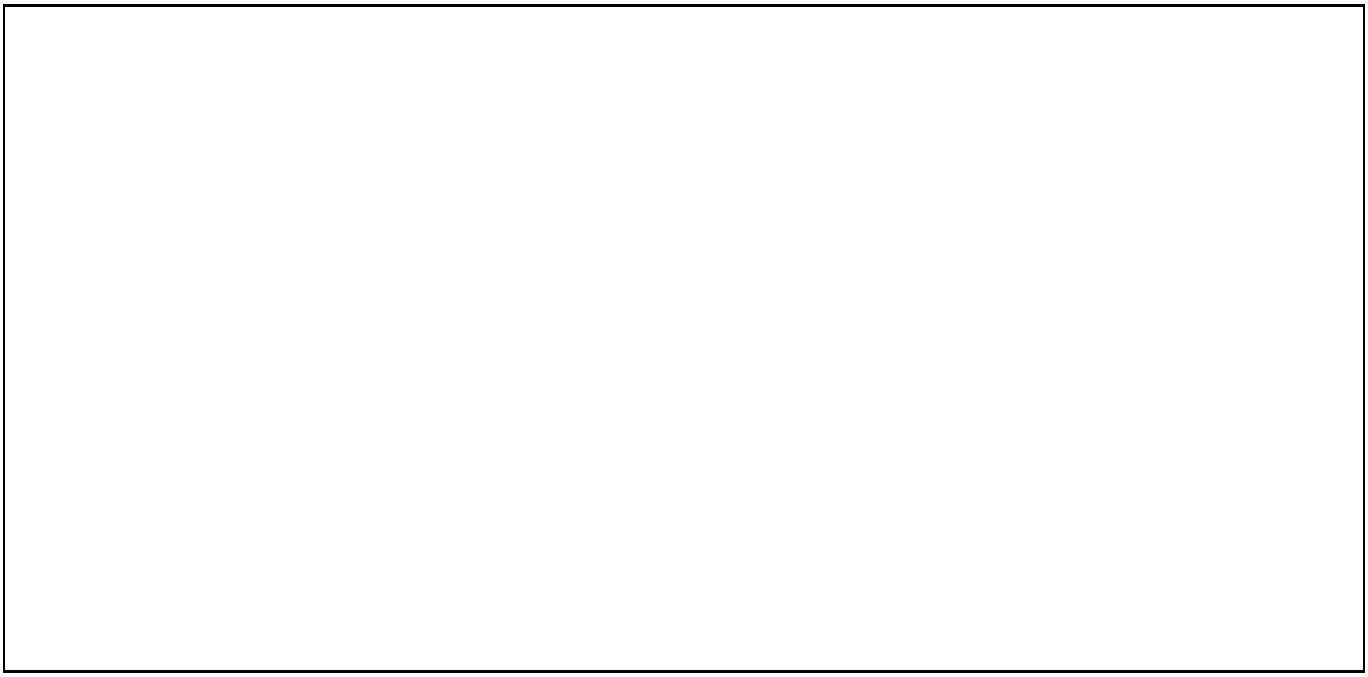

Fig. 3. Reddening values for three directions in common between FG's and NK's reddening maps.

by the available reddening maps. To accommodate for poorly sampled directions in the plane, the BH reddening maps at $|b| = \pm 10^{\circ}$ are dynamically incorporated in the interpolation. This also ensures a continuous transition to higher latitudes.

If (r, l, b) are the Heliocentric distance and the Galactic position of the point for which reddening is sought (the "target"), the (combined) FG and NK reddening maps are searched for the two node points in longitude that enclose the target longitude. Then, at those two longitudes, the two latitudes that enclose the target latitude are searched for. This search procedure may yield up to four node points enclosing the target point. Then, at each enclosing node point, the reddening at distance r is interpolated linearly in distance from the respective reddening maps. In this linear interpolation, if the target distance is smaller than the first node point for a particular reddening map, the value is interpolated assuming zero reddening at zero distance and the reddening associated with the first distance point in the reddening map. On the other hand, if the target distance is greater than the last node point, the reddening is *extrapolated*, as described in the following subsection.

In addition to the four nearby points, the reddening at Heliocentric distance r, Galactic longitude l, and Galactic latitudes of $\pm 10^{\circ}$ is computed from the BH reddening maps. These reddening values are used mainly for the intermediate region $5^{\circ} < |b| < 10^{\circ}$, where FG's and NK's reddening maps do not constrain the reddening very well, and to provide a smooth transition to higher Galactic latitudes.

2.5.2. Reddening extrapolation

We have attempted two different approaches to obtain the reddening at distances beyond the last node point. First, we have tried assuming a constant value of absorption per unit of distance (e.g., 1.5 mag/kpc in $A_{\rm v}$), and using the last node point as a zero-point, i.e.:

$$A_{\rm v}(r, l, b) = A_{\rm v}(r_l, l, b) + \delta A_{\rm v} \times (r - r_l) \tag{6}$$

where $A_{\rm v}(r_l, l, b)$ is the reddening for the last distance node located at r_l, and $\delta A_{\rm v}$ is the adopted absorption per unit of distance. This extrapolation approach is similar to that adopted in the extinction model by Arenou et al. (1992), we shall call this Model-A. This model, which is quite common (see Sect 2.6.1), has two main drawbacks. First, as we shall see below (Eq. 15), the absorption in the solar vicinity has a Galactic longitude dependence near the plane, and therefore it is not correct, in principle, to assume a constant value for the differential reddening. However, since this value is applied only after the last reddening point (typically located at Heliocentric distances of 3 to 4 kpc (Fig. 2)),

we can view the term $\delta A_{\rm v}$ as a *residual reddening*, with a minor effect on the bright starcounts discussed below, which are dominated by stars located at distances of about 1 to 2 kpc (see Sect 3.3), whereas the term $A_{\rm v}(r_l, l, b)$ not only sets the zero-point, but also determines the Galactic longitude dependence. The second shortcoming of this approach is that, at large Heliocentric distances and $b \neq 0^{\circ}$, this model assumes a constant value of reddening for stars situated many (reddening) scale-heights from the disk, leading therefore to an excess on the predicted reddening. This problem has been alleviated in the model by Arenou et al. (1992) by adopting zero differential reddening beyond a Heliocentric distance such that the corresponding distance from the Galactic plane is larger than the adopted scale-height of the reddening material.

The second extrapolation scheme (Model-B) comes from insisting on the functional form of the large-scale distribution of the reddening material presented in Sect. 2.2, and from using, again, the last reddening point, but this time as a scale factor (rather than as a zero-point) for the extrapolation. If $E(r_l, l, b)$ is the last reddening point, it is possible to show that the extrapolated reddening to an Heliocentric distance r (with $r > r_l$) is given by[2]:

$$\frac{E(r,l,b)}{E(r_l,l,b)} =$$

$$\begin{cases} \frac{1-\exp\left(-\frac{r\,\sin b}{h_{\rm red}}\right)}{1-\exp\left(-\frac{r_l\,\sin b}{h_{\rm red}}\right)} \text{ if } b \geq 0^{\circ} \\ \frac{1-2\exp\left(\frac{Z_{\odot}}{h_{\rm red}}\right)+\exp\left(\frac{2\,Z_{\odot}+r\,\sin b}{h_{\rm red}}\right)}{1-2\exp\left(\frac{Z_{\odot}}{h_{\rm red}}\right)+\exp\left(\frac{2\,Z_{\odot}+r_l\,\sin b}{h_{\rm red}}\right)} \text{ if } b < 0^{\circ} \text{ and } r_l\,|\sin b| \geq Z_{\odot} \\ \frac{1-\exp\left(-\frac{r\,\sin b}{h_{\rm red}}\right)}{1-\exp\left(-\frac{r_l\,\sin b}{h_{\rm red}}\right)} \text{ if } b < 0^{\circ} \text{ and } r\,|\sin b| \leq Z_{\odot} \\ \frac{1-2\exp\left(\frac{Z_{\odot}}{h_{\rm red}}\right)+\exp\left(\frac{2\,Z_{\odot}+r\,\sin b}{h_{\rm red}}\right)}{1-\exp\left(-\frac{r_l\,\sin b}{h_{\rm red}}\right)} \text{ if } b < 0^{\circ},\ r_l\,|\sin b| \leq Z_{\odot}, \text{ and } r\,|\sin b| \geq Z_{\odot} \end{cases} \tag{7}$$

We note that the above expression does not diverge for $b = 0^{\circ}$, in this case the extrapolated reddening is given by $E(r, l, b) = E(r_l, l, b) \times r/r_l$. By comparing this simple expression with Eq. (6), we see that a linear extrapolation is indeed a special case of Eq. (7) for $b = 0^{\circ}$ if we identify $\delta A_{\rm v}$ with $A_{\rm v}(r_l, l, b)/r_l$. In Model-B, the Galactic longitude dependency is, of course, built-into $E(r_l, l, b)$, and the decrease of reddening beyond the scale-height of the obscuring material is fully taken into account. The main problem with this model comes from the fact that, since $E(r_l, l, b)$ acts as a scale-factor (rather than as a zero-point as it was the case on Eq. (6)), the extrapolated reddening is extremely sensitive to uncertainties in the last reddening point which, being located at large Heliocentric distances, is subject to a greater uncertainty than the node points located at smaller Heliocentric distances, a point clearly demonstrated by Fig. 3 (see also discussion at end of Sect. 2.4). In Sects. 2.6.1 and 2.6.2 we fully compare the results of adopting either model, and its impact on the predicted reddening.

2.5.3. Weighting scheme & interpolation

Once the reddening of the four adjacent node points has been found, the reddening at the target is found through a *weighted* mean of the reddening from those four node points, plus the scaled reddening values from the BH maps. If w_i (i=1...4) are the assigned weights to the four enclosing reddening points with reddening E_i, and $w_{\rm p}$, and $w_{\rm n}$ are the weights assigned to the BH reddening values at $b = +10^{\circ}$ and $b = -10^{\circ}$ respectively, then the interpolated reddening is computed via:

$$E(r,l,b) = \frac{\sum_{i\leq 4} w_i \times E_i + w_{\rm p} \times E_{\rm p} + w_{\rm n} \times E_{\rm n}}{\sum_{i\leq 4} w_i + w_{\rm p} + w_{\rm n}} \tag{8}$$

where $E_{\rm p}$ and $E_{\rm n}$ are the values derived from the BH reddening maps (Eq. (4)), at $b = +10^{\circ}$ and $b = -10^{\circ}$ respectively.

We have incorporated the clumpy nature of the absorbing material, as well as its large-scale properties, through a proper selection of the weights specified in Eq. (8). The weights $w_i(r, l, b)$ are given by:

[2] Equation (7) is only valid for $Z_{\odot} \geq 0$, but similar expressions can be written for $Z_{\odot} < 0$.

$$w_i(r,l,b) = \tilde{w}_i(r,l,b) \times f(\delta S_i) \tag{9}$$

$$\delta S_i = \sqrt{2\ (1-\cos\theta_i)} \times r \tag{10}$$

$$\cos\theta_i = \cos b\ \cos b_i\ \cos l\ \cos l_i + \cos b\ \cos b_i\ \sin l\ \sin l_i + \sin b\ \sin b_i \tag{11}$$

where (l_i, b_i) are the Galactic longitude and latitude of the i-th node point, $\tilde{w}_i(r,l,b)$ are the weights that describe the large-scale variation of the reddening material, $f(\delta S_i)$ is a function that considers the patchy distribution of reddening material, and δS_i and θ_i are the linear and angular distances between the corresponding node points and the target respectively. The weights $\tilde{w}_i(r,l,b)$ have two components, a latitude component, $w_i^{\rm b}(r,b)$, and a longitude component, $w_i^{\rm l}(r,l)$, both of which are described below. The large-scale component of the weights is thus given by $\tilde{w}_i(r,l,b) = w_i^{\rm b}(r,b) \times w_i^{\rm l}(r,l)$.

The weights $w_i^{\rm b}(r,b)$ are computed by taking the ratio of the expected value for the reddening at position (r,l,b), and the expected value at the respective node position. Effectively this ratio scales the (observed) reddening value at the node point to that at the target location. This is achieved by using our assumed density law for the dust particles (Eq. (2)) integrated over the appropriate line-of-sight (Eq. (1)). The weights $w_i^{\rm b}(r,b)$ are thus given by:

$$w_i^{\rm b}(r,b) = \frac{\Omega(r,b)}{\Omega(r,b_i)} \tag{12}$$

where the function $\Omega(r,b)$ is computed as[3]:

$$\Omega(r,b) = \begin{cases} \frac{1-\exp\left(-\frac{r\,\sin b}{h_{\rm red}}\right)}{\sin b} \text{ if } b \geq 0^\circ \\ \frac{1-\exp\left(-\frac{r\,\sin b}{h_{\rm red}}\right)}{\sin b} \text{ if } b < 0^\circ \text{ and } r\,|\sin b| \leq Z_\odot \\ \frac{1-2\exp\left(\frac{Z_\odot}{h_{\rm red}}\right)+\exp\left(\frac{2\,Z_\odot+r\,\sin b}{h_{\rm red}}\right)}{\sin b} \text{ if } b < 0^\circ \text{ and } r\,|\sin b| > Z_\odot \end{cases} \tag{13}$$

For example, if $Z_\odot = 0$, the weights $w_i^{\rm b}(r,b)$ (for *any* value of r, b, and b_i) take the very simple expression:

$$w_i^{\rm b}(r,b) = \frac{\left(1-\exp\left(-\frac{r\,|\sin b|}{h_{\rm red}}\right)\right)}{\left(1-\exp\left(-\frac{r\,|\sin b_i|}{h_{\rm red}}\right)\right)} \times \frac{|\sin b_i|}{|\sin b|} \tag{14}$$

Note also that, for $b = 0^\circ$, $\Omega(r,b)$ does not diverge, but it approaches the ratio $r/h_{\rm red}$ which corresponds to a linear increase of reddening with distance (see Eq. (6), and comments following Eq. (7)). Indeed, this is the only possible asymptotic solution for an exponential layer, as b goes to zero.

In addition to the Galactic-latitude (or height above the plane) dependence of the weights, we have implemented also a longitude dependence. From a study of classical Cepheids, Fernie (1968) found that the reddening exhibits a cyclic (sinusoidal) variation with Galactic longitude at $b = 0^\circ$, while Pandey & Mahra (1987) found a similar behavior for $|b| < 10^\circ$ from a sample of 462 open clusters with known color excesses and (photometric) distances. For the cyclic variation represented by $\delta A_{\rm v}(l) = \delta A_{\rm v}^{\rm o} + \delta A_{\rm v}^{\rm l}\ \sin(l + l_{\rm o})$, Fernie (1968) found $\delta A_{\rm v}^{\rm o} = 0.90 \pm 0.04$ mag/kpc, $\delta A_{\rm v}^{\rm l} = 0.28 \pm 0.06$ mag/kpc, and $l_{\rm o} = 41^\circ \pm 13^\circ$ from Cepheids located at Heliocentric distances closer than 6 kpc. Pandey & Mahra (1987) found a maximum absorption at $l \approx 50^\circ$, and a minimum absorption at $l \approx 230^\circ$, for $r < 2$ kpc (where their sample of open clusters is not extremely biased), in accordance with Fernie's value for $l_{\rm o}$. Lyngå (1979, 1982) also found a maximum average interstellar absorption toward $l \approx 50^\circ$, based on a study of B stars, classical Cepheids, and open clusters.

Based on Fernie's results, our weights in Galactic longitude, $w_i^{\rm l}(r,l)$, have been defined as:

$$w_i^{\rm l}(r,l) = \begin{cases} \frac{\delta A_{\rm v}^{\rm o}+\delta A_{\rm v}^{\rm l}\ \sin(l+l_{\rm o})}{\delta A_{\rm v}^{\rm o}+\delta A_{\rm v}^{\rm l}\ \sin(l_i+l_{\rm o})} & \text{if } r \leq 6 \text{ kpc} \\ 1 & \text{otherwise} \end{cases} \tag{15}$$

[3] Equation (13) is valid only for $Z_\odot \geq 0$, but similar expressions can be written for $Z_\odot < 0$.

Since Fernie's relationship seems to pertain only to the local distribution of reddening material, the weights given in Eq. (15) are only applied for distances smaller than 6 kpc.

As for the function $f(\delta S)$ in Eq. (9), we have tried different functional forms, and we have chosen the one that minimizes the reddening residuals of the observed *vs.* predicted node point in a self-consistent way, as described in Sect. 2.6. The purpose of introducing this function has been to take into account the discrete nature of the individual clouds and the patchy distribution of the interstellar dust by weighting the node points according to its proximity to the target location.

We should note that, since the BH reddening maps are evaluated at $(l, \pm 10^\circ)$, then Eq. (11) becomes $\cos\theta_{\rm pn} = \cos b \cos 10^\circ \pm \sin b \sin 10^\circ$, where the + sign applies to the node point with reddening $E_{\rm p}$ (with weight $w_{\rm p}$), while the - sign applies to the node point with reddening $E_{\rm n}$ (with weight $w_{\rm n}$) from the BH maps. Also, for the BH reddening values we do not apply any Galactic longitude variation component to the weights (which are applicable only to $b \sim 0^\circ$), but only the latitude dependence (Eq. (12)).

Overshoot and undershoot in latitude in those cases where the target latitude is bigger or smaller respectively than the biggest and smallest latitude on the reddening arrays is taken care of by considering only the closest latitude point with the proper weight. Therefore the interpolation is set up to work with a maximum of six points (four node points from the low-latitude reddening maps, and two node points from the BH maps) to a minimum of four points (two node points from the low-latitude reddening maps, and two node points from the BH maps). Note that in cases of over/undershoot we extrapolate in latitude using our exponential reddening model described above. Since reddening data is available in the whole range $0^\circ \leq l < 360^\circ$, there is never over/undershoot in longitude.

It should be noticed that, with the weighting scheme described above, the role of the BH maps, even at low Galactic latitudes, is quite important. For example, for a target point at $(r, l, b) = (1\,{\rm kpc}, 90^\circ, +1^\circ)$ with a node point at $(l, b) = (90^\circ, 0^\circ)$, the weights applied to the node point and the values from the BH maps at $\pm 10^\circ$ are 0.91, 1.84, and 1.37 correspondingly, where we have adopted for $f(\delta S)$ an inverse-linear relationship (see Sect. 2.6), $Z_\odot = +7$ pc, and $h_{\rm red} = 110$ pc. In cases where the target location is enclosed by four node points from the FG or NK maps, one might not use the BH maps, and could perform an interpolation using only those node points. However, due to the relatively poor angular sampling of the current maps (see Sect. 2.4 and Fig. 2) it seldom occurs that a target is surrounded by four node points, and therefore this is not a problem for the current implementation of the model, but it could become important as the density of node points increases through the incorporation of more reddening maps in our database.

A simpler approach, but similar to that of Eq. (8), has been used recently by Layden et al. (1996) in the context of statistical parallaxes for RR Lyrae stars. Indeed, this is yet another possible use of our starcounts & kinematic model, which we intend to pursue in the future.

2.6. Tuning the low Galactic latitude interpolation

The following procedure has been adopted to estimate the expected uncertainty in the interpolated reddening values: the reddening has been computed at each node point for a given longitude (a "longitude slice") from the two adjacent node points in longitude, and the root-mean-square (rms) residual between the predicted value and the observed one has been obtained for each of those longitude slices. Our reddening maps have 276 independent longitude slices. Each longitude slice may contain more than one latitude node (although it has, typically, only one latitude point at $b \sim 0^\circ$) and, at each latitude, there may be node points at more than one Heliocentric distance. This scheme is similar to the way in which reddening is computed for a line-of-sight integration in our starcounts model (Sect. 3.2), and therefore it provides a realistic description of the accuracy of our reddening model.

Using the above procedure we can examine the residuals between our model predictions and the observed values at each node point in the reddening maps in a self-consistent manner. This allows us to "tune-up" the adopted parameters, as well as the exact distance weighting scheme in the reddening model (the term $f(\delta S)$ in Eq. (9)), so as to minimize the scatter between the predicted and observed values. In the following two subsections we deal, separately, with the Models-A and B described in subsection 2.5.2 (Eqs. (6) and (7)).

2.6.1. Tuning Model-A

Figure 4 shows the residuals (in the sense $E(B-V)_{\rm model} - E(B-V)_{\rm node}$) as a function of Galactic latitude, longitude, and Heliocentric distance for Model-A. Figures 4a-b provide and indication of the angular sampling with the reddening maps implemented in the current version of our reddening model, it also shows that we do not have any obvious systematic trend in the predicted residuals as a function of either Galactic latitude or longitude. Figure 4c shows, on

the other hand, an upward trend in the residuals *vs.* distance, particularly for $r > 2$ kpc. This is caused by a value of $\delta A_{\rm v}$ beyond the last node point that is too large. The value of $\delta A_{\rm v}$ used in Fig. 4c was 1.5 mag/kpc. Table 1 indicates the dispersion in the reddening model as a function of $\delta A_{\rm v}$. The best value for $\delta A_{\rm v}$, obtained from a minimization of the residuals as a function of this parameter, gives $\delta A_{\rm v} = 0.5$ mag/kpc, which for a value of $R_{\rm v} = 3.2$ corresponds to only 0.16 mag/kpc of reddening beyond 2 kpc. This value is considerably *smaller* than previous determinations of $\delta A_{\rm v}$, which yielded values closer to 1.5 mag/kpc. For example, Van Herk (1965) adopted a value of 1.9 mag/kpc (for $|b| > 40^{\circ}$), and Di Benedetto & Rabbia (1987) a value of 1.4 mag/kpc. On the other hand, Lyngå (1982) adopted a value of 0.75 mag/kpc from an statistical study of a sample of open clusters. More recently, Blackwell et al. (1990) have discussed the evidence for even smaller values of $\delta A_{\rm v}$ from the *local* (i.e., $r < 300$ pc) distribution of reddening material around the Sun, adopting in the end an absorption of 0.6 mag/kpc, quite close to our derived value. We should note, however, that those determinations were concerned with *local* reddening, while our value is determined mainly from the more distant node points (further than 2 kpc from the Sun). Figure 4d shows the residuals *vs.* distance for $\delta A_{\rm v} = 0.5$ mag/kpc (Figs. 4a-b were produced with this value of $\delta A_{\rm v}$ as well). The residuals *vs.* distance vary slowly with $\delta A_{\rm v}$ and, as a result, our minimum is rather shallow. This is because a large fraction of the residual is produced by the nearby points that are not sensitive to the actual value of $\delta A_{\rm v}$. However, the effect of different values of $\delta A_{\rm v}$ at large Heliocentric distances is obvious in Figs. 4c-d.

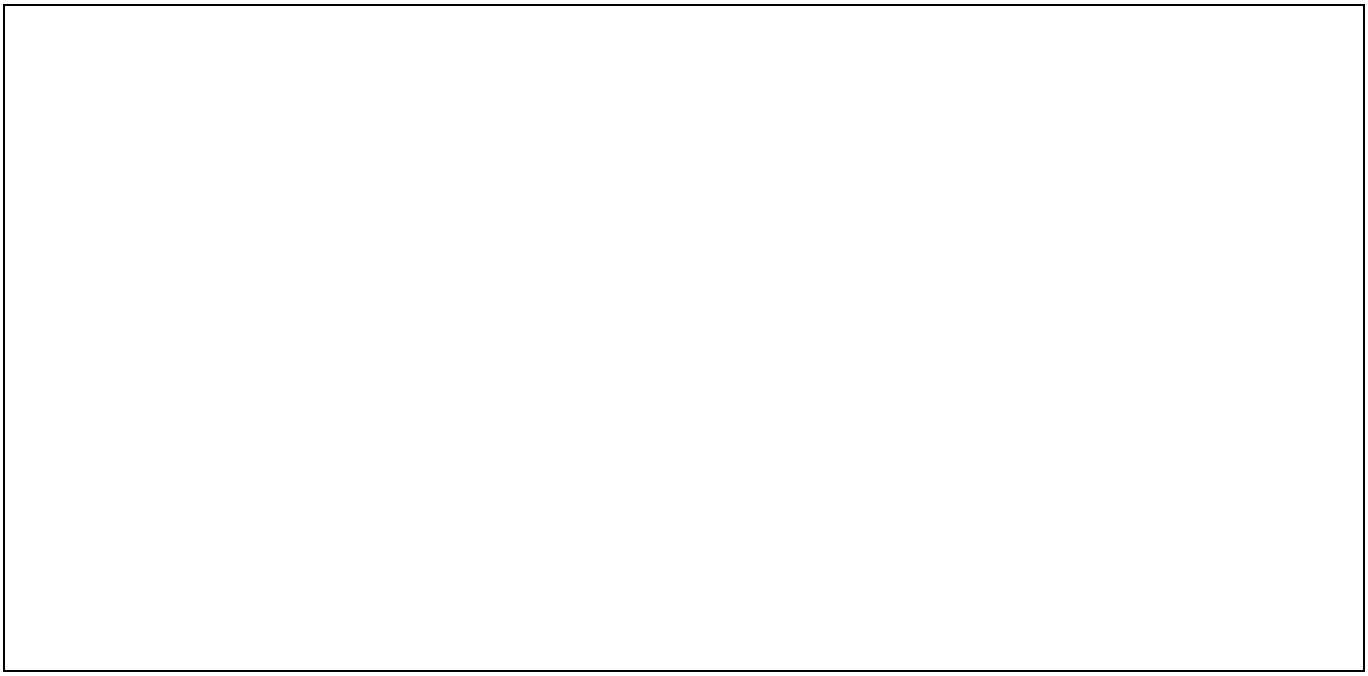

Fig. 4. Reddening residuals (in the sense $E(B-V)_{\rm model} - E(B-V)_{\rm node}$) *vs.* Galactic position for Model-A. Panels (a) and (b) indicate the reddening residuals *vs.* Galactic longitude and latitude respectively. Panels (c) and (d) show the reddening residuals *vs.* Heliocentric distance. In panels (a), (b) and (d) we have used $\delta A_{\rm v} = 0.5$ mag/kpc, while in panel (c) we have used $\delta A_{\rm v} = 1.5$ mag/kpc (see text for explanation).

Table 1 also indicates the effect of changing $R_{\rm v}$ for the case when $\delta A_{\rm v}$ is fixed to 0.5 mag/kpc. The effect on the derived dispersion is minimal, even when changing $R_{\rm v}$ by as much as 13%. In terms of residuals, there is very little difference when changing $R_{\rm v}$ for $r < 3-4$ kpc. The trend we find is that a larger $R_{\rm v}$ predicts somewhat smaller model reddenings (i.e., a more negative residual) for $r > 4$ kpc, thus allowing for a larger value of $\delta A_{\rm v}$. This is expected, since the quantity of interest is actually the differential reddening, which is the ratio between $\delta A_{\rm v}$ and $R_{\rm v}$. The lack of sensitivity of the reddening model values to the exact value of $R_{\rm v}$ is important in view of the rather large sensitivity of our model starcounts to this parameter, as shown in Sect. 3.2. Figures 5a-b show the residuals *vs.* Heliocentric distance for these two extreme values of $R_{\rm v}$, it is evident that the differences in the distribution of residuals is minimal.

We have also varied the values of $h_{\rm red}$ and $Z_{\odot}$ within considerable limits. Since these parameters enter only in the "smooth" component of the weights, as described in Sect. 2.5.3, they have a rather small impact on the computed residuals. Table 1 lists our results for some extreme cases of these parameters, along with the computed dispersion.

We find no clear trend in the reddening residuals *vs.* Galactic position or Heliocentric distance for different values of $Z_\odot$. For $h_{\rm red} = 50$ pc there seems to be a small downward trend in the range $1 < r < 2$ kpc and then a flattening at larger distances, while for $h_{\rm red} = 200$ pc there seems to be a small upward trend for $r > 3$ kpc, although these features are not very pronounced (see Figs. 5c-d). As for the dependence on $Z_\odot$ (Figs. 5e-f), we find very little dependence on this parameter, with an indication of a slight upward trend for $r > 4$ kpc when $Z_\odot = 40$ pc. As a consequence, we can not constrain these parameters from these data alone. It is not surprising that this test is not sensitive, in particular, to $h_{\rm red}$ because our node points are mostly located at $b \sim 0^\circ$, and therefore the dependence on height above/below the Galactic plane is greatly reduced. Therefore, in what follows, we have adopted the values of $h_{\rm red} = 110$ pc and $Z_\odot = +7$ pc, as indicated in Sect. 2.2, and in Méndez & van Altena (1996) respectively.

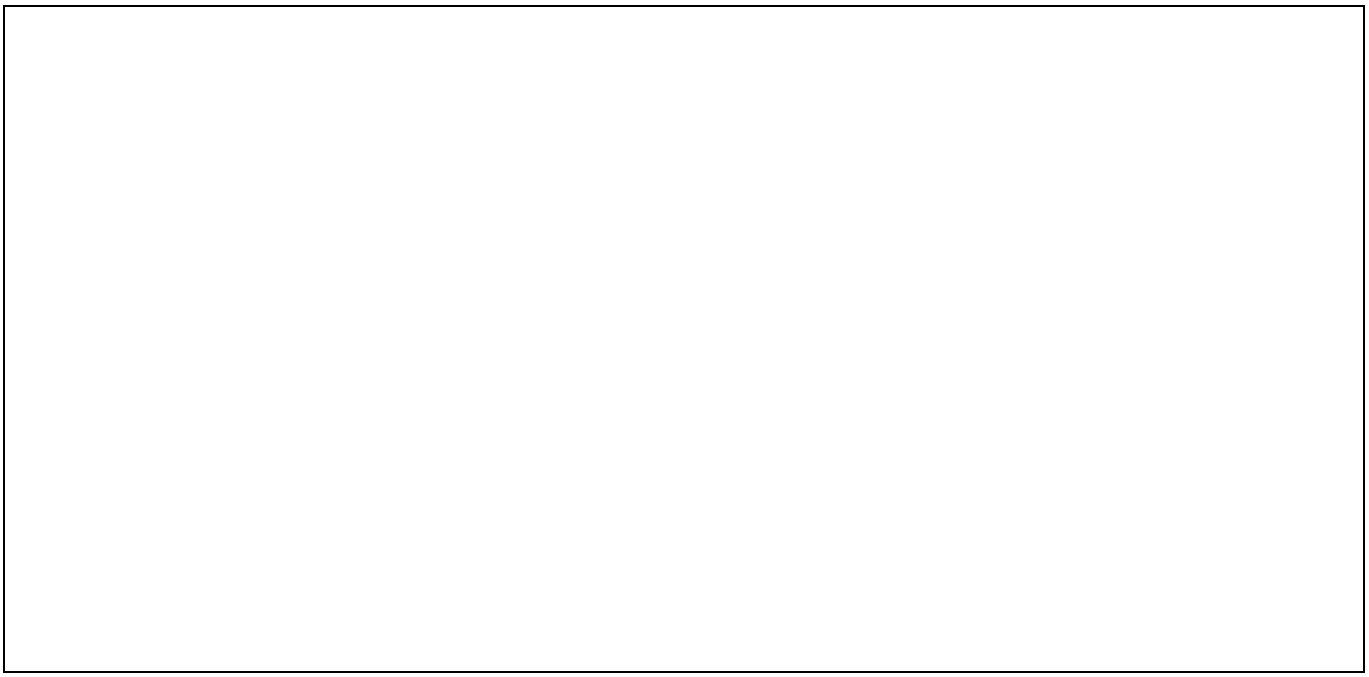

Fig. 5. Reddening residuals *vs.* Heliocentric distance. Panels (a) and (b) show the reddening residuals for $R_{\rm v} = 2.8$ and $R_{\rm v} = 3.6$ respectively. Panels (c) and (d) show the reddening residuals for $h_{\rm red} = 50$ pc and $h_{\rm red} = 200$ pc respectively. Finally, panels (e) and (f) show the reddening residuals for $Z_\odot = 0$ pc and $Z_\odot = 40$ pc respectively (see Table 1).

As for the distance-weighting function $f(\delta S)$ in Eq. (9), we have tried different functional forms, and have chosen the one that minimizes the overall scatter. Table 1 indicates the mean residual values for different functional forms, adopting $\delta A_{\rm v} = 0.5$ mag/kpc. We have tried inverse-linear, inverse-square, inverse-cubic, and exponentially-decaying weights (see Fig. 6). In all cases (except the exponentially-decaying weight) we have used a softening parameter of 1 pc, the exponential-decay was given a scale-length of 1 pc as well. The best result is obtained with the inverse-linear weight (indeed, Models A-1 through A-8 in Table 1 were performed precisely with this weighting scheme, with the best inverse-linear solution being Model A-2). The inverse-square, inverse-cubic, and exponentially-decaying weights exhibit an intrinsically larger scatter as a function of distance, and they also exhibit an upward trend in the residuals for distances larger than 4 kpc. Since for these models we have already adopted a small value of $\delta A_{\rm v}$ it seems unlikely that this upward trend is the result of an inadequate value for this parameter, but rather it shows the inadequacy of these weights. We have also tried no-distance weights at all (i.e., $f(\delta S) = 1$). In this case (see Table 1, Model A-12), the residuals are larger than for the inverse-distance weight and there is a small *downward* trend in the residuals *vs.* distance. By increasing the value of $\delta A_{\rm v}$, as indicated in Table 1 (Models A-13 & A-14), the residuals do decrease slightly, but are still larger than for an inverse-linear weight. For values of $\delta A_{\rm v} > 1.0$ mag/kpc the residuals wiggle, going downwards in the range 2 kpc $< r <$ 3 kpc and then upwards for $r > 3$ kpc. Also, as it can be seen from Table 1, the mean value of the residual is not zero, indicating a systematic offset between the model predictions and the observed values. This offset is not present when using *any* distance-weighting.

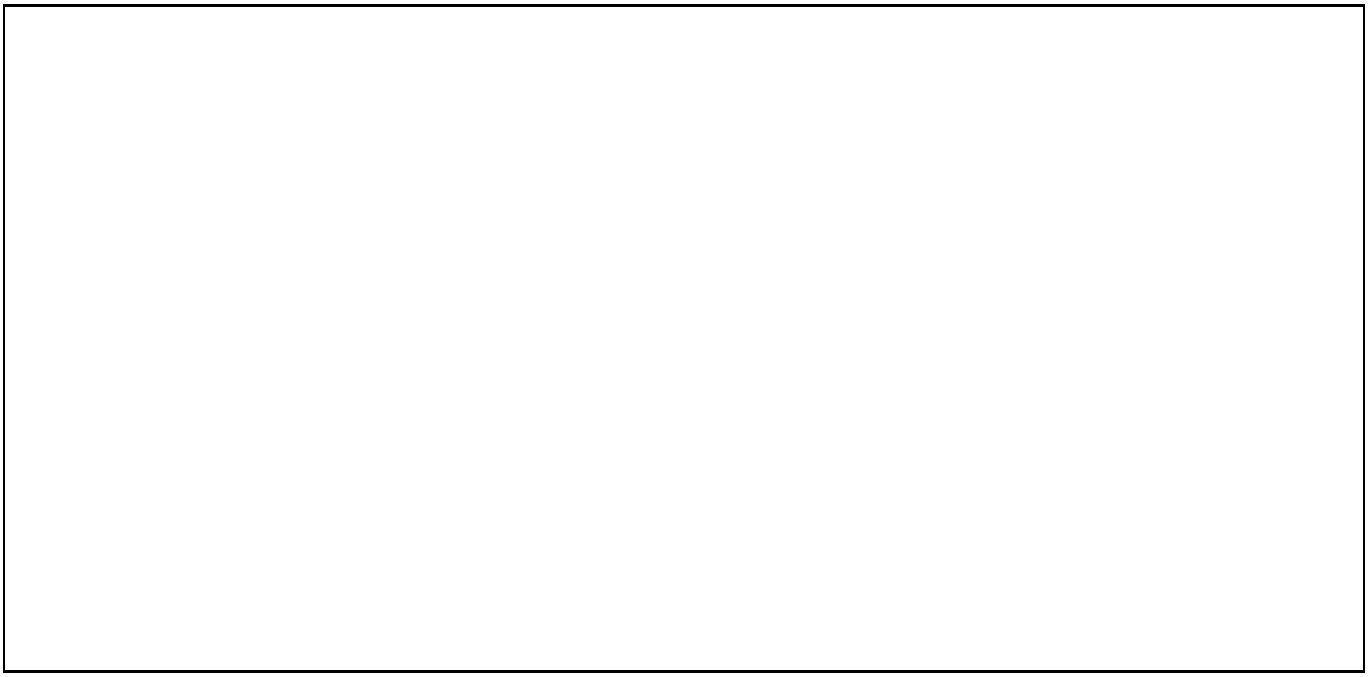

Fig. 6. Reddening residuals *vs.* Heliocentric distance. Panels (a) and (b) show the reddening residuals for an inverse-square and an inverse-cubic weight respectively. Panel (c) shows the reddening residuals for an exponentially-decaying weight. Panels (d), (e) and (f) show the reddening residuals for no distance weight with $\delta A_{\rm v} = 0.5$, 1.1, and 1.5 mag/kpc respectively (see text for details).

From the results presented in the preceding paragraph we conclude that the best weighting scheme is that of an inverse-linear weight. It is interesting to notice that there might be a physical reason for this: In an extensive study of the Rosette and Maddalena-Thaddeus Molecular Clouds (the latter discovered by Maddalena & Thaddeus 1985), Williams (1995, see also Williams et al. 1995) has shown that the (line-of-sight) *column density* of ^{13}CO in individual clumps can be fit by a power law of the type $N_{^{13}{\rm CO}} \sim 1/(1+r/0.7$ pc), close to what one might expect for the projection of an isothermal clump with $\rho(r) \sim 1/r^2$, where $\rho(r)$ is the volume density in the clump. Since our reddening values are directly related to the column density of absorbing material, the fact that our best weighting scheme corresponds to that found by Williams for isolated clouds indicates that the overall reddening is, *on the mean*, caused by clouds with the same density profiles as those studied by Williams, with a typical core-radius (our "softening parameter") close to 1 pc. We should also point out that Williams' results hold for pressure-bound, gravitationally-bound, and star-forming clumps, with minor differences in the slopes of the projected column-density for these different clouds.

The histogram distribution of the (slice averaged) residuals is shown in Fig. 7. The mean of the rms value for all longitude slices turns out to be 0.23 mag in $E(B-V)$ (Table 1, Model A-2), with few outliers, as evidenced by the ratio of the mean of the rms values to the mean of the absolute dispersions (0.20 mag). The ratio of these two values should approach asymptotically to 1.25 (Meyer 1975) for a Gaussian function, as it is indeed the case for our model. This rms value has to be regarded as a measure of the intrinsic clumpiness of the reddening in the reddening maps rather than as an estimation of the correctness of the weighting or interpolation scheme itself. We would expect, e.g., that this rms value will decrease as the node points become denser through the incorporation of more extensive reddening surveys. Our reddening model seems to have a substantially larger scatter than that of the extinction model by Arenou et al. (1992), who report a standard deviation of 0.14 in $E(B-V)$ by comparing predicted to observed colors for stars observed with the Hipparcos star mappers. Our comparisons to starcounts at low-Galactic latitudes seem to indicate, however, that our model gives a better match than the Arenou et al. model to the observed starcounts (see Sect. 3.2).

2.6.2. Tuning Model-B

We follow the same analysis as for Model-A, noticing that in Model-B we have one less degree of freedom, since $\delta A_{\rm v}$ in Eq. (6) is now determined by the last reddening point (see discussion on Sect. 2.5.2).

Table 1. Mean reddening residual & dispersion for Model-A.

Model	$< Res >$	σ_{Res}	Comments
A-1	-0.03	0.25	$\delta A_{\rm v} = 1.5$ mag/kpc
A-2	-0.07	0.23	$\delta A_{\rm v} = 0.5$ mag/kpc
A-3	-0.07	0.23	$R_{\rm v} = 2.8$ mag
A-4	-0.07	0.23	$R_{\rm v} = 3.6$ mag
A-5	-0.08	0.24	$h_{\rm red} = 50$ pc
A-6	-0.06	0.23	$h_{\rm red} = 200$ pc
A-7	-0.07	0.23	$Z_{\odot} = 0$ pc
A-8	-0.06	0.23	$Z_{\odot} = 40$ pc
A-9	-0.02	0.24	inverse-square weight
A-10	+0.01	0.25	inverse-cubic weight
A-11	+0.03	0.28	exponentially-decaying weight
A-12	-0.15	0.27	no weight, $\delta A_{\rm v} = 0.5$ mag/kpc
A-13	-0.14	0.23	no weight, $\delta A_{\rm v} = 1.1$ mag/kpc
A-14	-0.13	0.23	no weight, $\delta A_{\rm v} = 1.5$ mag/kpc

Fig. 7. Histogram of reddening residuals. The estimated rms value for the dispersion is 0.23 mag in $E(B-V)$.

In Table 2 we indicate the mean residual difference and the residual dispersion between the model and the predictions. We find the same trends as for Model-A, indicating that our tuning is nearly independent of the more distant (and, therefore, uncertain) node points (with the possible exception of $\delta A_{\rm v}$ which is determined mainly by the more distant node points, see the previous section). In particular, the dependency on the distance-weighting function is much stronger in this case, with a clear indication that the best weighting is that of an inverse-linear relation (compare model B-1 to models B-8, B-9, B-10 & B-11). The overall dispersion of our best Model-B (B-1, with 0.25 mag) is only slightly larger than that for our best Model-A (A-2 with 0.23 mag).

In Fig. 8 we show the residuals as a function of Galactic position and Heliocentric distance for model B-1. No curvature on the residuals as a function of distance is seen (compare with Fig. 4c), which shows the relative advantage of using the more self-consistent extrapolation to larger distances in Model-B rather than the adoption of a fixed

reddening slope beyond the last node point, as done in Model-A. The histogram of residual values is similar to that of Model-A, and it is not shown here.

Table 2. Mean reddening residual & dispersion for Model-B.

Model	$< Res >$	σ_{Res}	Comments
B-1	-0.05	0.25	standard
B-2	-0.05	0.25	$R_{\rm v} = 2.8$ mag
B-3	-0.05	0.25	$R_{\rm v} = 3.6$ mag
B-4	-0.08	0.24	$h_{\rm red} = 50$ pc
B-5	-0.04	0.26	$h_{\rm red} = 200$ pc
B-6	-0.06	0.25	$Z_{\odot} = 0$ pc
B-7	-0.04	0.26	$Z_{\odot} = 40$ pc
B-8	-0.20	0.31	inverse-square weight
B-9	-0.22	0.33	inverse-cubic weight
B-10	-0.22	0.33	exponentially-decaying weight
B-11	+0.05	0.32	no weight

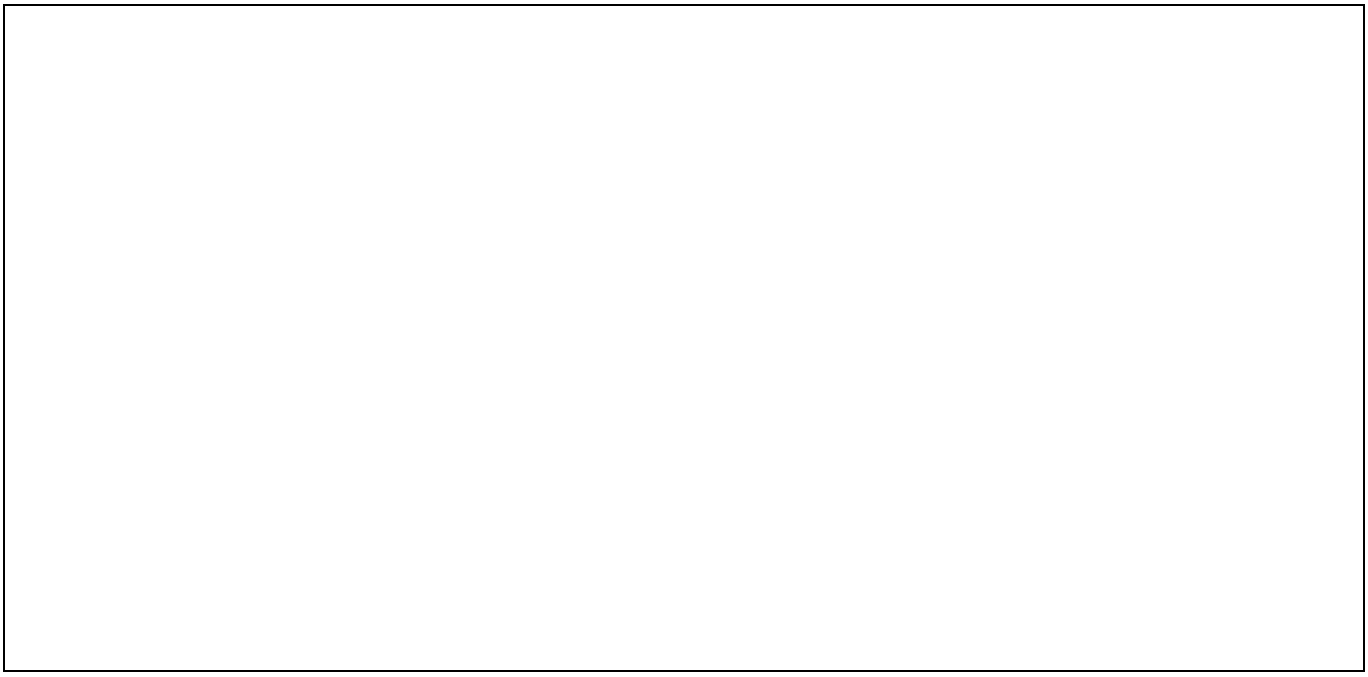

Fig. 8. Reddening residuals (in the sense $E(B-V)_{\rm model} - E(B-V)_{\rm node}$) *vs.* Galactic position for our best Model-B. Panels (a) and (b) indicate the reddening residuals *vs.* Galactic longitude and latitude respectively. Panel (c) shows the reddening residuals *vs.* Heliocentric distance.

2.7. Comparisons to independent measurements of reddening

As emphasized by Jønch-Sørensen (1994), a weighting & interpolation scheme as the one described above should give an accurate description of interstellar reddening for fields covering a long path through the disk or for large solid-angles, so that small scale inhomogeneities in the distribution of dust tend to average out. In Sect. 2.3 we already discussed the uncertainties in the predicted values of reddening from our model for intermediate-to-high Galactic latitudes. In

this section we briefly comment on the adequacy of our model for low Galactic latitudes, while more detailed tests are performed through comparisons to starcounts in the Galactic plane, as described in the following section.

Jønch-Sørensen & Knude (1994) have presented a determination of the reddening up to a distance of about 8 kpc for a field at $(l, b) = (262^{\circ}, +4^{\circ})$ using deep uvbyHβ photometry covering an area of 145 $\Box'$. In Fig. 9 we show the observed upper and lower envelope of reddening *vs.* Heliocentric distance as derived from their study (their Fig. 5c), as well as the predictions from our model. In this comparison we have used Model-B (which, in fact, gives similar results than Model-A for distances closer than about 5 kpc). From Fig. 9 we clearly see that our method agrees quite well with the observed *upper* envelope. On the other hand, a model that does not incorporates the BH maps clearly overestimates the reddening, showing the need of using these maps even at these low latitudes as an extra constraint (see also Sect. 2.5). Jønch-Sørensen & Knude emphasize that the distribution of reddening across their (small) field-of-view is certainly not homogeneous, and that there might be at least two small dense clouds in the field with sizes of order $5' \times 5'$. Given these uncertainties, the agreement between our model and the upper envelope is quite good. We also notice that the upper (observed) envelope suggests a slope of about 0.34 mag/kpc in E(B-V) for Heliocentric distances smaller than 2 kpc, in agreement with the results by Knude (1979) who finds, from a multicolor study of 63 Selected Areas, that the reddening from a single average cloud is $E(b - y) = 0.03$, with 6 to 8 clouds per kpc along the line-of-sight.

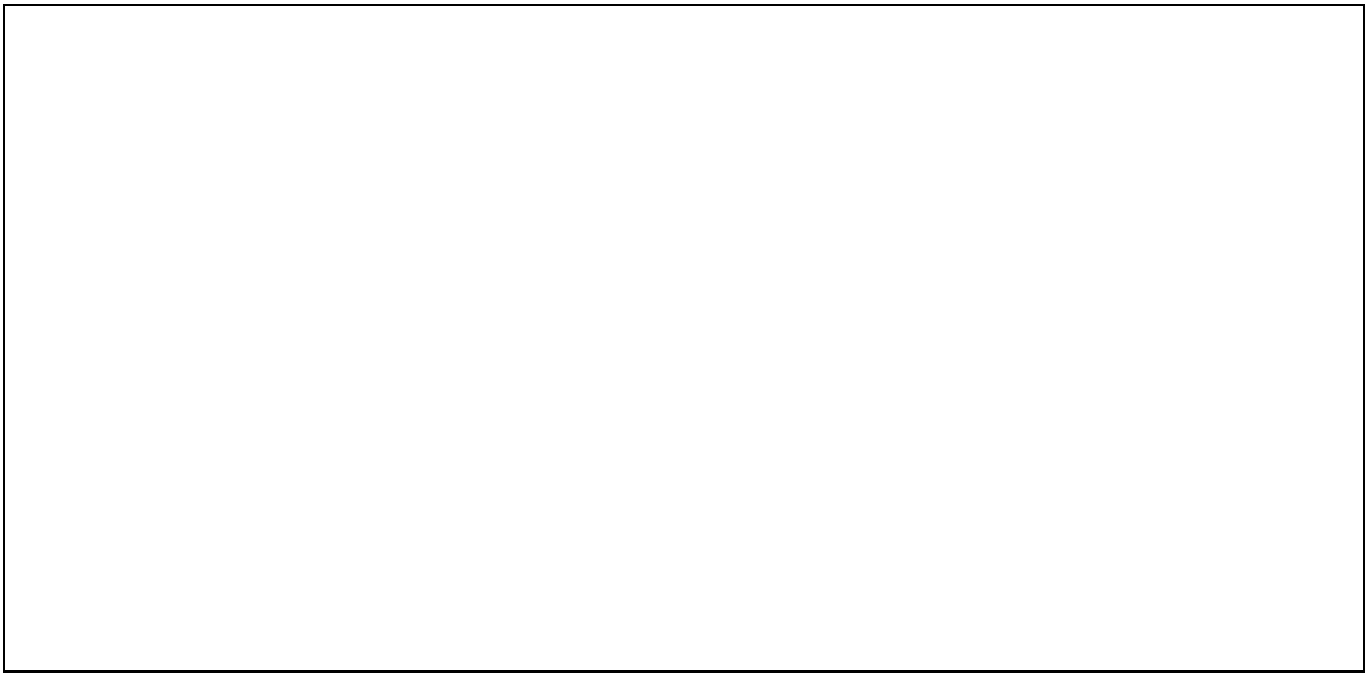

Fig. 9. Reddening *vs.* Heliocentric distance for a field located at $(l, b) = (262^{\circ}, +4^{\circ})$. Solid lines indicates the upper and lower envelope of the observed reddening as derived by Jønch-Sørensen & Knude (1994) and adopting $E(B - V) = 1.35E(b - y)$ from Crawford (1975). The dashed line is our Model-B, while the dot-dashed line indicates the predictions if the BH maps are not included in the interpolation.

3. Starcounts at low Galactic latitude: The Guide Star Catalogue

3.1. Selection of the Guide Star Catalogue Fields

Perhaps one of the largest modern photographic surveys available at low-Galactic latitudes is contained in the Guide Star Catalogue (Lasker et al. 1990, GSC hereafter). This catalogue, covering the whole-sky, contains calibrated photometry obtained from PDS microdensitometer measurements of Schmidt plates taken mainly at Siding Spring (SERC-J, UK-Schmidt Telescope, Cannon 1984) and Mount Palomar (Quick-V, Oschin-Schmidt, Minkowski & Abell 1963, Reid et al. 1991).

We have chosen a number of fields from the GSC to test our reddening model. The predictions from a starcount model (Méndez & van Altena 1996, Méndez et al. 1996) are compared to actual star counts toward these selected low-Galactic latitude regions having different amounts of reddening. These comparisons allow us to test the extent to which the assumptions embedded in the reddening model are appropriate, and provide also an indication of the correctness of our representation of the stellar populations contributing to the counts.

For our comparisons we have selected fields with plates from the *supplemental survey plate collection*. These plates are not part of the standard Palomar or SERC surveys, but were included for the purpose of providing uniform sky coverage. Among these, we have selected the short-exposure V plates (designated as XV on Table III of Lasker et al. 1990) taken with the UK-Schmidt Telescope. These plates have superior image quality which, along with their short-exposure time (240 sec), greatly reduce confusion and classification problems, especially severe at low-Galactic latitudes (Bernacca et al. 1992, Lattanzi 1994 private communication). We have also looked at two other fields from the northern Quick-V (QV) survey for completeness, but in this case we have restricted our selection to only those fields with plates of the type Pal-V4 which match the photometric response function of the XV plates. The full collection of XV plates might prove to be quite valuable for Galactic structure studies at low-latitudes but it has, of course, limited sky coverage. The complete sample of XV plates with $|b| < 10^{\circ}$ available from the GSC is shown in Fig. 10, along with an indication of the fields selected in this study.

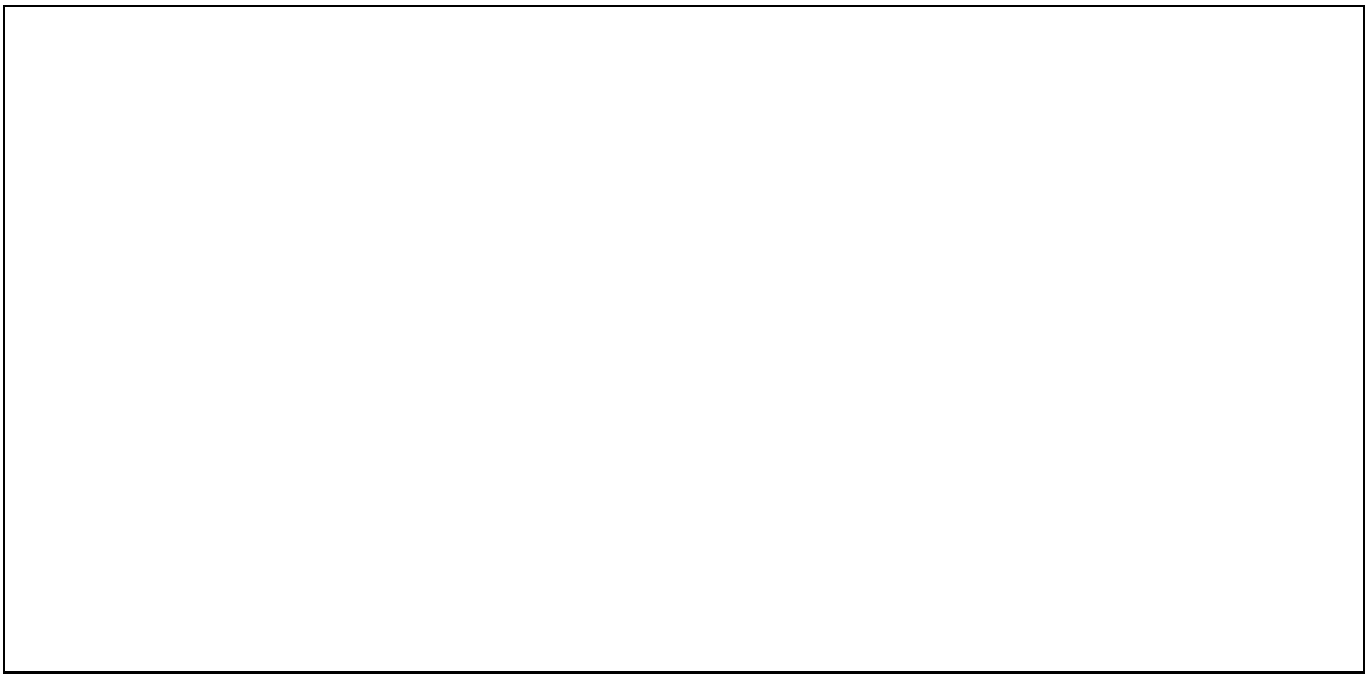

Fig. 10. Distribution on the Galactic plane of the GSC supplemental plate collection from the UK-Schmidt Telescope (open squares, not to scale). The fields selected for this study are marked with an X within the open square. Two other plates, from the Palomar Quick-V survey, have been selected as well, these are indicated as filled squares.

Six regions with centers at $|b| < 10^{\circ}$ have been selected from the GSC to compare with our model predictions (Fig. 10). In all cases only the $3^{\circ} \times 3^{\circ}$ central area from each plate has been extracted in order to minimize systematic as well as random errors in the photographic photometry which are present in regions far from the plate's photometric sequence, usually located in the central area of the plates (Ratnatunga 1990, Bernacca et al. 1992). The selected solid angle is a compromise value that provides sufficiently good number statistics (typically a few thousand stars), and small photometric errors (typically smaller than 0.3 mag in V for the selected regions). These six selected regions have varying amounts of (predicted) reddening and, therefore, provide a good test case in a wide variety of conditions with regards to both the amount and distribution of the reddening material along the line-of-sight. Figure 11 shows the reddening *vs.* Heliocentric distance for the selected fields, using the extrapolation method of Model-A (which, as discussed on Sect. 2.7, gives nearly the same results as for Model-B for distances closer than about 5 kpc). We have also compared our reddening model to the predictions of the extinction model by Arenou et al. (1992). Arenou's

values (from his Eq. (5) and (5bis), and the parameters given in the Appendix of their paper) are also shown in Fig. 11. We should emphasize that, as a consequence of our local, rather than global and analytic, treatment of the reddening, the reddening values derived from our model, and plotted in Fig. 11, do not reflect, necessarily, the overall value of $E(B-V)$ for the whole $3^{\circ} \times 3^{\circ}$ starcount region, but only the values for the *field center* as given in Table 2. Nevertheless, Fig. 11 gives an indication of the the nature and amount of error in the reddening estimation that one might expect from these type of models.

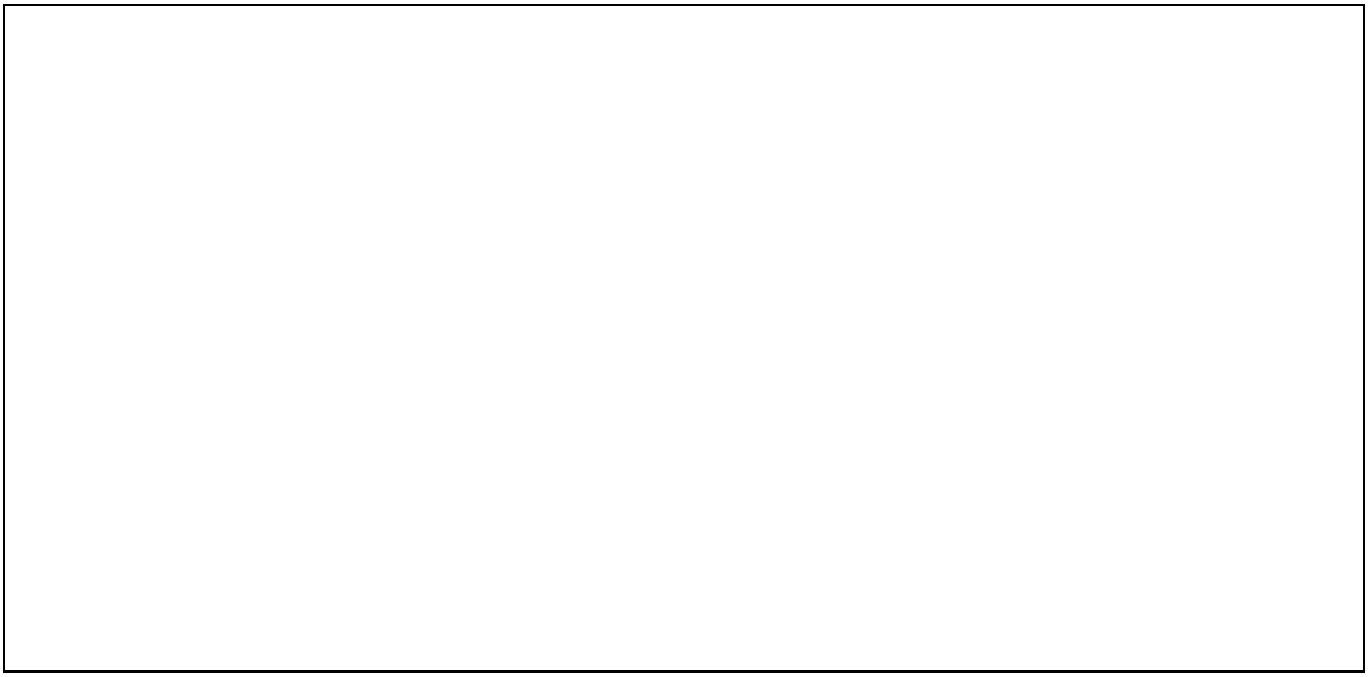

Fig. 11. Predicted reddening values for the selected regions. Regions are numbered according to the ID given in Table 2. The solid line indicates our model predictions, while the dotted line indicates the prediction from the extinction model by Arenou et al. (1992) scaled to $E(B-V)$ using $R_{\rm v}$= 3.2.

Starcount data for our chosen fields have been obtained from the GSC, version 1.2, available on the WWW (http://www-gsss.stsci.edu/gsc12/gsc12.html), for magnitudes brighter than $V \approx 15$. To avoid extrapolated photometric values, we have restricted our comparisons to the range $V > 8$, compatible with the brightest stars in the photometric sequences. Only objects classified as stars were included in the counts. Of course, at these bright magnitudes and low-Galactic latitudes, compact galaxies misclassified as stars do not contribute to the starcounts. On the other hand, our comparisons will be restricted to the magnitude range where the counts are complete, this is typically more than one magnitude *brighter* than the magnitude limit of the plates. Therefore, misclassification due to poor signal-to-noise, close blends, or plate defects is likely to be very small (Jenkner et al. 1990).

Table 3 summarizes the properties of the selected GSC1.2 fields. The first four columns indicate a running identification number, the GSC source for the field, and the Galactic longitude and latitude for the center of the field-of-view. The fifth column ($E(B-V)_1$) indicates the predicted reddening in $(B-V)$ at a Heliocentric distance of 1 kpc, as computed from our reddening model, the sixth column (V_{lim}) indicates the completeness limit for the GSC starcounts, and the seventh column indicates the observed (error-convolved) number of stars from the GSC1.2 in the magnitude range $8 \leq V < V_{lim}$. Finally, the last column indicates a generic name for the selected regions, with a reference to optical and/or submillimetric studies from where the denomination has been extracted.

We should emphasize that the photometry from the GSC is in the "natural system" of each filter-emulsion combination. Therefore, for the XV plates (emulsion IIaD, filter GG495), V refers only to an approximation to Johnson's V, and the same is true for the Pal-V4 plates (with the same emulsion-filter combination). Therefore, in what follows, whenever we mention V photometry it must be understood that we are referring to the "natural" passbands of these plates. We should also emphasize that all our model predictions (see Sect 3.2) have been converted to the photometric

Table 3. General properties of our selected GSC1.2 fields.

Region ID	Source	l deg	b deg	$E(B-V)_1$ mag	V_{lim} mag	N_{obs} $[8 \leq V < V_{lim}]$	Comments
1	XV807	27.6	-0.4	0.66	12.2	1 072	Aquila Rift[a]
2	QV-N338	67.7	-0.1	0.37	12.2	1 771	Cygnus Rift[a,b]
3	QV-N158	160.8	5.9	0.43	13.7	3 449	Auriga-Gemini[b]
4	XV168	283.5	2.2	0.16	12.2	2 392	Vela-Carina[a,c]
5	XV127	284.2	-3.4	0.13	12.2	3 023	Vela-Carina[a,c]
6	XV455	358.6	0.3	0.13	12.2[d]	1 020	Scorpio [a]

[a] From Dame & Thaddeus (1985).
[b] From Deutschman et al. (1976).
[c] From Dame et al. (1987).
[d] The completeness magnitude limit for this Region is undefined, see Sect 3.2.

systems of the plates, by using the following transformation (Lasker et al. 1990, Table I, and Russell et al. 1990, Eq. (1)):

$$V_{495} = V - 0.10(B-V) \tag{16}$$

Notice that, in the above equation, all quantities are reddened and extincted.

3.2. Starcounts and the reddening model

The starcounts model described by Méndez & van Altena (1996) has been used, along with the reddening model described above, to compute the expected counts in the selected fields. Because of the rather large solid angle covered by each plate, and because of the discrete nature of the reddening material, some experimentation was needed to decide upon the best angular resolution to employ in the integration scheme in the starcounts model. It was found that, for a resolution higher than 0.5° in both RA and DEC, the predicted counts from the model varied by less than 2%. Therefore, we adopted this angular resolution. It must be emphasized that a finer angular resolution could easily be performed with the model, but then the required CPU time becomes increasingly large, making these computations impractical (e.g., already, at 0.5° resolution, the model has to be evaluated at 36 positions within each Region). Our adopted angular resolution *oversamples* the mean angular resolution of our reddening maps (see Sect. 2.4, and Fig. 2), so that there is no loss of information from the reddening maps when adopting this angular resolution. Also, we have adopted Model-A for extrapolation at larger distances although, in practice, it does not make any difference for this application to use either Model-A or Model-B because both models give nearly the same reddening at distances smaller than about 5 kpc (see Sect.3.1), while most of the starcounts analyzed here are contributed by objects closer than about 2 kpc (see Sect. 3.3). The adoption of Model-A over Model-B has been guided by the greater simplicity of the former, and a faster implementation of the algorithm (compare Eq. (6) for Model-A with Eq. (7) for Model-B), although for general applications Model-B would lead to better predictions than Model-A for reasons that were explained in Sect. 2.5.2. The Galactic structure parameters employed in our computations are those described in Méndez & van Altena (1996, Table 1), unless otherwise specified.

Starcounts *vs.* magnitude for the selected regions are shown in Fig. 12. The predicted counts are for the standard parameters of the reddening procedure as outlined in the previous sections. These comparisons indicate a very good agreement between the predicted and observed starcounts in the magnitude range $8 \leq V < 14.5$, especially when considering the model predictions for the case of no-reddening. Table 4 indicates the observed starcounts within the magnitude range where the counts are complete (i.e., $8 \leq V < V_{lim}$, from Table 3) and the predicted starcounts by the model without (Run 1) and with (Run 2) reddening, in the same magnitude range. The last two columns in Table 4 indicate the mean fractional difference between the observed and model starcounts, as well as the mean of the absolute dispersion, both with their standard deviation.[4] It can be seen that, despite a reduction factor of up to 15 in the predicted counts from a model without reddening to a model including reddening, the (absolute) agreement is around

[4] In Tables 4 and 5 the values quoted in the last two columns *exclude* Region 6 for reasons that will become apparent afterwards.

20%, with a mean value of 11% (except in the case of Region 6 at $(l, b) = (358.6^{\circ}, +0.3^{\circ})$ which will be discussed later).

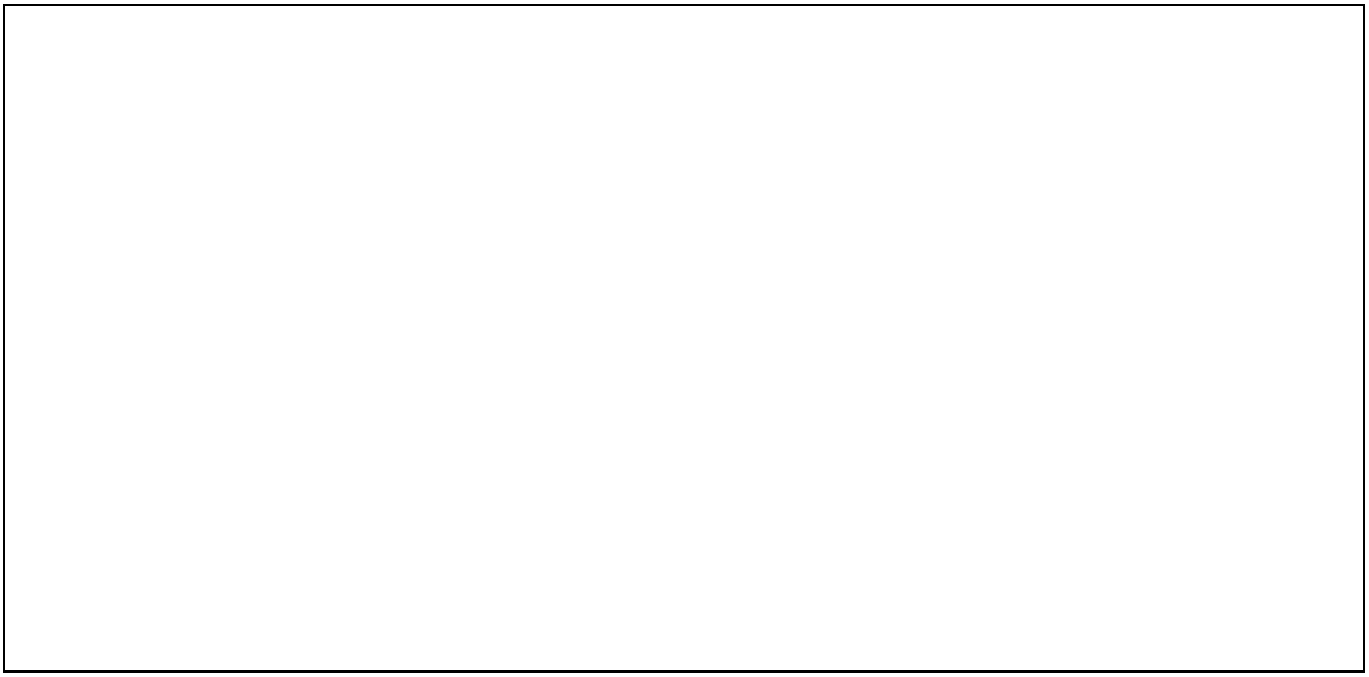

Fig. 12. Observed (dots with Poisson error bars) and predicted (lines) starcounts in our selected regions. The solid line indicates the predicted counts for no-reddening (Run 1), while the dotted line indicates the predictions using the model described in Sect. 2 (Run 2).

Starcounts in our selected fields are somewhat sensitive to the value of $R_{\rm v}$. It is well known (Gutiérez-Moreno & Moreno 1975) that $R_{\rm v}$ is as function of, both, the spectral energy distribution of the stars considered, and the amount of reddening itself. Figure 13 shows the results of adopting the (mean) relationship for $R_{\rm v}$ given by Schmidt-Kaler (1982):

$$R_{\rm v} = 3.30 + 0.28(B-V)_{\rm o} + 0.04E(B-V) \tag{17}$$

By comparing Figs. 12 and 13 (see also Table 4), it is evident that we obtain a better fit to the observed counts by using $R_{\rm v}$ as per Eq. (17), rather than a constant value. The dependency on $R_{\rm v}$ is not surprising, in view of the large amount of reddening present in some of our fields. Indeed, it is clear from Fig. 13 that the dependency on $R_{\rm v}$ is larger for those fields with larger overall reddening (Table 3 and Fig. 11). Schmidt-Kaler cites regional variation of $R_{\rm v}$ amounting to ± 0.2. In Fig. 13 (see also Table 4) we show the effect of changing $R_{\rm v}$ within these margins. The effect of these changes is rather small, and it suggests that a better overall model is indeed obtained with an $R_{\rm v}$ that is given by Eq. (17). Therefore, we have adopted this value of $R_{\rm v}$ for *all* our subsequent model runs.

At this point it is interesting to mention that the predictions of a model similar to that of Run 3 (which uses the $R_{\rm v}$ given by Eq. (17)), but using the extrapolation Model-B, leads to a mean difference in the counts for all six regions of only 1.7% with respect to Run 3, while the mean absolute difference is 4%. This shows that the use of Model-A, for this particular application, is guaranteed. However, comparisons to fainter starcounts would likely benefit from the use of Model-B instead, for the reasons presented in Sect. 2.5.2.

We have also investigated the effects on the predicted starcounts of changing the differential absorption and the scale-height of the reddening material, since these parameters were not well constrained by the tests described in Sect. 2.6. Figure 14 shows the results of our runs with $\delta A_{\rm v} = 1.5$ mag/kpc (Run 6 in Table 4), as well as the effect of changing $h_{\rm red}$ from 110 pc (Run 3 in Table 4) to a lower value of 50 pc (Run 7 in Table 4), and to an upper value of 200 pc (Run 8 in Table 4). From the last two columns on Table 4 it is apparent that the change of $\delta A_{\rm v}$ has a minor impact on the predicted counts. However, there is a tendency of the model with the larger value of $\delta A_{\rm v}$ to underestimate the counts, specially at the fainter magnitudes. This is a natural consequence of the excessive differential reddening

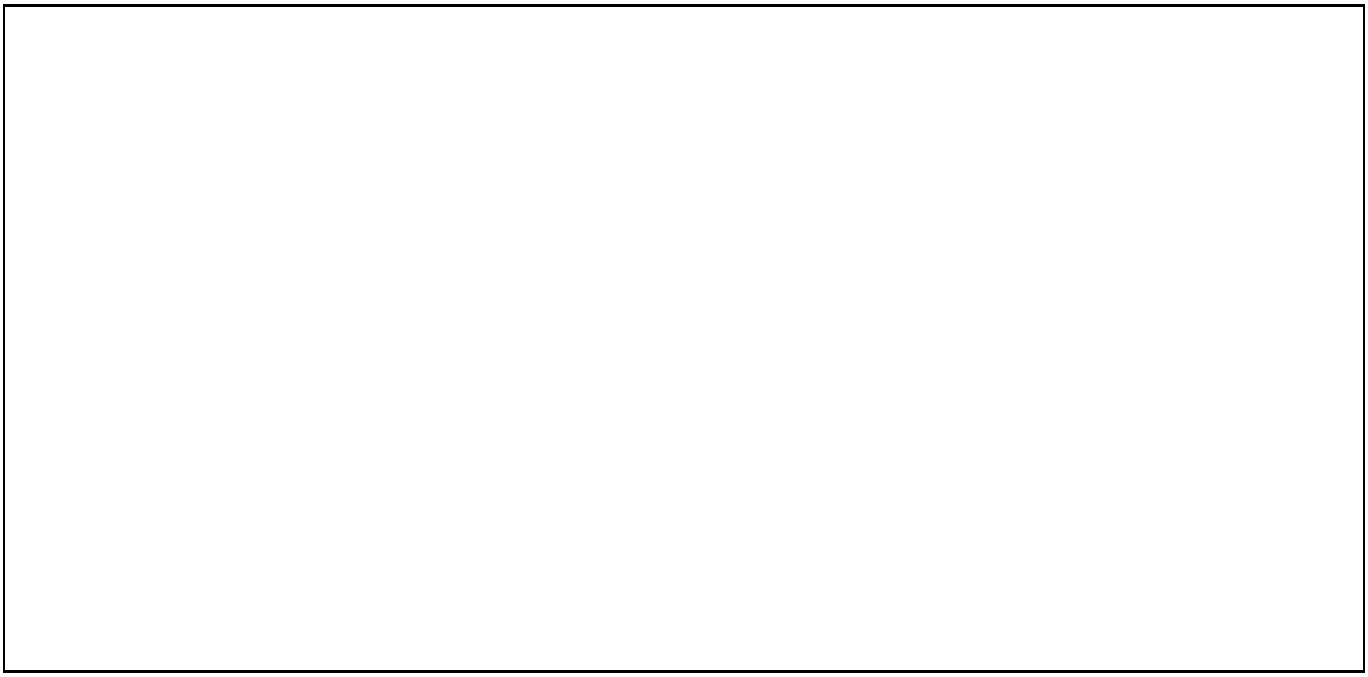

Fig. 13. Same as Fig. 12, except that $R_{\rm v}$ is as given by Eq. (17, solid line). A change on $R_{\rm v}$ of ± 0.2 is indicated with the dashed lines, with the upper predicted counts having the smaller value of $R_{\rm v}$.

Table 4. Predicted starcounts as a function of parameters in the reddening model.

Run	Reg. 1	Reg. 2	Reg. 3	Reg. 4	Reg. 5	Reg. 6	$<\frac{\Delta N}{N_{\rm Obs}}>^{\rm a,b}$	$<\frac{\lvert\Delta N\rvert}{N_{\rm Obs}}>^{\rm b}$	Comments[c]
Obs.	1 072	1 771	3 449	2 392	3 023	1 020	–	–	Measured values
1	22 164	12 530	7 925	7 231	6 099	30 134	6.0 ± 7.9	6.0 ± 7.9	No reddening
2	1 459	2 181	2 782	2 989	2 659	3 162	0.11 ± 0.25	0.23 ± 0.09	Std. params., $R_{\rm V} = 3.2$
3	1 296	1 977	2 489	2 780	2 510	2 888	0.01 ± 0.22	0.19 ± 0.06	$R_{\rm V}$ as in Eq. (17)
4	1 164	1 832	2 332	2 658	2 425	2 651	-0.06 ± 0.19	0.15 ± 0.11	$R_{\rm V}$ as in Eq. (17) +0.2
5	1 437	2 142	2 658	2 911	2 600	3 164	0.08 ± 0.25	0.23 ± 0.07	$R_{\rm V}$ as in Eq. (17) -0.2
6	1 234	1 814	2 215	2 745	2 509	2 644	-0.04 ± 0.22	0.17 ± 0.12	$\delta A_{\rm v} = 1.5$ mag/kpc
7	1 404	2 147	2 335	2 856	2 503	2 991	0.04 ± 0.28	0.24 ± 0.07	$h_{\rm red} = 50$ pc
8	1 234	1 882	2 757	2 744	2 539	2 764	0.00 ± 0.17	0.14 ± 0.05	$h_{\rm red} = 200$ pc
9	770	1 442	2 851	2 455	2 279	2 511	-0.17 ± 0.12	0.18 ± 0.10	Arenou et al. (1992) model

[a] ΔN is in the sense $N_{\rm Model} - N_{\rm Obs}$.
[b] These columns exclude Region 6, see text for explanation.
[c] The meaning of the different runs is discussed in the text. Here we give only a brief description.

implied by this value of $\delta A_{\rm v}$, suggesting that the value of 0.5 mag/kpc found in Sect. 2.6.1 is closer to the proper value. The lack of sensitivity of the predicted counts to this parameter is understandable because this differential reddening is only applied beyond the last node point in the reddening maps, which extend to distances beyond 2 kpc, while the mean distance of stars contributing to the observed counts is typically less than 2 kpc, reinforcing thus the adequacy of using Model-A for reddening extrapolation.

With regards to the scale-height of the reddening material, a higher value for $h_{\rm red}$ seems to provide a better overall solution in, both, the mean as well as the absolute residuals. As we shall see though (Sects. 3.3 and 3.4), there are other parameters that also have a large impact on the starcounts. Therefore, in what follows, we will still adopt our standard values of $\delta A_{\rm v} = 0.5$ mag/kpc and $h_{\rm red} = 110$ pc.

Our starcounts model also includes an option for the extinction model by Arenou et al. (1992). This model was developed to predict magnitudes and colors for stars in the Hipparcos Input Catalogue, which in many cases lacked

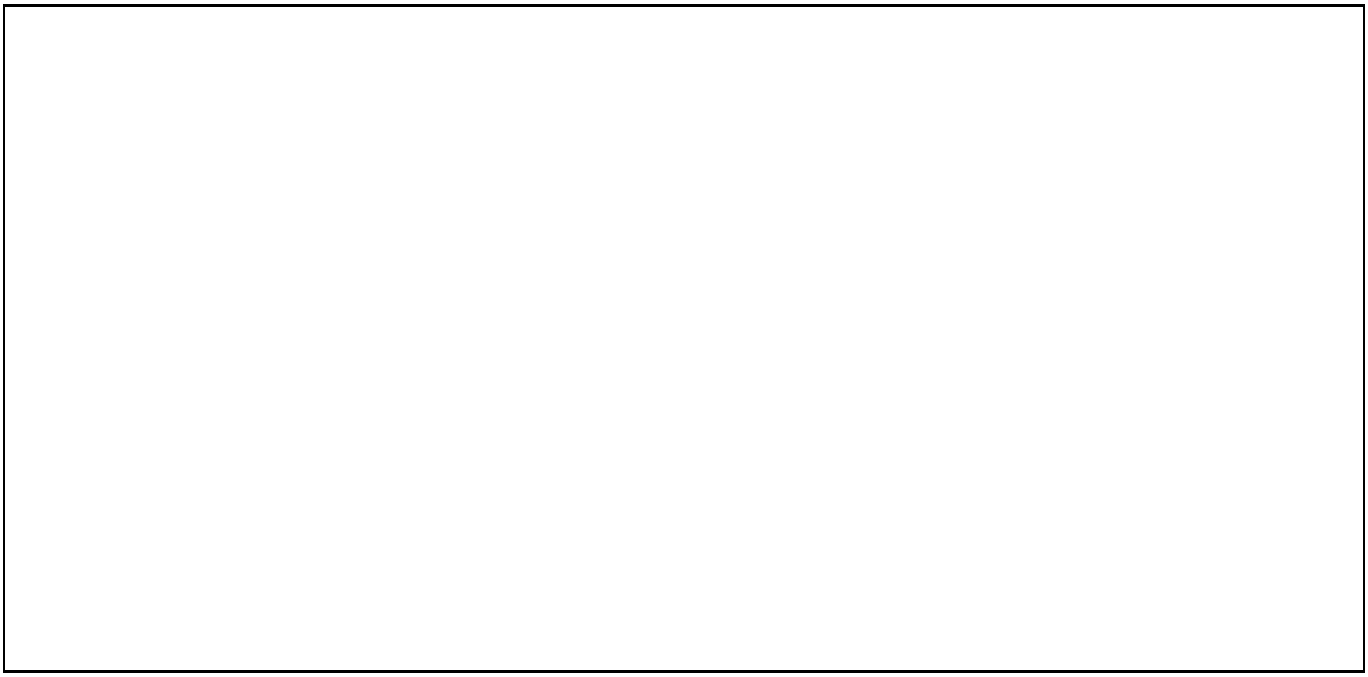

Fig. 14. Same as Fig. 13, except that $\delta A_{\rm v}$ has been increased to 1.5 mag/kpc (solid line). The dashed line indicates the run with a small $h_{\rm red}$ equal to 50 pc, while the dot-dashed line indicates the run with a large $h_{\rm red}$ equal to 200 pc, both having $\delta A_{\rm v} = 0.5$ mag/kpc, as in Figs. 12 and 13.

photoelectric photometry. The results of these computations, along with the results from Run 3, are indicated in Fig. 15 & Table 5. There is a very good correspondence between the starcounts predicted using our reddening model and Arenou's et al. model, specially when considering the rather large differences in the predicted reddening values between these two models shown in Fig. 11. However, it is also apparent from Fig. 15 (see also Table 4, Run 9) that Arenou's model predicts systematically *fewer* stars than observed, although the absolute dispersion with respect to the observed value is similar to that of our best runs (e.g., Runs 3 and 8), as indicated in the last two columns of Table 4. The discrepancies in the predicted starcounts between these two reddening models may be a consequence of the different approaches adopted: while Arenou's et al. model accounts for the large-scale properties of the reddening material, our model incorporates more accurately the intrinsic clumpiness of the absorbing material, giving therefore better results *on the mean* at low Galactic latitudes, even for very high-reddening regions. As a general statement we could say that the *absolute* deviation in the predicted starcounts from the observed values is somewhat smaller when using the model by Arenou et al. than our model. This is in agreement with the fact that Arenou et al. (1992) quote a *mean accuracy* for their model of about 40%, which for a reddening at 1 kpc of, e.g., 0.4 mag, leads to an uncertainty in the reddening of 0.16 mag, smaller almost by a factor of 1.5 than the estimated uncertainty of 0.23 mag for our model reddening values (see Sect. 2.6 and Fig. 7). However, the deviations between the starcounts computed with the model by Arenou et al. and the observed counts seem to be systematic and, therefore, even though their model leads to more precise starcounts, our model seems to lead to more accurate starcounts, in the classical statistical distinction between these two terms.

We must emphasize that Arenou et al. (1992) have adopted the mean $R_{\rm v}$ as given in Eq. (17) above. Since Arenou's model is an extinction model, rather than a reddening model, we have to adopt an iterative procedure to solve for $E(B-V)$ (and thus $({\rm B-V})_{\rm o}$) from their model $A_{\rm v}$ values and from the observed (B-V). This was needed in order to compute starcounts with our model, and it is a consequence of the dependence of $R_{\rm v}$ on both $(B-V)_{\rm o}$ and $E(B-V)$. The iterative procedure converged quickly, in only two or three iterations.

The discrepancy seen between the model predictions and Region 6 at $(l, b) = (358.6^{\circ}, +0.3^{\circ})$ (Figs. 13 – 15) is puzzling: on one hand the predicted reddening at 1 kpc is smaller than that of Region 1 at $(l, b) = (27.6^{\circ}, -0.4^{\circ})$ (Table 3), yet the observed number of stars in the latter is larger than that of the former, contrary to expectation. On the other hand, Region 6 should exhibit a higher stellar density than that of Region 1 (before any reddening correction) because of the exponentially decaying stellar density profile away from the Galactic center (this is indeed seen in the model excluding reddening on Fig. 12 and Table 4, Run 1). These two facts combined, point to a problem

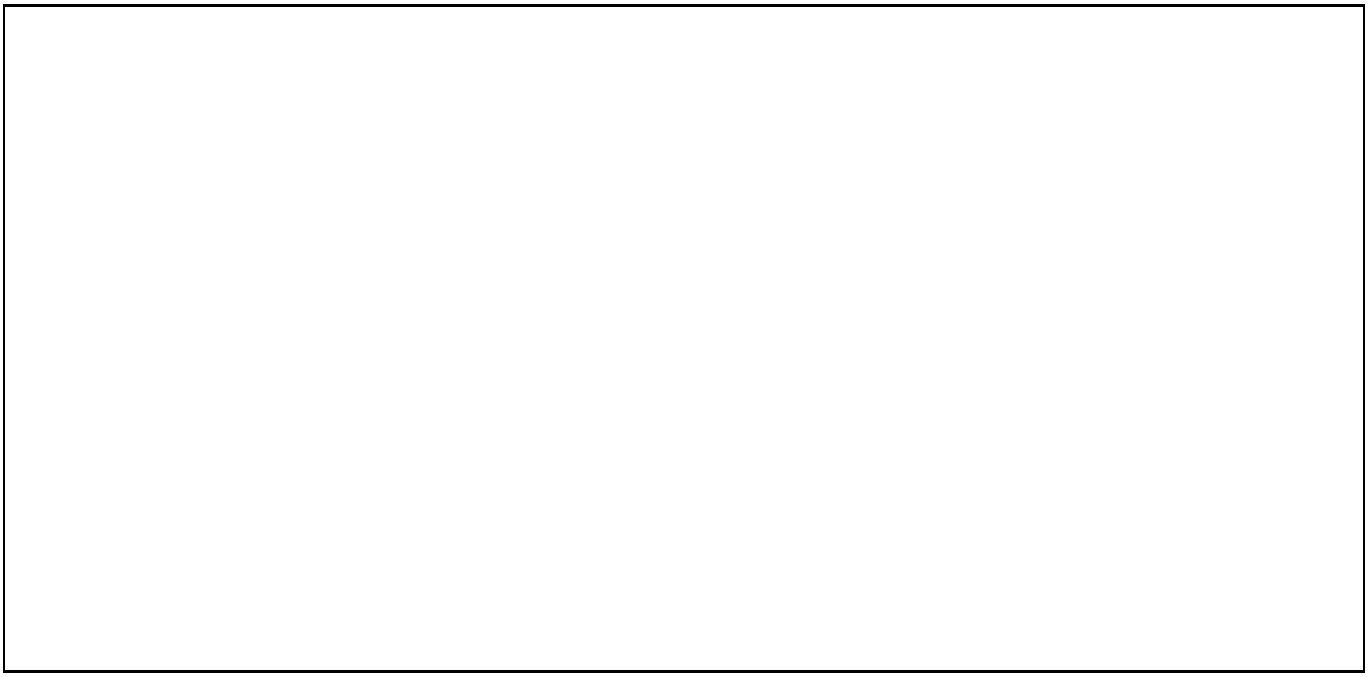

Fig. 15. Same as Fig. 13, except that the extinction model by Arenou et al. (1992) is used (solid line, Run 9). For comparison, we show the results from Run 3 as a dashed line.

with the particular GSC plate in Region 6, rather than to a deficiency of the model. It is possible that due to the very high degree of crowding toward this line of sight, only a subset of all images were included in the GSC in order to maintain a good magnitude coverage (one of the GSC requirements was to provide a uniform stellar density over the sky, rather than a uniform magnitude limit, so that at lower Galactic latitudes the GSC becomes incomplete at brighter magnitudes than for higher Galactic latitudes (Jenkner et al. 1990). An investigation of this particular plate is currently being carried out to determine the actual nature of the discrepancy seen in Figs. 13 – 15.

3.3. Starcounts and Galactic Structure

From Eqs. (4),(7), and (13) it is clear that the value of $Z_\odot$ will have an impact on the predicted reddening. Indeed, this parameter will have an important effect, even if there is no reddeding, as it controls the viewing aspect when looking at the Galactic plane at positions slightly above or below it. Therefore, its effect is twofold: it changes the predicted value of $E(B-V)$, but it also changes the density contribution of the different types of stars that make up the starcounts model. Table 5 indicates the predicted reddening for a model with the same parameters as that for Run 3 in Table 4, but for values of $Z_\odot = +40$ pc and $Z_\odot = -10$ pc (instead of the standard value $Z_\odot = +7$ pc adopted in Runs 1 to 9 of Table 4). Figure 16 show the effects on the predicted starcounts. From the last column on Table 5 it is evident that we obtain a more precise fit for a value of $Z_\odot = +40$ pc, while a value of $Z_\odot = -10$ pc is clearly inadequate. The latter value has been recently suggested by Binney et al. (1996) who have found, from a dust-corrected near-infrared COBE/DIRBE surface brightness map of the inner Galaxy ($|l| \leq 30^\circ$, $|b| \leq 15^\circ$), that the Sun should lie 14 ± 4 pc *below* their (photometric-model) symmetry plane. This solution seems incompatible with the GSC low-latitude optical starcounts presented here. Indeed, starcount studies at the Galactic poles indicate that the Sun is *above* the Galactic plane (as defined by the distribution of neutral Hydrogen), e.g., Humphreys & Larsen (1995) find $Z_\odot = 20.5 \pm 3.5$ pc from a comparison of the asymmetry in the starcounts towards the North and South Galactic poles.

We have also varied the adopted value of $R_\odot = 8.5$ kpc within a wide margin, between 7 kpc and 10 kpc. The effect of these self-similar Galaxy models on the starcounts is minimal, as it can be seen in Table 5, with no salient features in the shape of the predicted starcounts. This is a consequence of the relatively small distance range covered by these bright starcounts, limited typically to Heliocentric distances smaller than about 2 kpc.

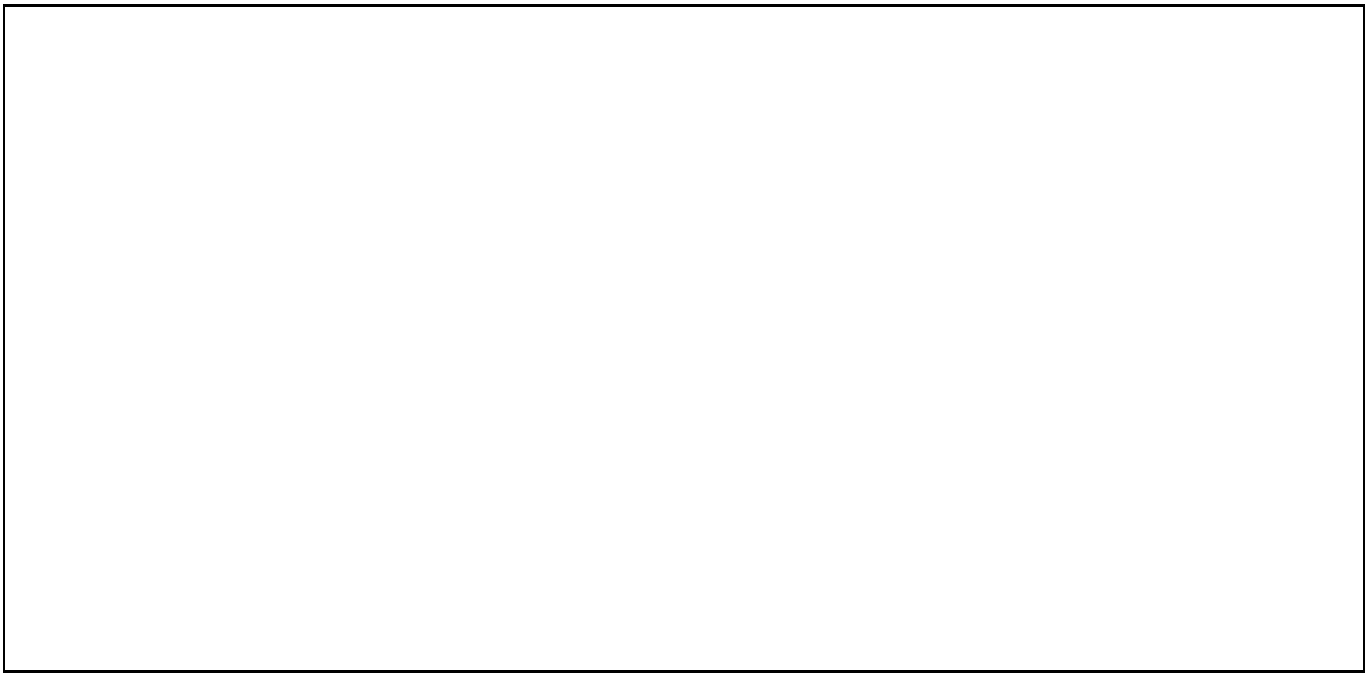

Fig. 16. Same as Fig. 13, except that we have used $Z_\odot = +7$ pc (solid line, Run 3) $Z_\odot = +40$ pc (dashed line, Run 10), and $Z_\odot = -10$ pc (dot-dashed line, Run 11).

The structural parameters discussed previously affect *all* the stellar populations simultaneously. However, there are still a few population-dependent parameters in the starcount model that have an impact on the starcounts: these are the population scale-heights and scale-lengths.

Figure 17 shows the effect of varying the exponential scale-length for the disk ($H_{\rm Disk}$) between 2.5 kpc and 4.5 kpc. The effect on the counts is highly dependent on projection effects, and thus Regions 1 and 6 are the most affected by changes in this parameter, along with Region 3 at the fainter magnitudes, all these Regions being close to the center-anticenter direction. A *longer* $H_{\rm Disk}$ of about 3.5 to 4.5 kpc seems to reproduce better the counts, rather than the short-scale of 2.3 ± 0.1 kpc advocated recently by Ruphy et al. (1996) from star and color counts from the DENIS project. Since all these determinations *are* model-dependent, it is possible that other Galactic parameters have come into play in the determination by Ruphy et al., since their fields were located at $l = 217^\circ$ and $l = 239^\circ$, close to our Regions 4 and 5 were we see (Fig. 17) a reduced dependency of the predicted counts on $H_{\rm Disk}$. This highlights the importance of studying *several* directions simultaneously to best constrain the structural properties of the Galaxy from the vast parameter space available in the models. On the other hand, our results agree with the determination by Ng et al. (1995), who obtained a value of $H_{\rm Disk}$ in the range 3.5 – 4.5 kpc from an analysis of starcounts towards the Galactic Bulge (see Sect. 3.4).

The scale-height for disk stars ($h_{\rm Disk}$) is parametrized as a function of absolute visual magnitude, as described by Méndez & van Altena (1996). Red-giant & sub-giant stars (defined as $M_v \leq +3.0$ and $(B-V)_o > +0.57$) are given a single $h_{\rm Disk}$ of 250 pc. We have varied this parameter between 150 and 350 pc and found that the effect of these changes on the predicted counts to be minimal, except for Region 3. Region 3, with a higher Galactic latitude, is more sensitive to this parameter as the line-of-sight includes a wider sampling of stars in the direction perpendicular to the plane. In fact, this effect has been used by Méndez & van Altena to constrain $h_{\rm Disk}$ for disk sub-giants, obtaining a value of 250 ± 32 pc, in agreement with previous determinations of the scale-height for red-giants.

As for the scale-height of main-sequence stars, we have changed this parameter between a "lower" and an "upper" set of values allowed by the observational uncertainties, as described by Méndez & van Altena (1996). Given the distance range predicted from the model, the luminosity range sampled by these counts encompass the range $-1.0 \leq M_v < +0.5$, i.e., it includes main-sequence stars of spectral type B5 to A0 and red-giants (luminosity class III) of spectral types G0 to late M, located at distances of between 400 pc and 1.8 kpc. We find that the effect of changing the scale-height of main-sequence stars yields a systematic change in the counts, and therefore it does not produce a good match to the overall counts. This can be clearly seen by inspection of the last two columns on Table 5 for Runs 18 and 19.

Table 5. Predicted starcounts as a function of Galactic Structure parameters in the starcounts model.

Run	Reg. 1	Reg. 2	Reg. 3	Reg. 4	Reg. 5	Reg. 6	$< \frac{\Delta N}{N_{\rm Obs}} >^{\rm a,b}$	$< \frac{\lvert\Delta N\rvert}{N_{\rm Obs}} >^{\rm b}$	Comments[c]
Obs.	1 072	1 771	3 449	2 392	3 023	1 020	–	–	Measured value
3	1 296	1 977	2 489	2 780	2 510	2 888	0.01 ± 0.22	0.19 ± 0.06	$R_{\rm V}$ as in Eq. (17)
10	1 081	1 639	2 113	2 232	2 951	2 171	-0.11 ± 0.16	0.11 ± 0.16	$Z_\odot = +40$ pc
11	1 245	2 005	2 695	3 125	2 265	3 116	0.03 ± 0.25	0.21 ± 0.07	$Z_\odot = -10$ pc
12	1 275	1 961	2 489	2 756	2 497	2 846	0.00 ± 0.21	0.18 ± 0.06	$R_\odot = 7$ kpc
13	1 293	1 991	2 491	2 797	2 521	2 487	0.01 ± 0.22	0.19 ± 0.06	$R_\odot = 10$ kpc
14	1 470	2 050	2 229	2 830	2 560	3 540	0.04 ± 0.29	0.24 ± 0.11	$H_{\rm Disk} = 2.5$ kpc
15	1 201	1 940	2 655	2 753	2 484	2 559	-0.01 ± 0.18	0.16 ± 0.05	$H_{\rm Disk} = 4.5$ kpc
16	1 274	1 951	2 106	2 590	2 329	2 806	-0.05 ± 0.25	0.20 ± 0.12	$h_{\rm Disk}$ for RG & SG[d] of 150 pc
17	1 292	1 991	2 725	2 874	2 602	2 865	0.04 ± 0.20	0.18 ± 0.05	$h_{\rm Disk}$ for RG & SG of 350 pc
18	1 184	1 838	2 035	2 348	2 139	2 517	-0.12 ± 0.22	0.17 ± 0.17	Lower $h_{\rm Disk}$ for MS[e] stars
19	1 328	2 032	2 757	2 990	2 698	2 986	0.07 ± 0.21	0.19 ± 0.06	Upper $h_{\rm Disk}$ for MS stars
20	1 035	1 719	2 557	2 389	2 751	2 009	-0.08 ± 0.10	0.08 ± 0.10	Best-fit solution[f]

[a] ΔN is in the sense $N_{\rm Model} - N_{\rm Obs}$.
[b] These columns exclude Region 6, see text for explanation.
[c] The meaning of the different runs is discussed in the text. Here we give only a brief description.
[d] RG stands for red-giants, SG for sub-giants.
[e] MS stands for main-sequence.
[f] From Regions 1, 2, and 4 only, with $Z_\odot = +27$ pc and $H_{\rm Disk} = 6$ kpc, see text.

Fig. 17. Same as Fig. 13, except that we have used a scale-length for the disk of 3.5 kpc (solid line, Run 3), 2.5 kpc (dashed line, Run 14), and 4.5 kpc (dot-dashed line, Run 15).

3.4. Putting it all together

The purpose of the parameter-space exploration described in the previous two sub-sections has been to indicate the possible range of uncertainty expected from the model starcounts given our present knowledge of the different Galactic structure and reddening-related parameters employed in the model. It is clear from the analysis presented above that, in principle, several combinations of parameters can yield similar predicted starcounts and, for this reason, we have not attempted, at this stage, a global solution. However, the numerous trends described above do yield some constraints on parameters of the reddening model as well as parameters of the Galactic model, and we describe these in turn.

From the reddening model, we find that the adopted value of the scale-height of the reddening material has an important role in the predicted counts. On the other hand, these bright starcounts are not very sensitive to the adopted value of the differential reddening beyond the last node point, for the reasons explained in Sect. 3.2.

A change of the adopted Galactocentric distance within considerable limits does not have an impact on the model counts, for reasons that have been explained in Sect. 3.3. Also, the effect of scale-heights is either minimal, or yields a systematic trend regardless of the region being modeled, and therefore a change in this parameter is not warranted by the present analysis (see below though). We therefore infer that the current model implementation is not inconsistent with the observed counts.

The distance of the Sun from the Galactic plane, and the scale-length of disk stars have, both, a large impact on the predicted counts. The question is whether a better *representation* of the observed counts is provided by a suitable choice of $Z_\odot$ and $H_{\rm Disk}$, or by a large scale-height of the reddening material. We explore this by assuming $h_{\rm red} = 110$ pc and by solving, simultaneously, for $Z_\odot$ and $H_{\rm Disk}$. This simultaneous solution is only possible because, as it can be seen from Figs. 16 and 17, Regions 2, 4, and 5 are mostly sensitive to $Z_\odot$ (but not to $H_{\rm Disk}$), while Regions 1 and 3 are sensitive to both. We use an iterative procedure in which we solve for $Z_\odot$ from Regions 2, and 4, apply this solution to Region 1 from which we determine $H_{\rm Disk}$, which is used in turn to compute counts in Regions 2, and 4, and so on until convergence. At each iteration, the relevant parameters are computed from a full χ^2 analysis of the observed and computed starcounts in the magnitude range $8 \leq V < V_{\rm lim}$. Region 5 was excluded when computing $Z_\odot$ because it was found to give a somewhat discrepant value for this parameter with respect to the other two regions, as well as a larger error. For example, from Runs 3 and 10 we get $Z_\odot = 24 \pm 11\,(3\sigma)$ pc from Region 2, $Z_\odot = 30 \pm 8\,(3\sigma)$ pc from Region 4, and $Z_\odot = 44 \pm 19\,(3\sigma)$ pc from Region 5. Indeed, the mean from Regions 2 and 4 is not incompatible (at the the 3σ level) with the results from Region 5, given its larger uncertainty. As for the disk's scale-height, we could not use Region 3 because it never converged. Indeed, as it can be seen from Figs. 16 and 17, whatever combination of $Z_\odot$ and $H_{\rm Disk}$ underestimates the counts, and this is true even for the run using Arenou's et al. (1992) model, as can be seen from Fig. 15.

The resulting parameters are $Z_\odot = 27 \pm 3$ pc and $H_{\rm Disk} = 6.0 \pm 2.0$ kpc, where the uncertainties are at the 99% confidence interval (or, equivalently, 3σ), and have been computed from the χ^2 fits using the parameter estimation scheme described by Lampton et al. (1976). It must be emphasized that these results were computed using only Regions 1, 2, and 4, for the reasons explained above.

With the above determined values for $Z_\odot$ and $H_{\rm Disk}$, the predicted counts indicate an overall uncertainty for *all* regions (excluding, as always, Region 6, but including Regions 3 and 5 which were not used in the fit) of only 8% in the counts (see Table 5). This run is illustrated in Fig. 18. When comparing this run with Run 8 (Table 4) we see that we have indeed reduced the scatter from about 15% to half this value with this choice of values for $Z_\odot$ and $H_{\rm Disk}$.

Our long scale-height is compatible with the results by van der Kruit (1986), who obtained $H_{\rm Disk} = 5.5 \pm 1.0$ kpc from his analysis of the *Pioneer 10* optical integrated starlight measurements. Ruphy et al. (1996), have suggested that van der Kruit's result is sensitive to the adopted scale-height for disk stars. However, if we adopt our lower set for the scale-height of disk stars, then the Solar height above the plane is affected quite considerably, but the scale-length remains unchanged. In fact, in this case, we derive $Z_\odot = 8.2 \pm 1.0$ pc and $H_{\rm Disk} = 6.5 \pm 1.8$ kpc, in disagreement with Ruphy's et al. claim that a smaller scale-height will substantially reduce the derived scale-length. We must emphasize that Ruphy's et al. IR counts, van der Kruit's optical integrated light measurements, and our GSC counts are all mostly sensitive to G and K giants, so that we are sampling basically the *same* population of disk objects.

It is evident that more constraints on the models and a better insight on stellar populations *in the disk* would be obtained if we had colors. Unfortunately, the availability of colors from the digitization of the short-exposure red plates obtained with the UK-Schmidt at low-Galactic latitudes is not foreseen in any of the current major digitization efforts (van Altena et al. 1993). This situation is particularly unfortunate because of the need for an optical counterpart to the near-infrared surveys of the Galactic plane such as DENIS (Epchtein 1994), 2MASS (Skrutskie et al. 1995), and the Two Micron Galactic Survey (Garzon et al. 1994).

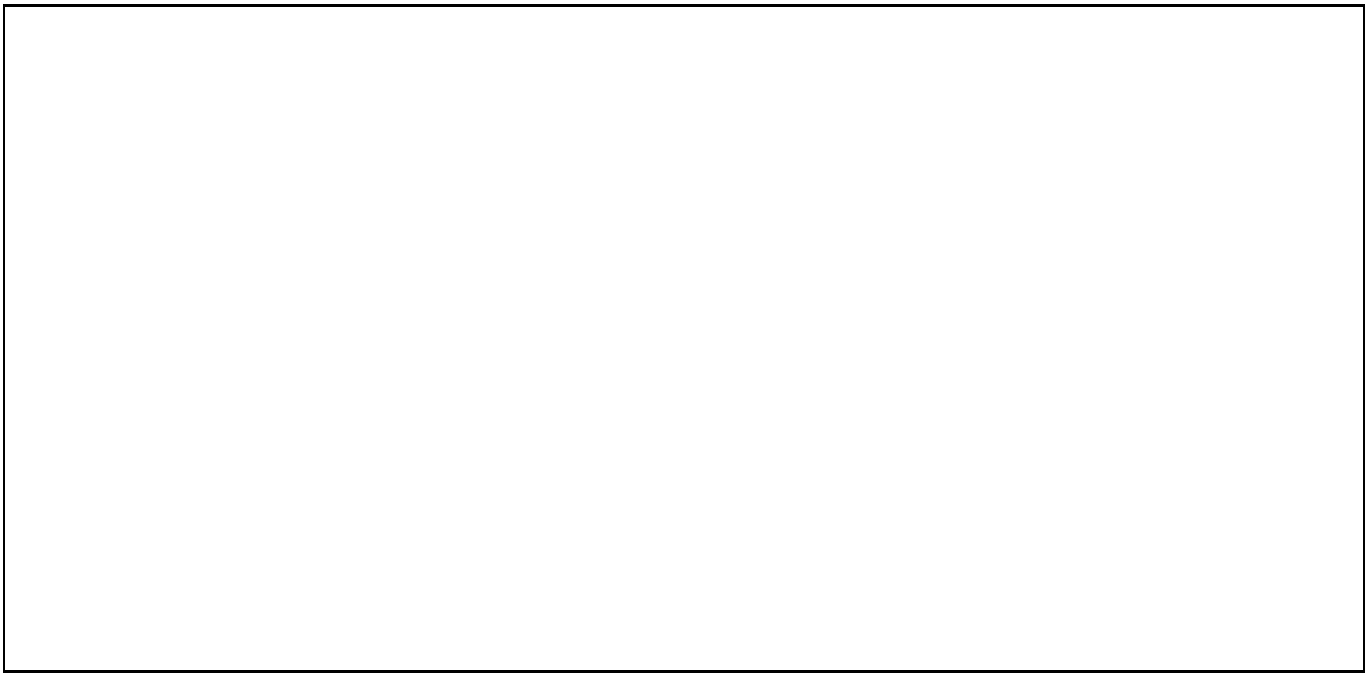

Fig. 18. Same as Fig. 13, except that we have used our best-fit solution with $Z_{\odot} = +27$ pc and $H_{\rm Disk} = 6$ kpc (solid line). For comparison we also indicate Run 8 as a dashed line.

4. Conclusions

We have presented the first systematic study of low-Galactic latitude starcounts from the perspective of a Galactic structure and reddening model, and we have demonstrated that our reddening model can be used to obtain meaningful starcount estimates in the plane of the Milky-Way. We find that it is possible to predict starcounts in the range $8.0 \leq V < 13.7$ with a mean accuracy of 15% or better for total samples of several thousand stars at $|b| < 10^{\circ}$, and for total reddening at 1 kpc of up to $E(B-V) \sim 0.7$ mag. This accuracy is similar to the accuracy with which starcounts at high galactic latitudes can be modeled due to fluctuations in the stellar density along the line-of-sight (Bahcall 1986). This opens the possibility of using our reddening and starcount model to estimate and compare observations of diffuse starlight to constrain the major structural parameters of the Galaxy, as described by van der Kruit (1986, 1990). This is also an important step in determining the contribution of diffuse Galactic light to the extragalactic diffuse light component whose distribution is important as a test of Cosmological models (Paresce 1985), for theories of galaxy formation and evolution (Cole et al. 1992, Sasseen et al. 1995, Vaeisaenen 1996), and for theories of growth of structure in the Universe (Bowyer & Leinert 1990). In a subsequent paper we will explore this issue in detail.

Another important application in the works is the use of our model to compute the distance distribution of stars self-consistently with the starcounts, in order to derive corrections to absolute parallax (van Altena 1974, 1986, van Altena et al. 1988) which might in turn yield better parallaxes than those contained in the latest edition of the Yale Parallax Catalogue (van Altena et al. 1995).

By performing a simultaneous fit to three selected regions, we derive a distance of the Sun from the symmetry plane of the Galaxy of $27 \pm 3\,(3\sigma)$ pc, while the disk's scale-length is found to be $6 \pm 2\,(3\sigma)$ kpc. The derived value for $Z_{\odot}$ is sensitive to the adopted scale-height of disk stars, but no big dependency of $H_{\rm Disk}$ on this parameter is found. These values should be taken, of course, with caution because of the inherent uncertainties in modeling optical starcounts in the presence of patchy reddening material, which introduce the uncertainties explored in this paper.

We have only grasped the rich potential for Galactic structure studies that could be carried out with the digitized supplemental survey plate collection of the GSC. It is clear from the analysis presented in this paper that the problem is, by nature, multi-variate, and that a number of parameters must be adjusted to a set of observables simultaneously. The model evaluations described above are computationally very intensive, and we are working on ways to make the problem more tractable so that more regions can be compared to the model predictions at once. A related issue is, of course, the choice of optimum algorithms to arrive at the best overall solution. We are confident that this is doable,

since important advances have been made in these two areas recently, as shown by Larsen (1996), Larsen et al. (1996), and Chen (1996, 1997).

The reddening model source code (written in f77) may be obtained upon request from the authors.

Acknowledgements. The four data files and the source code to compute the total reddening from the Burstein & Heiles (1982) maps at any requested point in the sky were kindly made available to us by Dr. David Burstein. The authors would like to acknowledge a number of constructive comments from the referee, Dr. Helge Jønch-Sørensen, which lead to the introduction of the more self-consistent Model-B for reddening extrapolation, and several other suggestions from the referee which have made the paper more readable overall. R.A.M. has greatly benefited from conversations with Dr. Fernando Comeron. R.A.M. acknowledges a grant from Allied Signal Aerospace Guidance and Control Systems for the development of the reddening model in the context of the Hubble Space Telescope Fixed-Head Star Trackers and, in particular, to Arthur J. Bradley for his interest and constant support during this research. R.A.M. also acknowledges a travel grant (C-51073) from the Chilean Andes Foundation. W.F.v.A. acknowledges support from NSF, NASA and the US Naval Observatory, Flagstaff Station, the later for supporting the development of the initial low-latitude reddening model in 1987 and 1988. The Guide Star Catalog was produced at the Space Telescope Science Institute under U.S. Government grant. These data are based on photographic data obtained using the Oschin Schmidt Telescope on Palomar Mountain and the UK Schmidt Telescope. The Oschin Schmidt Telescope is operated by the California Institute of Technology and Palomar Observatory. The UK Schmidt Telescope was operated by the Royal Observatory Edinburgh, with funding from the UK Science and Engineering Research Council (later the UK Particle Physics and Astronomy Research Council), until 1988 June, and thereafter by the Anglo-Australian Observatory. The blue plates of the southern Sky Atlas and its Equatorial Extension (together known as the SERC-J), as well as the Equatorial Red (ER) were all taken with the UK Schmidt.

References

Allen C.W. 1954, MNRAS 114, 387
Arenou F., Grenon M., Gomez A. 1992, A&A 258, 104
Bahcall J.N. 1986, ARA&A 24, 557
Bernacca P.L., Bucciarelli B., Lattanzi M.G., et al. 1992, in: Complementary Approaches to Double and Multiple Star Research, IAU Coll. No. 135, McAlister H.A., Hartkopf, W.I. (eds.). Astronomical Society of the Pacific, San Francisco, p. 449
Binney J., Gerhard O., Spergel D. 1996, astro-ph/9609066
Blackwell D.E., Petford A.D., Arribas S., Haddock, D.J., Selby, M.J. 1990, A&A 232, 396
Bowyer S., Leinert C. 1990, in: The Galactic and Extragalactic Background Radiation, IAU Symp. No. 139, Bowyer S., Leinert C. (eds.). Kluwer, Dordrecht, p. 522
Burstein D., Heiles C. 1978, ApJ 225, 40
Burstein D., Heiles C. 1982, AJ 87, 1165
Cannon R.D. 1984, in: Astronomy with Schmidt-Type Telescopes, Capaccioli M. (ed.). Reidel, Dordrecht, p.25
Chen B. 1996, A&A 306, 733
Chen B. 1997, AJ 113, 311
Cole S., Treyer M.-A., Silk J. 1992, ApJ 385, 9
Crawford D.L. 1975, PASP 87, 481
Dame T.M., Thaddeus P. 1985, ApJ 297, 751
Dame T.M., Ungerechts H., Cohen R.S., et al. 1987, ApJ 322, 706
Deutschman W.A., Davis R.J., Schild R.E. 1976, ApJS 30, 97
de Vaucoleurs G., Buta R. 1983, AJ 88, 939
de Vaucoleurs G., de Vaucoleurs A., Corwin H.G. 1976, Second Reference Catalogue of Bright Galaxies. University of Texas, Austin
Di Benedetto G.P., Rabbia Y. 1987, A&A 188, 114
Dufay J. 1954, Nébuleuses Galactiques et Matière Interstellaire. Albin Michel, Paris
Epchtein N. 1994, Ap&SS 217, 3
Fernie J.D. 1968 AJ 73, 995
FitzGerald M.P. 1968 AJ 73, 983
FitzGerald M.P. 1974, A&A 31, 467
FitzGerald M.P. 1987, MNRAS 229, 227
FitzGerald M.P., Reed B.C. 1991, in: Objective-Prism and Other Surveys, Davis Philip A.G., Upgren A.R. (eds.). L. Davis Press, Schenectady, p. 45
Forbes D. 1985, AJ 90, 301
Fouqué P., Gieren W.P. 1997, A&A 320, 799
Garzon F., Hammersley P.L., Mahoney T., Calbet X., Selby M.J. 1994, Ap&SS 217, 177
Gutiérrez-Moreno A., Moreno H. 1975, PASP 87, 425
Heiles C. 1976, ApJ 204, 379

Humphreys R.M. 1993, in: Workshop on Databases for Galactic Structure, Davis Philip A.G., Hauck B., Upgren A.R. (eds.). L. Davis Press, Schenectady p. 87
Humphreys R.M., Larsen J.A. 1995, AJ 110, 2183
Jenkner H., Lasker B.M., Sturch C.R., et al. 1990, AJ 99, 2082
Johnson H.L., Morgan W.W. 1953, ApJ 117, 313
Jønch-Sørensen H. 1994, A&A 292, 92
Jønch-Sørensen H., Knude J. 1994, A&A 288, 139
Knude J. 1979, A&A 71, 344
Knude J. 1996, A&A 306, 108
Lampton M., Margon B., Bowyer S. 1976, ApJ 208, 177
Larsen J.A. 1996, PhD Thesis, University of Minnesota
Larsen J.A., Berendse F., Humphreys R.M. 1996, BAAS 188, #08.02
Lasker B.M., Sturch C.R., McLean B.J., et al. 1990, AJ 99, 2019
Layden A.C., Hanson R.B., Hawley S.L., Klemola A.R., Hanley C.J. 1996, AJ 112, 2110
Lu N.Y., Houck J.R., Salpeter E.E. 1992, AJ 104, 1505
LyngåG. 1979, in: The Large-Scale Characteristics of the Galaxy, IAU Symp. No. 84, Burton W.B. (ed.). Reidel, Dordrecht, p. 87
LyngåG. 1982, A&A 109, 213
Maddalena R., Thaddeus P. 1985, ApJ 294, 231
Mattila K. 1980a, A&AS 39, 53
Mattila K. 1980b, A&A 82, 373
McClure R.D., Crawford D. 1971, AJ 76, 31
Méndez R.A. 1995, Ph.D. Thesis, Yale University
Méndez R.A., van Altena W.F. 1996, A.J. 112, 655
Méndez R.A., Minniti D., De Marchi G., Baker A., Couch W. J. 1996, MNRAS 283, 666
Meyer S.L. 1975, Data Analysis for Scientists and Engineers. Wiley, New York
Mihalas D., Binney J. 1981, Galactic Astronomy. Freeman, San Francisco
Minkowski R.L., Abell G.O. 1963, in: Stars and Stellar Systems, Vol. III, Strand Aa. (ed.). University of Chicago Press, Chicago, p. 481
Monet D.G. 1988, ARA&A 26, 413
Neckel Th., Klare G. 1980, A&AS 42, 251 (NK)
Ng Y., Bertelli G., Bressan A., Chiosi C.M, Lub J. 1995, A&A 295, 655
Ochsenbein F. 1983, A&A 118, 197
Pandey A.K., Mahra H.S. 1987, MNRAS 226, 635
Parenago P.P. 1945, Russian AJ 22, 129
Paresce F. 1985 Nuovo Cimento C Vol. 8C, 379
Ratnatunga K.U. 1990, AJ 100, 280
Reid N., Majewski S.R. 1993, ApJ 409, 635
Reid I.N., Brewer C., Brucato R.J., et al. 1991, PASP 103, 661
Ruphy S., Robin A.C., Epchtein N., et al. 1996, A&A 313, L21
Russell J.L., Lasker B.M., McLean B.J., Sturch C.R., Jenkner H. 1990, AJ 99, 2059
Sandage A. 1972, ApJ 178, 1
Sasseen T., Lampton M., Bowyer S., Wu X. 1995, ApJ 447, 630
Savage B.D., Mathis J.S. 1979, ARA&A 17, 73
Scheffler H. 1982, in: Landolt-Börnstein, Numerical Data and Functional Relationships in Science and Technology, Vol. 2c, Schaifers K., Voigt H.H. (eds.). Springer-Verlag, Berlin, p. 45
Scheffler H., Elsässer H. 1987, Physics of the Galaxy and Interstellar Matter. Springer-Verlag, Berlin
Schmidt-Kaler Th. 1982, in: Landolt-Börnstein, Numerical Data and Functional Relationships in Science and Technology, Vol. 2c, Schaifers K., Voigt H.H. (eds.). Springer-Verlag, Berlin, p. 1
Skrutskie M.F., Beichman C., Capps R., et al. 1995, BAAS 187, #75.07
Solomon P.M., Sanders D.B., Scoville N.Z. 1979, in: The Large-Scale Characteristics of the Galaxy, IAU Symp. No. 84, Burton W.B. (ed.). Reidel, Dordrecht, p. 35
Spitzer L. 1978, Physical Processes in the Interstellar Medium. Wiley, New York
Toller G.N. 1990, in: The Galactic and Extragalactic Background Radiation, IAU Symp. No. 139, Bowyer S., Leinert C. (eds.). Kluwer, Dordrecht, p. 21
Vaeisaenen P. 1996, A&A 315,21
van Altena W.F. 1974, AJ 79, 826
van Altena W.F. 1986, in: Astrometric Techniques, IAU Symp. No. 109, Eichhorn H., Leacock, R.J. (eds.). Reidel, Dordrecht, p. 183
van Altena W.F., Lee J.T., Hanson R.B., Lutz T.E. 1988, in: Calibration of Stellar Ages, Philip A.G.D. (ed.). L. Davis Press, Schenectady, p. 175

van Altena W.F., Platais I., Cudworth K.M., et al. 1993, in: Workshop on Databases for Galactic Structure, Davis Philip A.G., Hauck B., Upgren A.R. (eds.). L. Davis Press, Schenectady p. 215
van Altena W.F., Lee J.T., Hoffleit E.D. 1995, The General Catalogue of Trigonometric Stellar Parallaxes. L. Davis Press, Schenectady
van der Kruit P.C. 1986, A&A 157, 230
van der Kruit P.C. 1990, in: The Galactic and Extragalactic Background Radiation, IAU Symp. No. 139, Bowyer S., Leinert C. (eds.). Kluwer, Dordrecht, p. 85
van Herk G. 1965, Bull. Astron. Inst. Netherlands 18, 71
Williams J.P. 1995, Ph.D. Thesis, University of California at Berkeley
Williams J.P., Blitz L., Stark A.A. 1995, ApJ 451, 252

This article was processed by the author using Springer-Verlag LaTeX A&A style file *L-AA* version 3.

E(B−V) at infinity [mag]
0
0.1
0.2
0.3
0.4
0
20
40
60
80
Galactic latitude [deg]

U kpc
5
0
−5
V kpc
5
0
−5

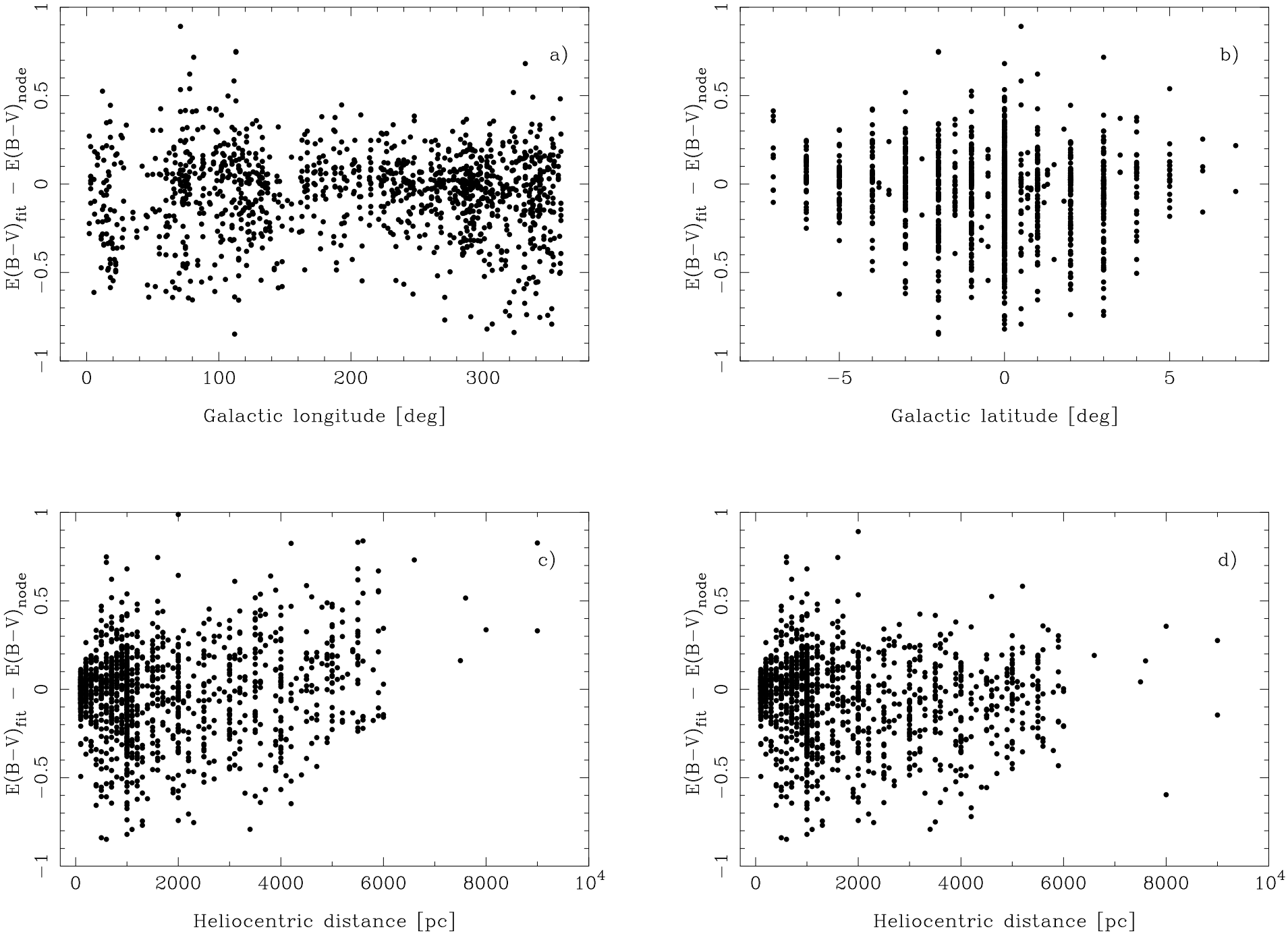
a)
b)
c)
d)
E(B−V)fit − E(B−V)node
Galactic longitude [deg]
Galactic latitude [deg]
Heliocentric distance [pc]
−1
−0.5
0
0.5
1
0
100
200
300
−5
5
2000
4000
6000
8000
10^4

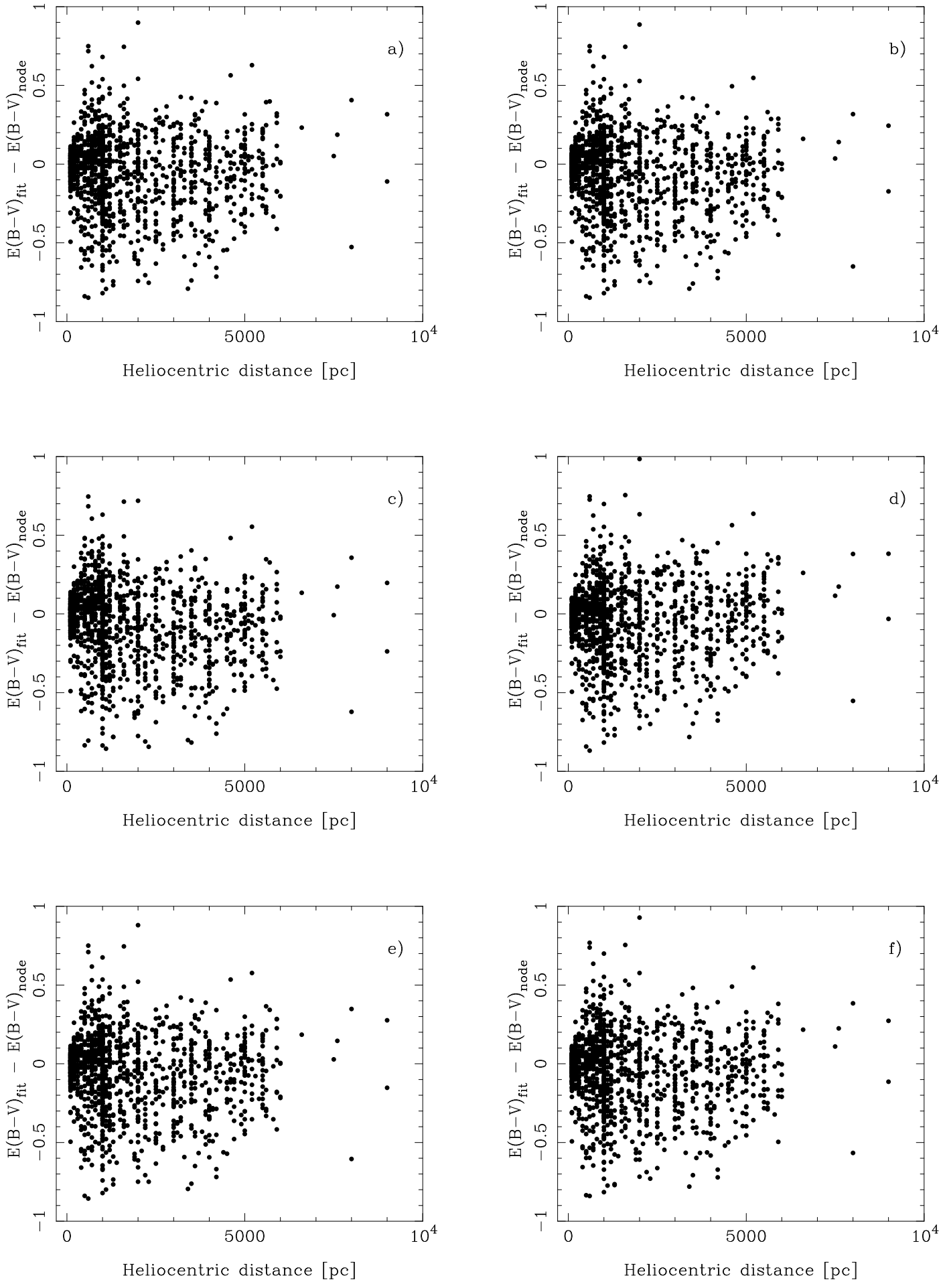
a)
b)
c)
d)
e)
f)
$E(B-V)_{fit} - E(B-V)_{node}$
Heliocentric distance [pc]
−1
−0.5
0
0.5
1
0
5000
10^4

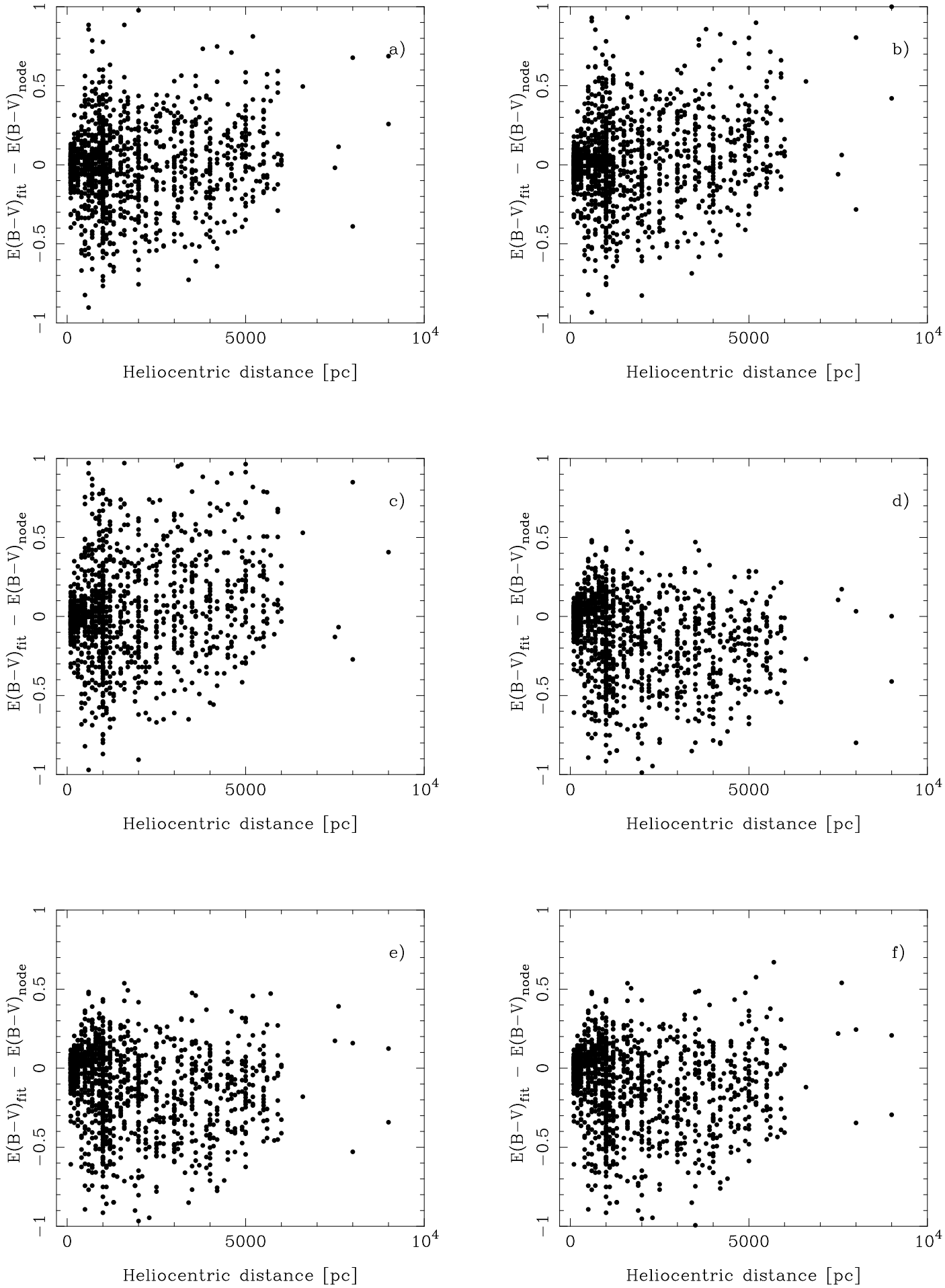
a)
b)
c)
d)
e)
f)
E(B−V)fit − E(B−V)node
Heliocentric distance [pc]
−1
−0.5
0
0.5
1
0
5000
10^4

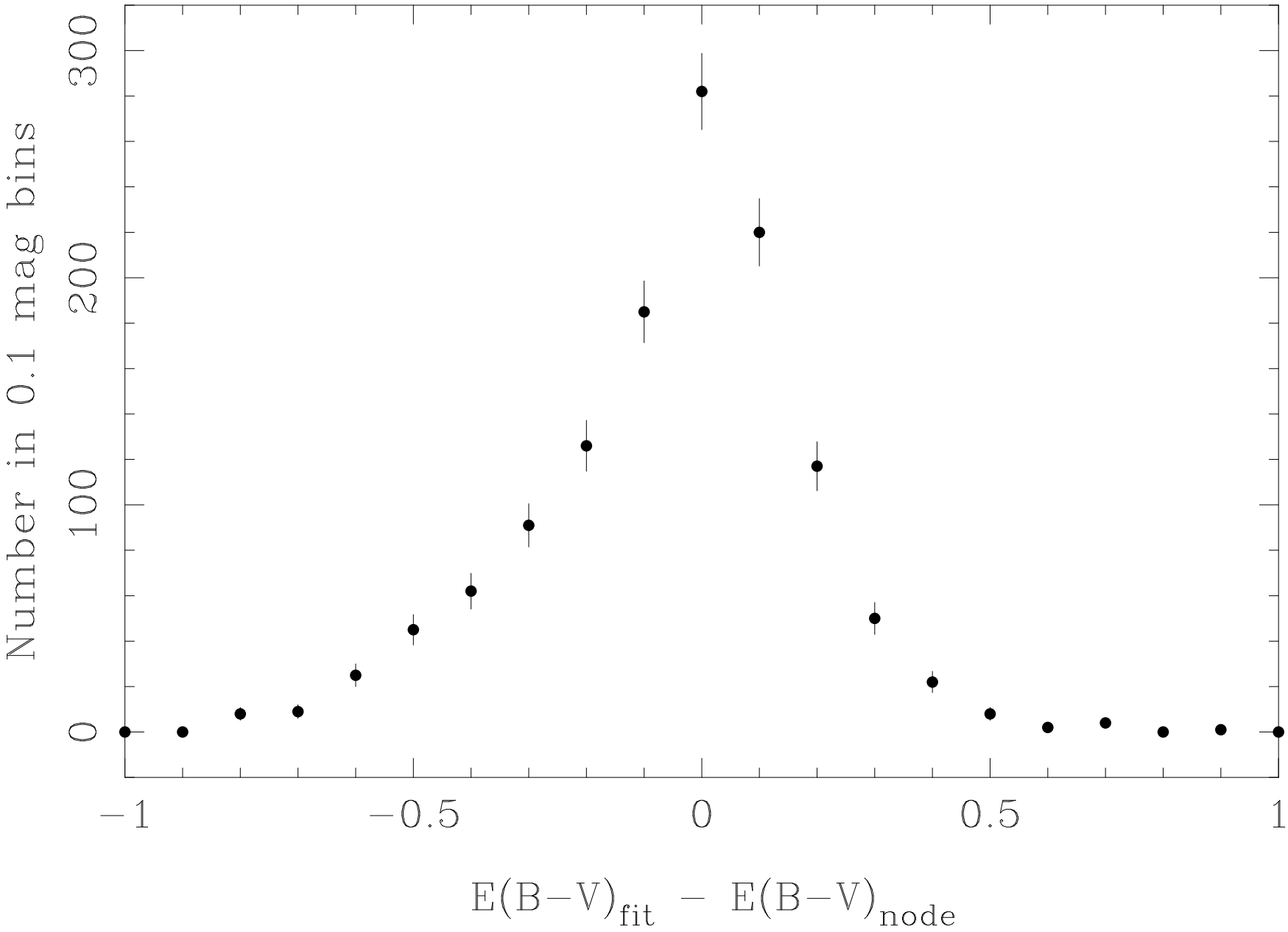
Number in 0.1 mag bins
0
100
200
300
−1
−0.5
0
0.5
1
E(B−V)fit − E(B−V)node

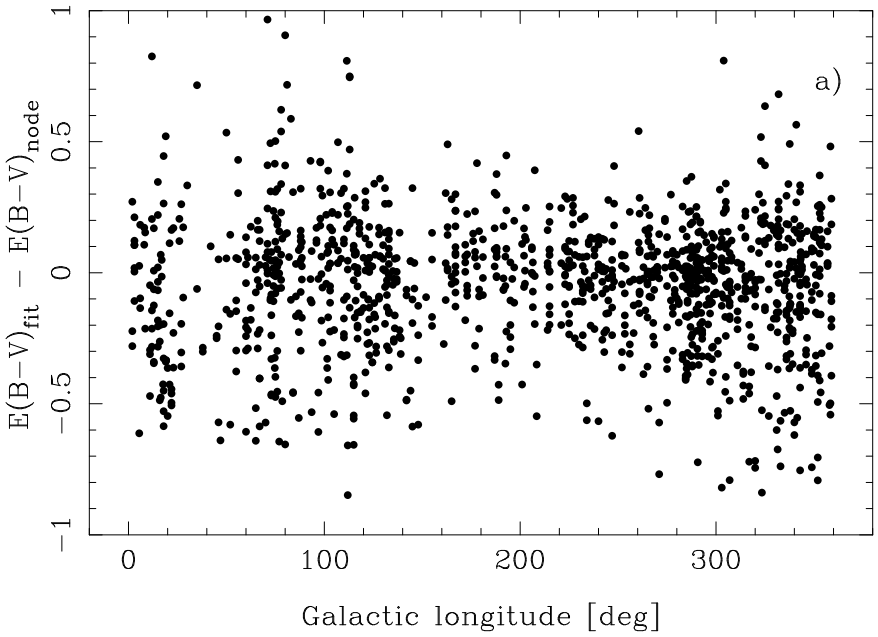
a)
$E(B-V)_{fit} - E(B-V)_{node}$
Galactic longitude [deg]
0
100
200
300
−1
−0.5
0
0.5
1

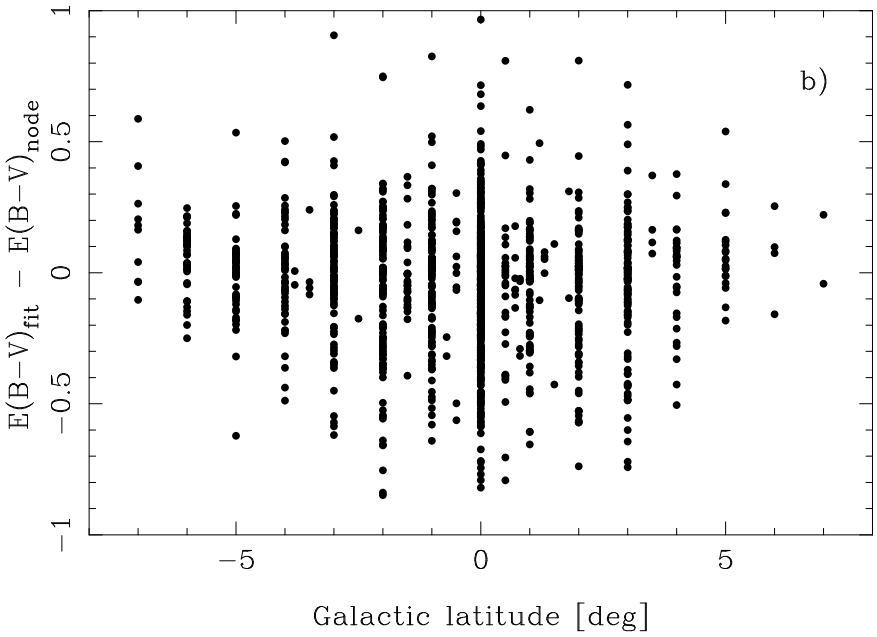
b)
$E(B-V)_{fit} - E(B-V)_{node}$
Galactic latitude [deg]
−5
0
5
−1
−0.5
0
0.5
1

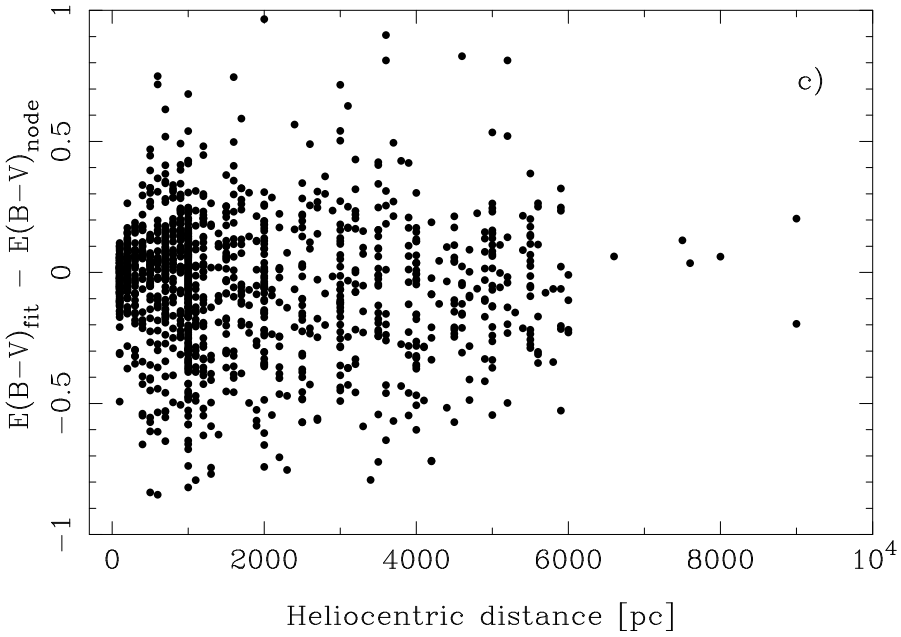
c)
$E(B-V)_{fit} - E(B-V)_{node}$
Heliocentric distance [pc]
0
2000
4000
6000
8000
10^4
−1
−0.5
0
0.5
1

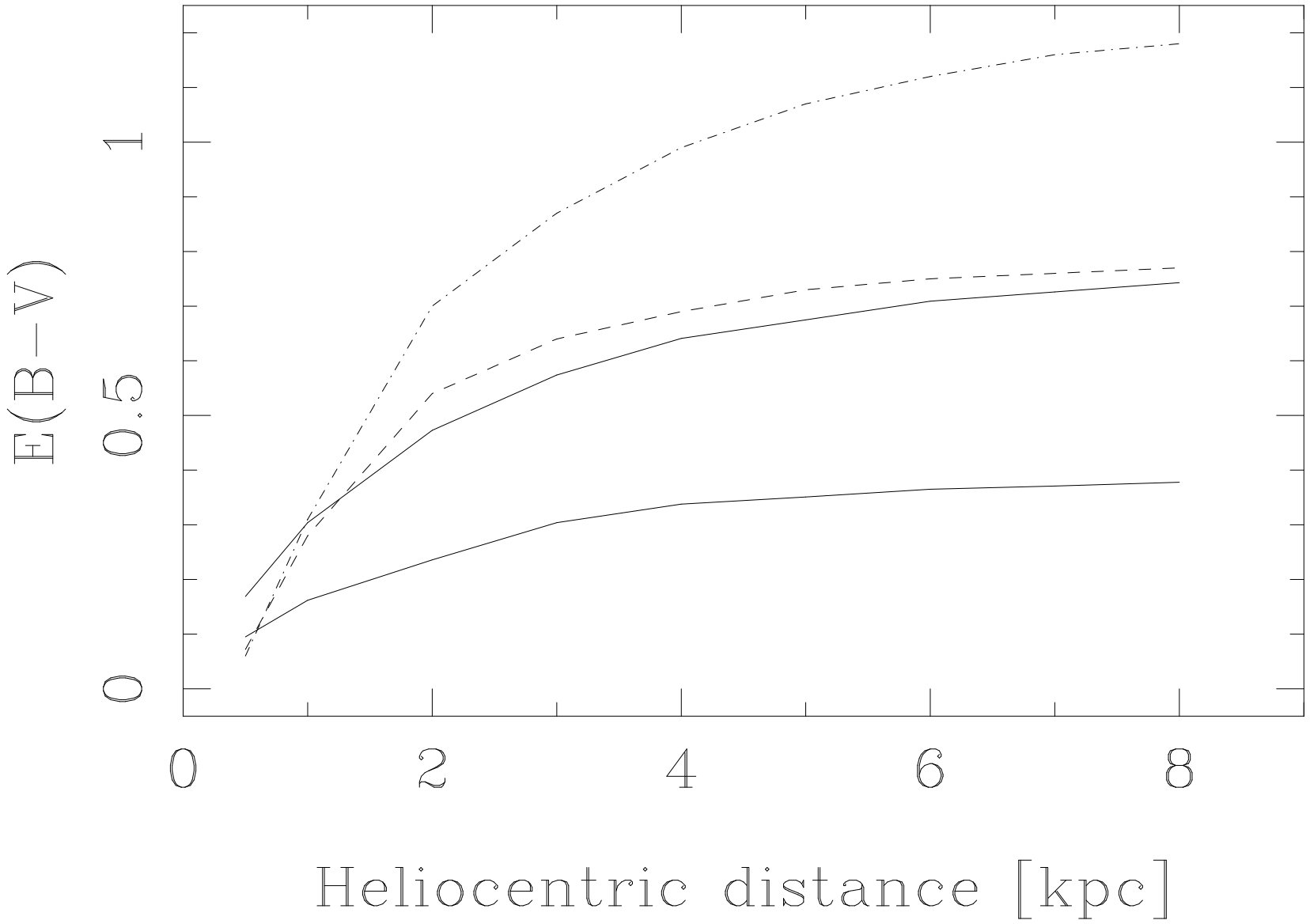
E(B−V)
0
0.5
1
0
2
4
6
8
Heliocentric distance [kpc]

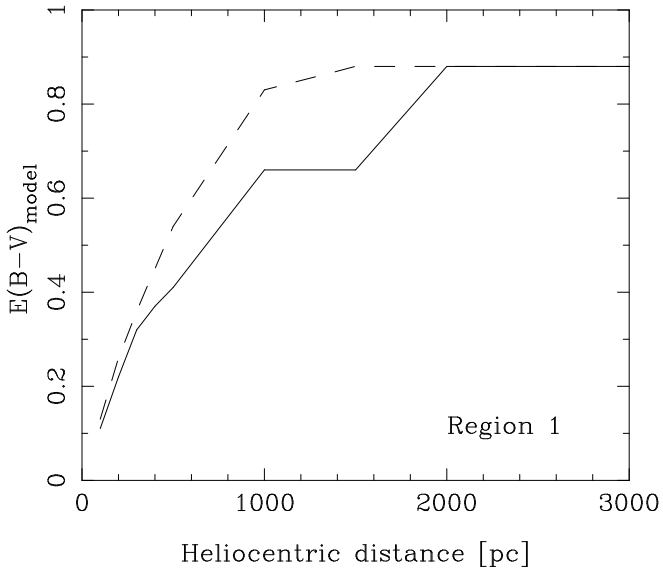
E(B−V)model
0
0.2
0.4
0.6
0.8
1
0
1000
2000
3000
Heliocentric distance [pc]
Region 1

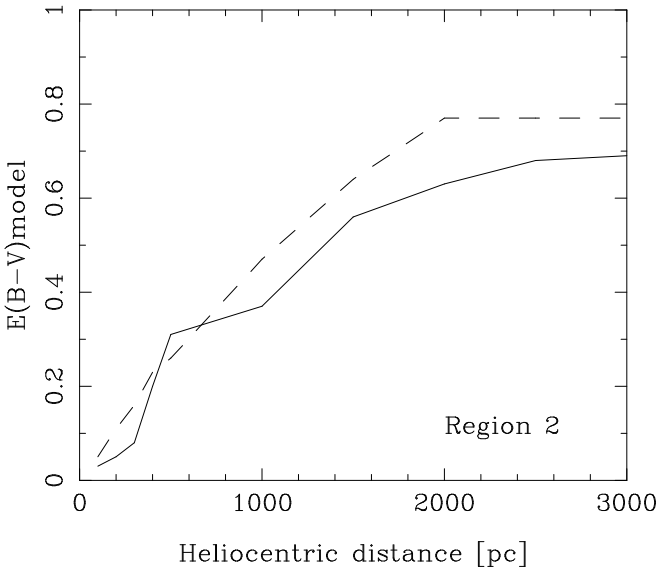
E(B−V)model
0
0.2
0.4
0.6
0.8
1
0
1000
2000
3000
Heliocentric distance [pc]
Region 2

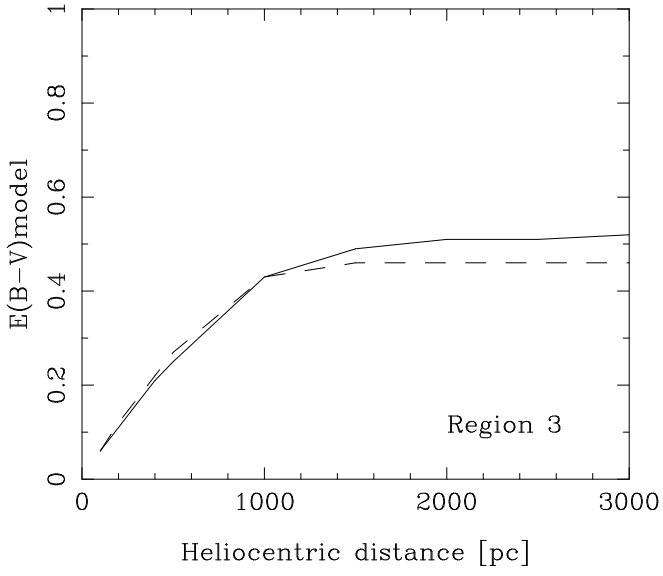
E(B−V)model
0
0.2
0.4
0.6
0.8
1
0
1000
2000
3000
Heliocentric distance [pc]
Region 3

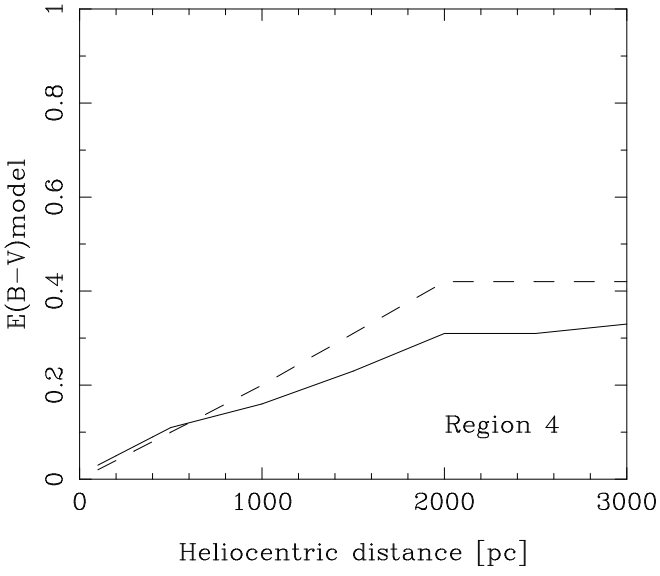
E(B−V)model
0
0.2
0.4
0.6
0.8
1
0
1000
2000
3000
Heliocentric distance [pc]
Region 4

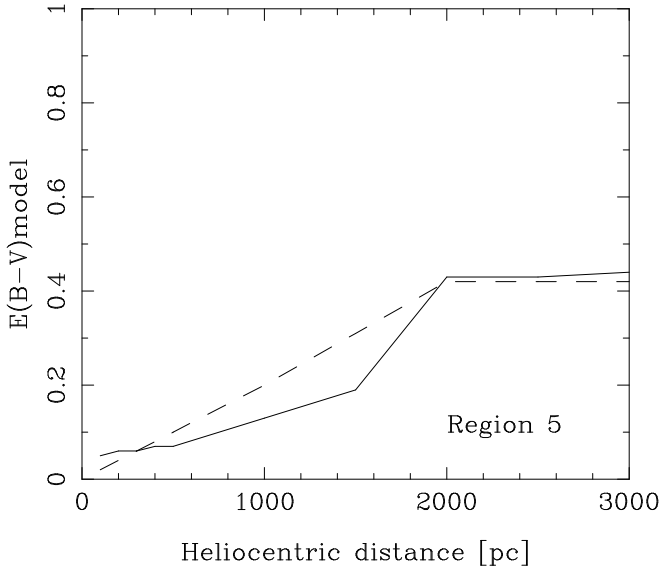
E(B−V)model
0
0.2
0.4
0.6
0.8
1
0
1000
2000
3000
Heliocentric distance [pc]
Region 5

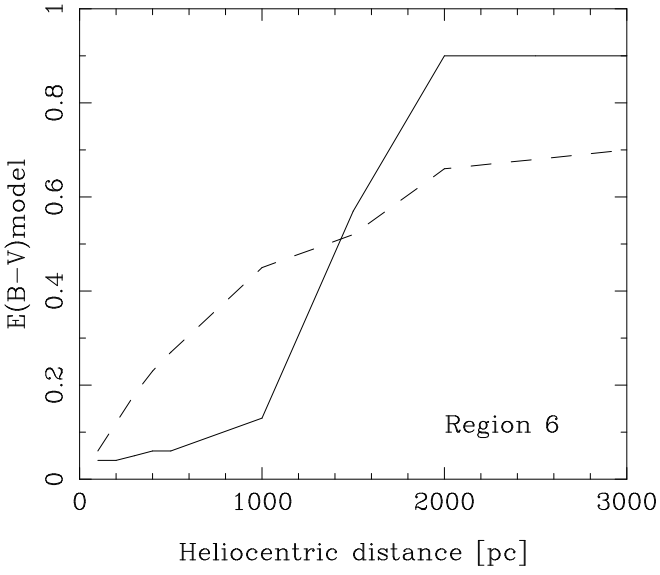
E(B−V)model
0
0.2
0.4
0.6
0.8
1
0
1000
2000
3000
Heliocentric distance [pc]
Region 6

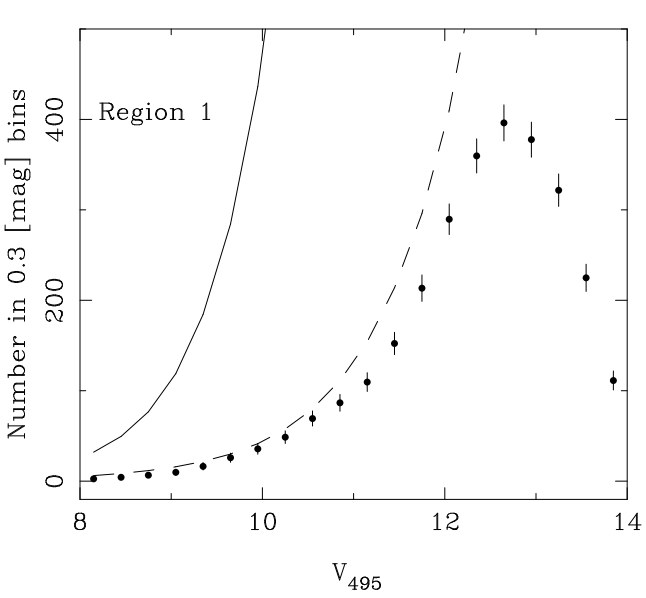
Region 1
Number in 0.3 [mag] bins
0
200
400
8
10
12
14
V495

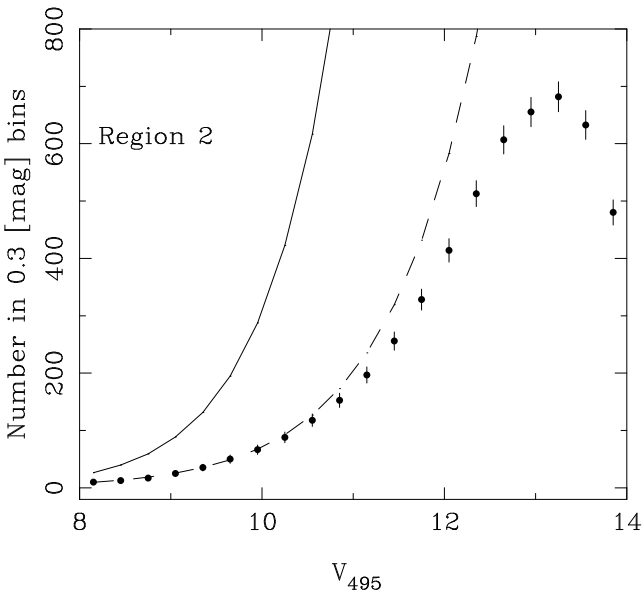
Region 2
Number in 0.3 [mag] bins
0
200
400
600
800
8
10
12
14
V495

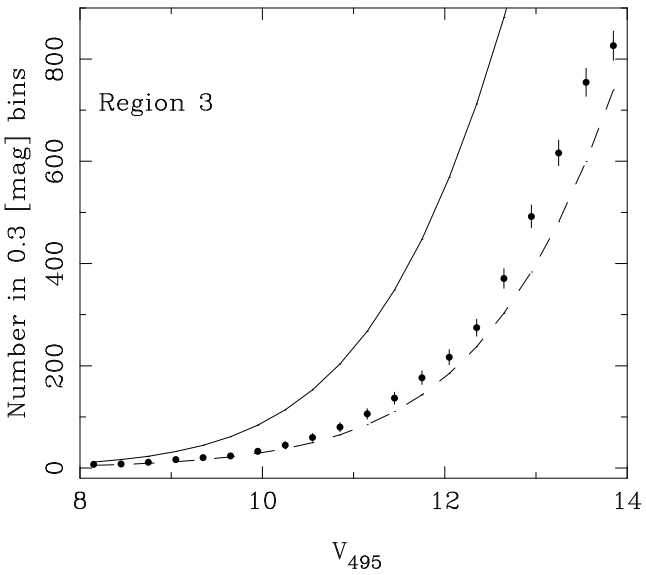
Region 3
Number in 0.3 [mag] bins
0
200
400
600
800
8
10
12
14
V495

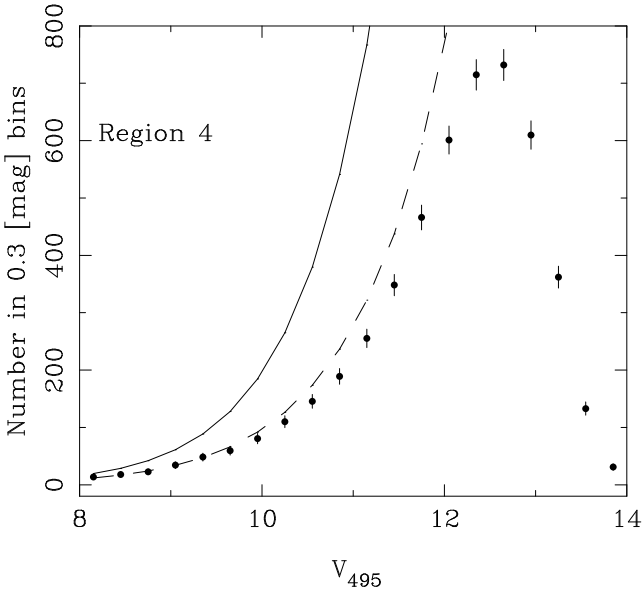
Region 4
Number in 0.3 [mag] bins
0
200
400
600
800
8
10
12
14
V495

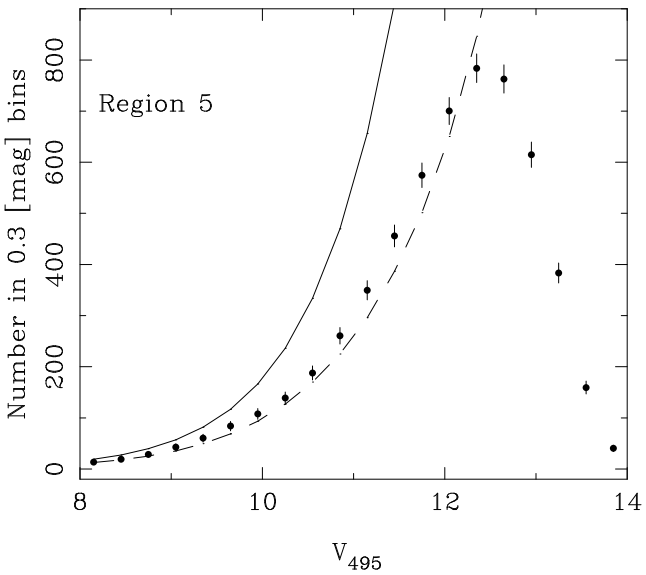
Region 5
Number in 0.3 [mag] bins
0
200
400
600
800
8
10
12
14
V495

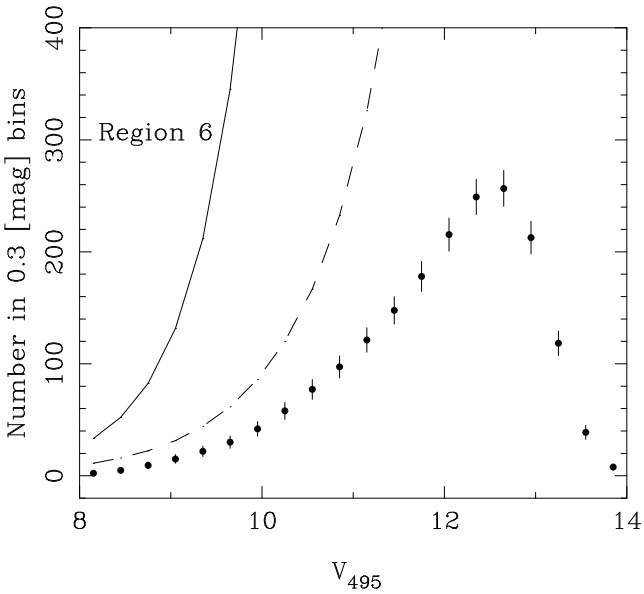
Region 6
Number in 0.3 [mag] bins
0
100
200
300
400
8
10
12
14
V495

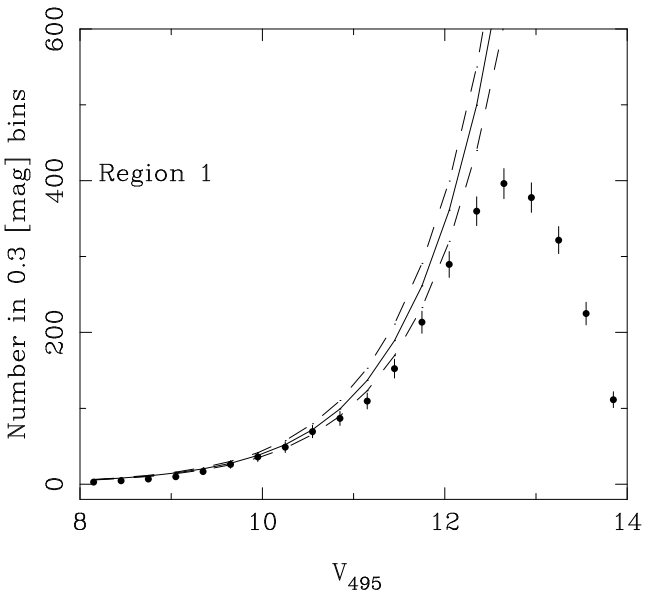
Region 1
Number in 0.3 [mag] bins
V_{495}

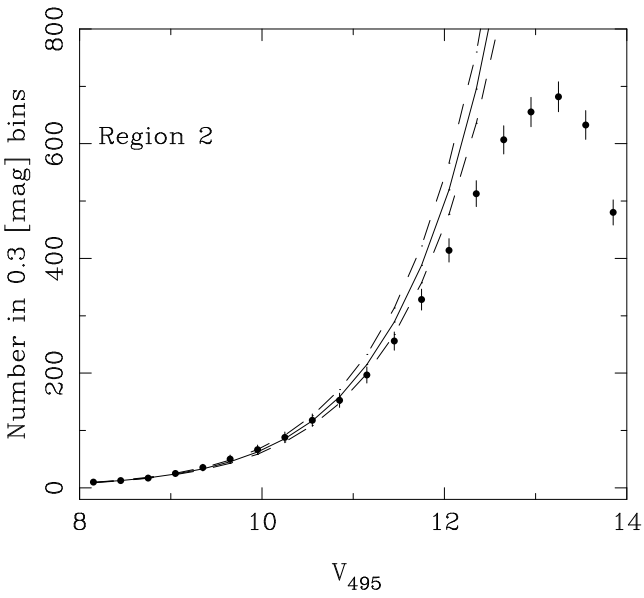
Region 2
Number in 0.3 [mag] bins
V_{495}

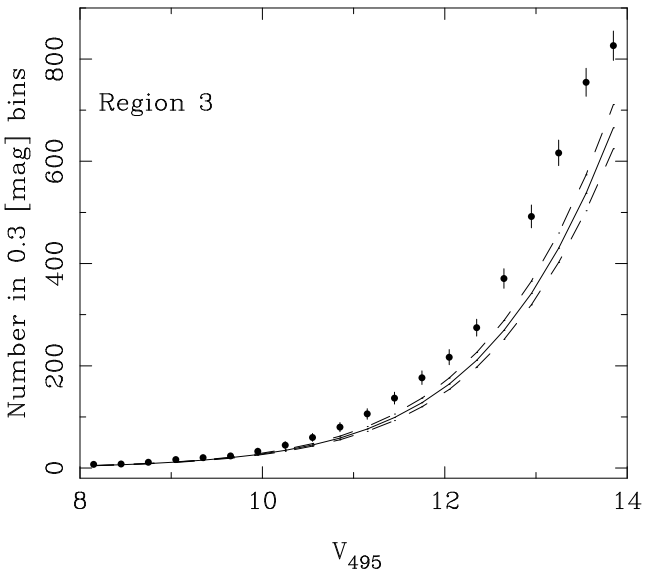
Region 3
Number in 0.3 [mag] bins
V_{495}

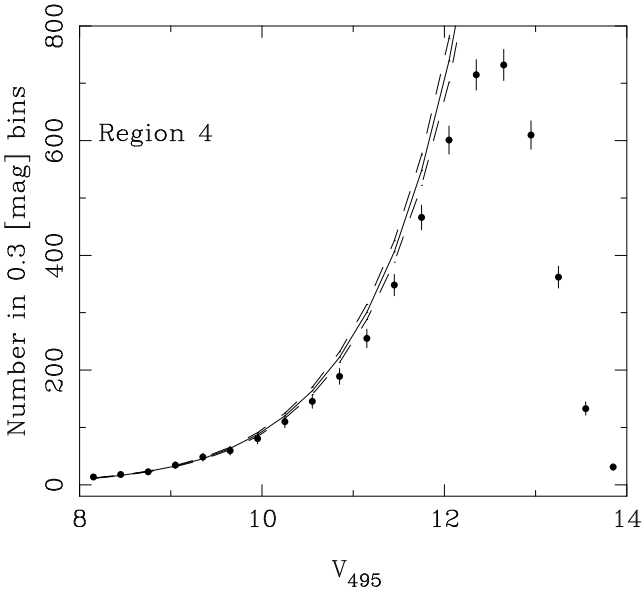
Region 4
Number in 0.3 [mag] bins
V_{495}

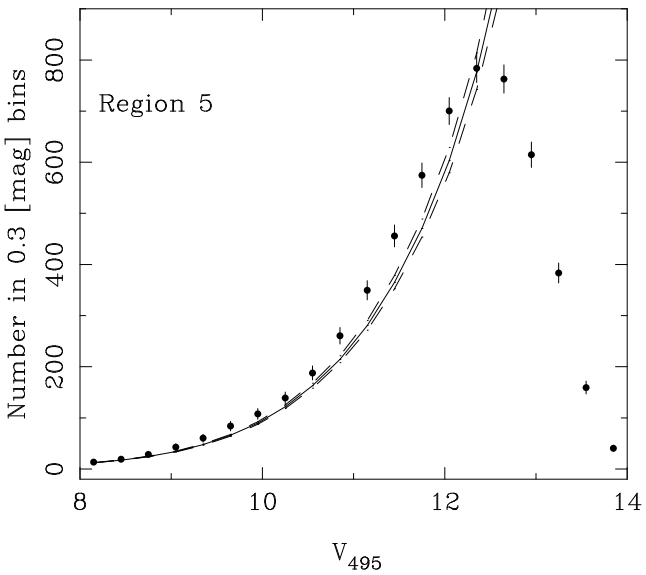
Region 5
Number in 0.3 [mag] bins
V_{495}

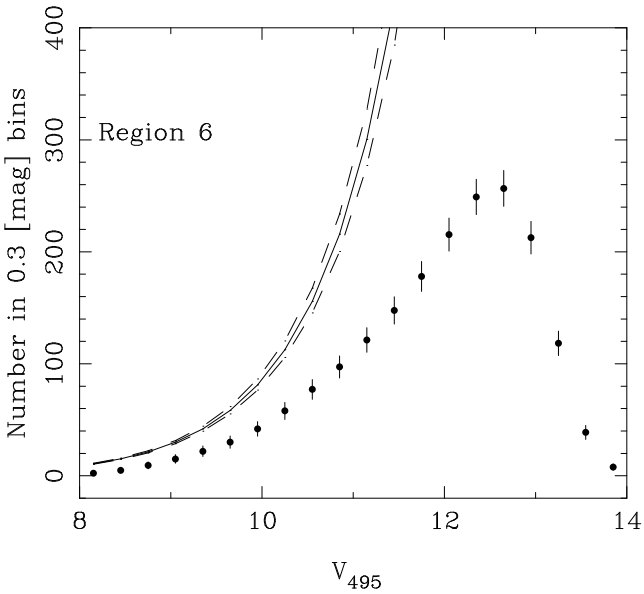
Region 6
Number in 0.3 [mag] bins
V_{495}

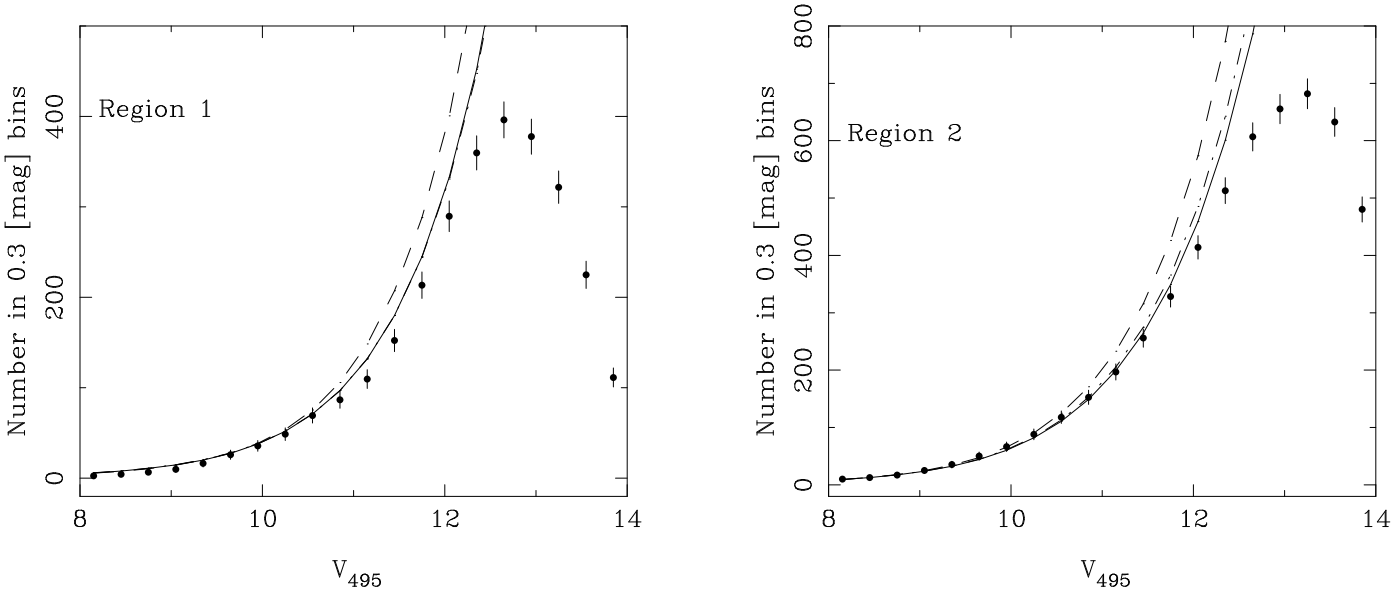
Region 1
Number in 0.3 [mag] bins
0
200
400
8
10
12
14
V495

Region 2
Number in 0.3 [mag] bins
0
200
400
600
800
8
10
12
14
V495

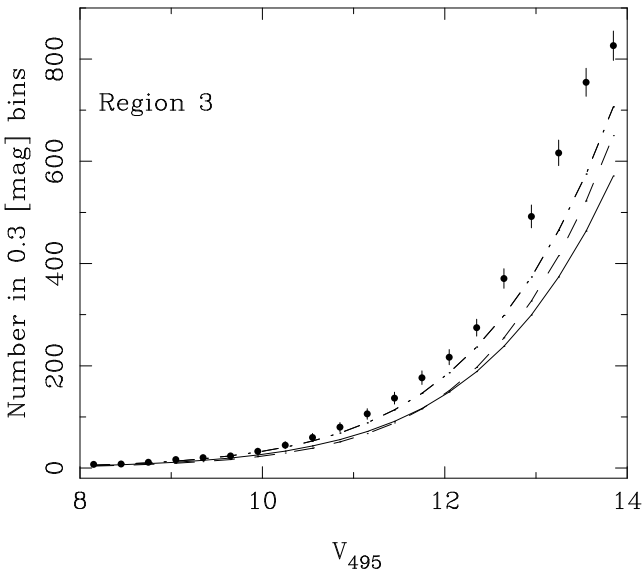
Region 3
Number in 0.3 [mag] bins
0
200
400
600
800
8
10
12
14
V495

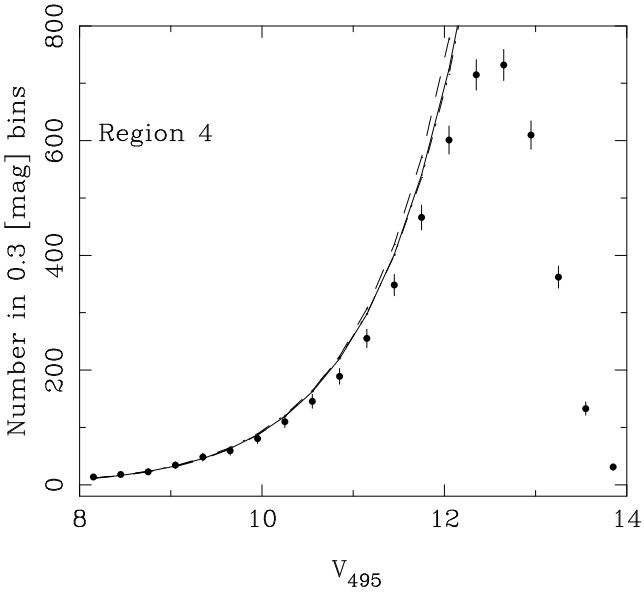
Region 4
Number in 0.3 [mag] bins
0
200
400
600
800
8
10
12
14
V495

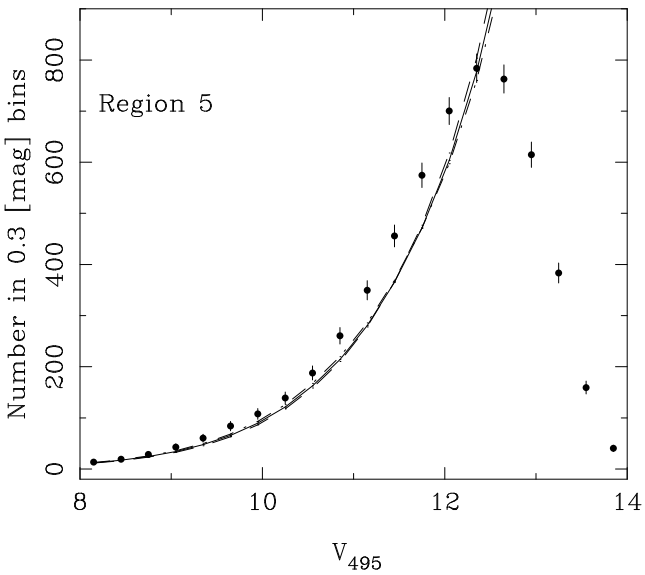
Region 5
Number in 0.3 [mag] bins
0
200
400
600
800
8
10
12
14
V495

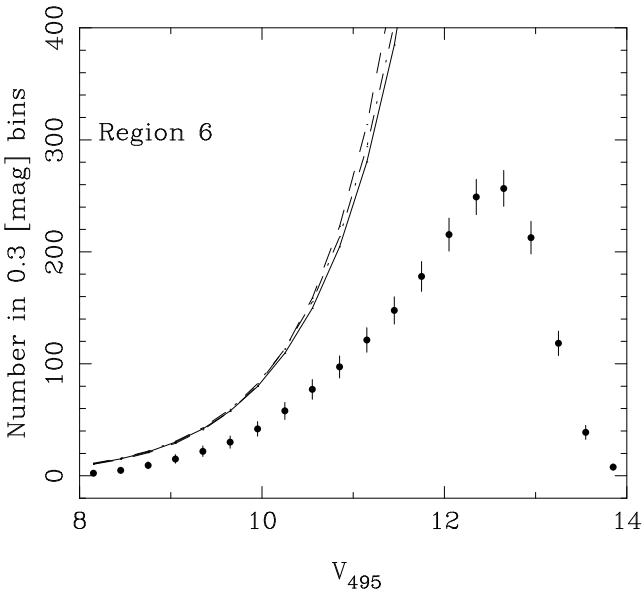
Region 6
Number in 0.3 [mag] bins
0
100
200
300
400
8
10
12
14
V495

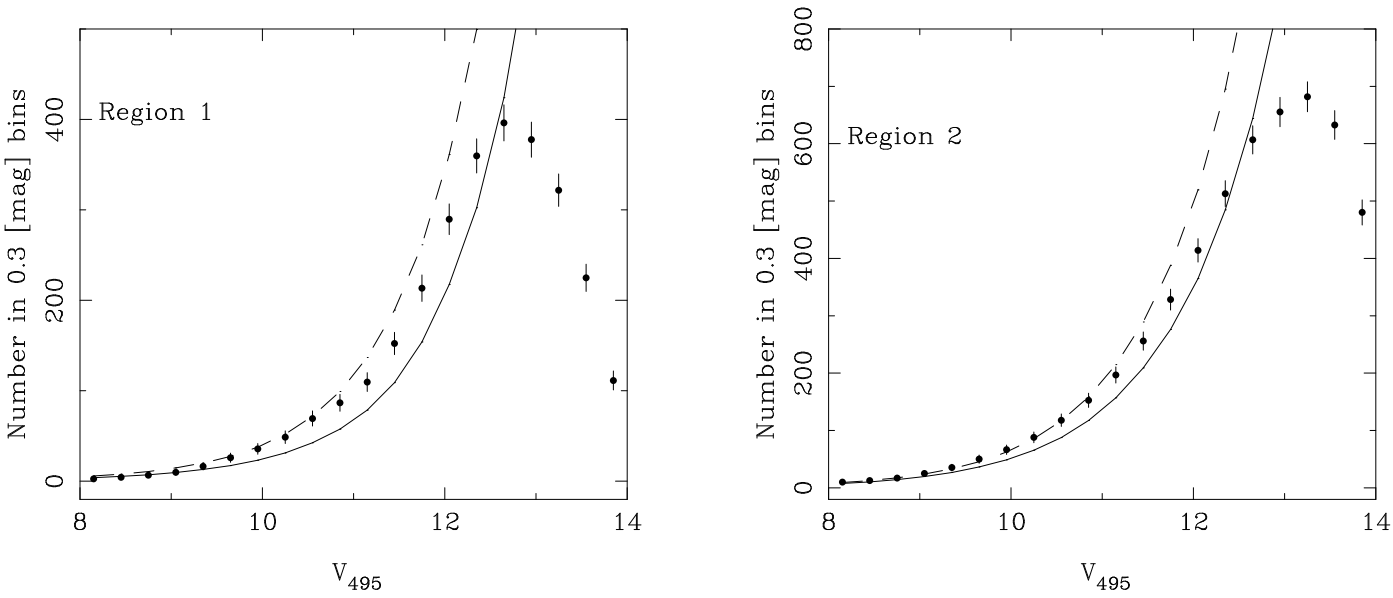
Region 1
Number in 0.3 [mag] bins
0
200
400
8
10
12
14
V495

Region 2
Number in 0.3 [mag] bins
0
200
400
600
800
8
10
12
14
V495

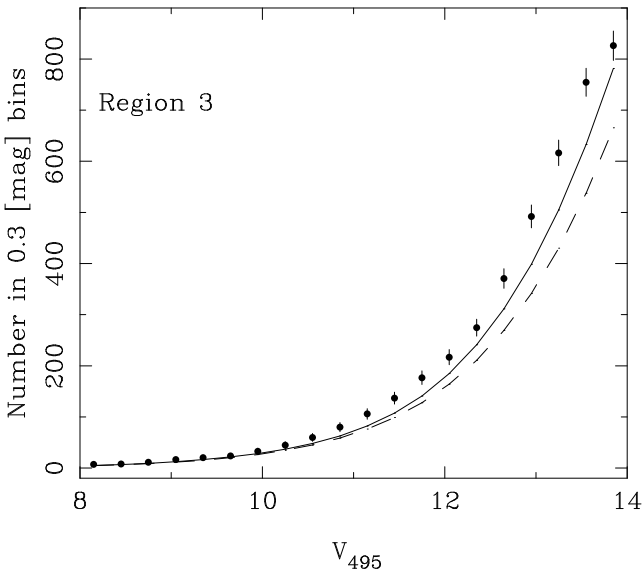
Region 3
Number in 0.3 [mag] bins
0
200
400
600
800
8
10
12
14
V495

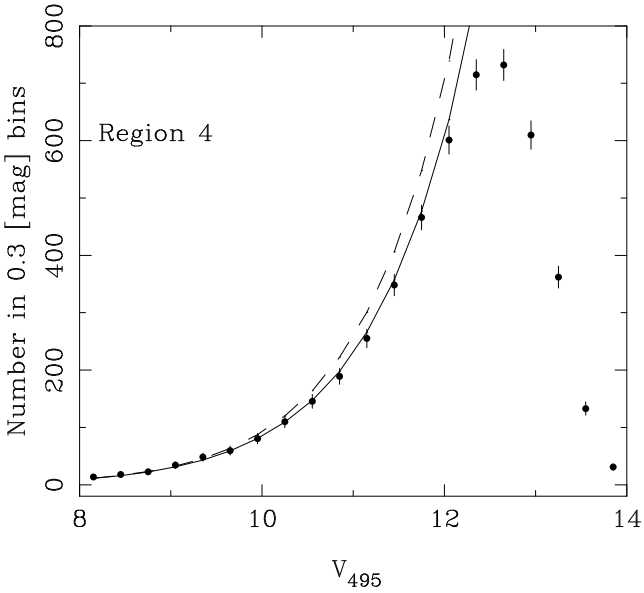
Region 4
Number in 0.3 [mag] bins
0
200
400
600
800
8
10
12
14
V495

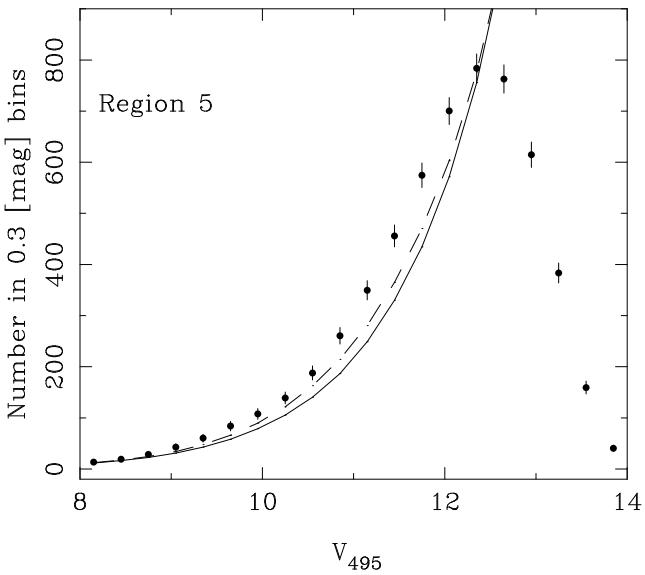
Region 5
Number in 0.3 [mag] bins
0
200
400
600
800
8
10
12
14
V495

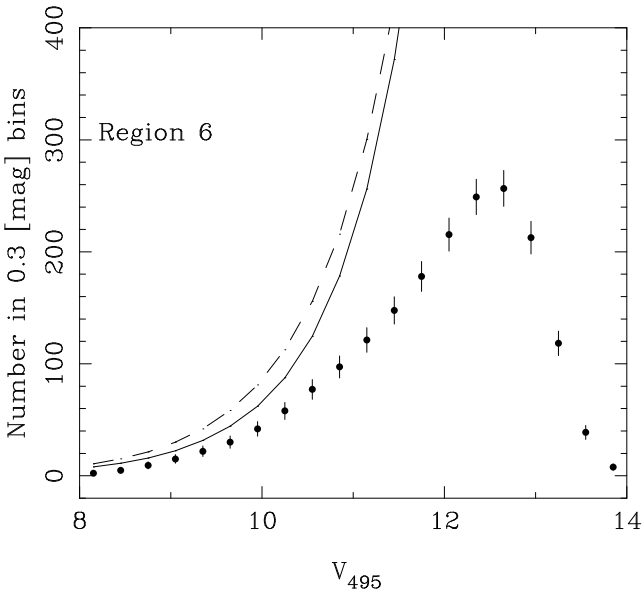
Region 6
Number in 0.3 [mag] bins
0
100
200
300
400
8
10
12
14
V495

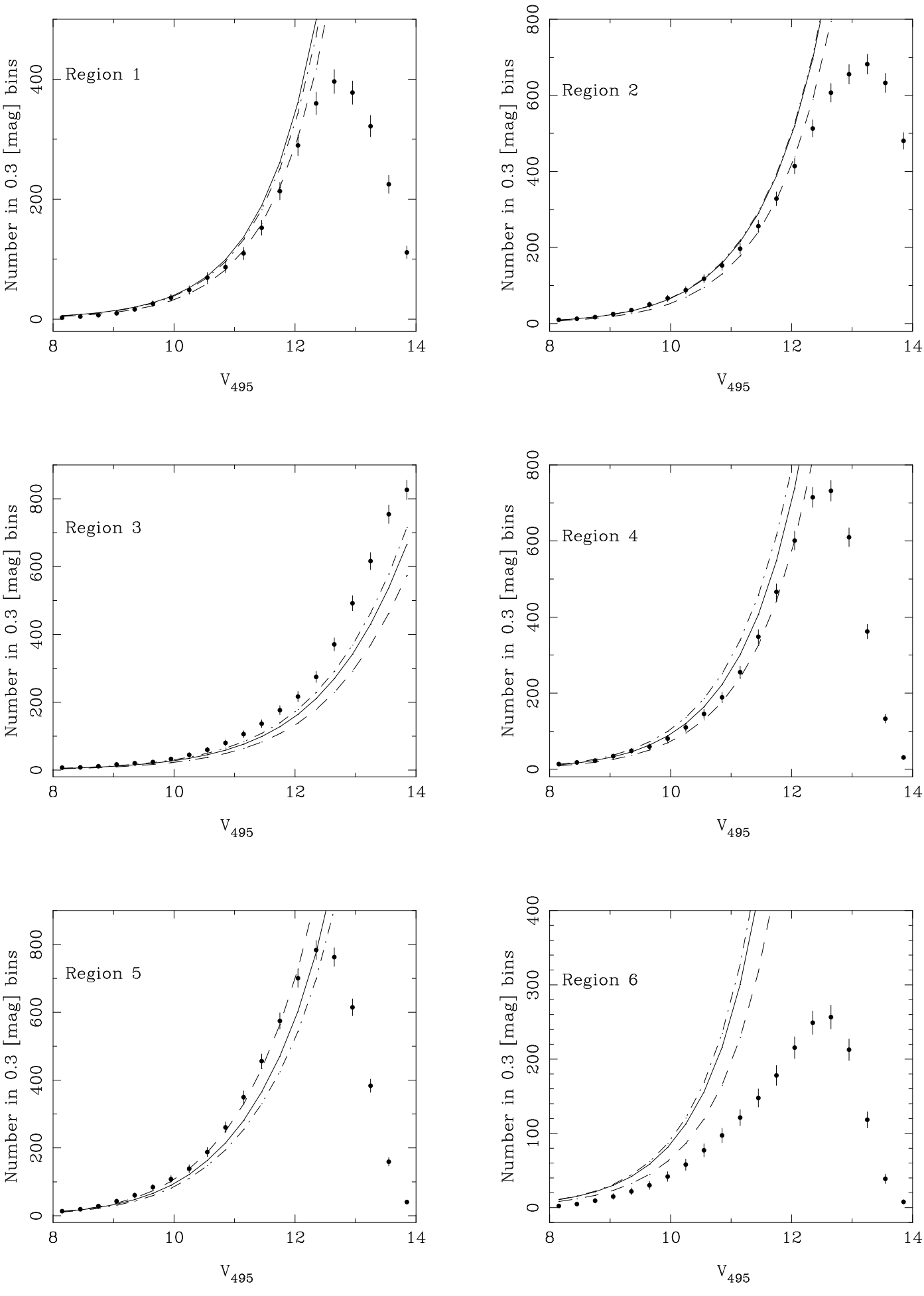
Region 1
Region 2
Region 3
Region 4
Region 5
Region 6
Number in 0.3 [mag] bins
V_{495}

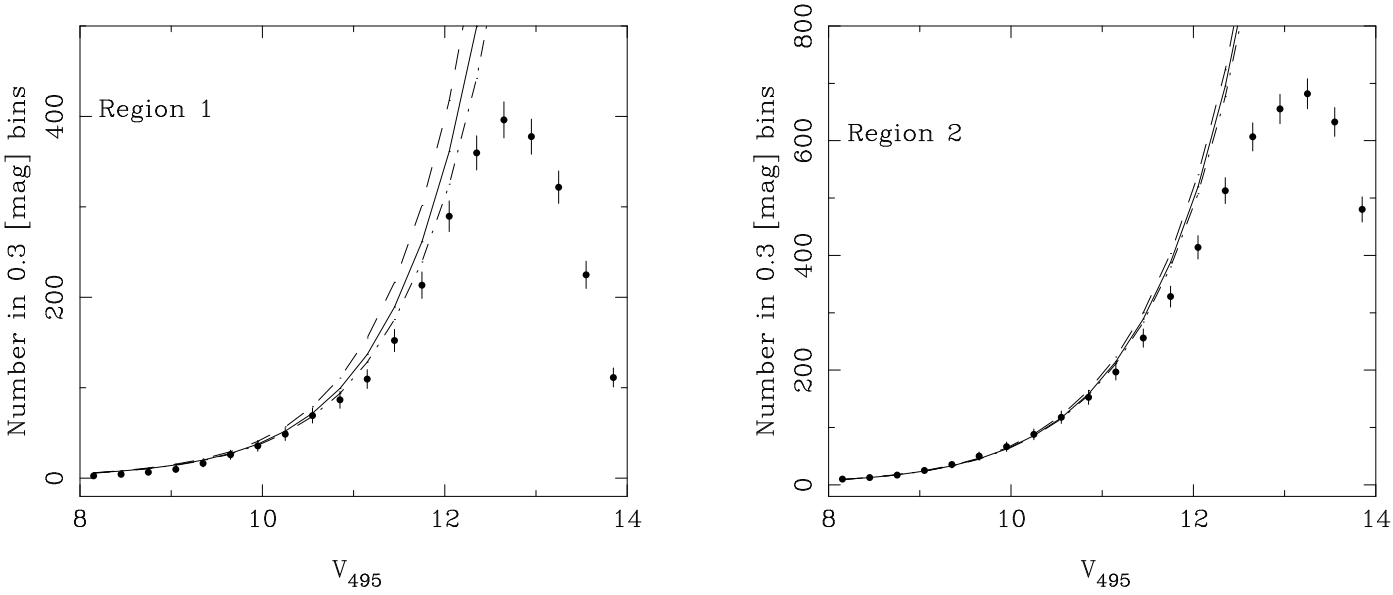
Region 1
Number in 0.3 [mag] bins
0
200
400
8
10
12
14
V495

Region 2
Number in 0.3 [mag] bins
0
200
400
600
800
8
10
12
14
V495

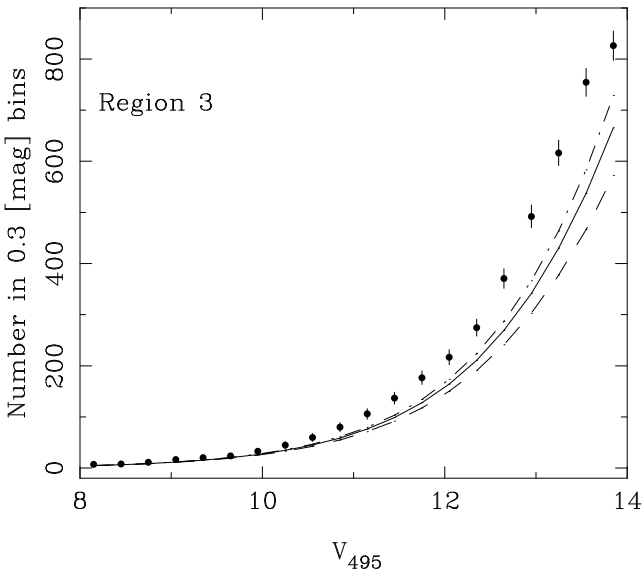
Region 3
Number in 0.3 [mag] bins
0
200
400
600
800
8
10
12
14
V495

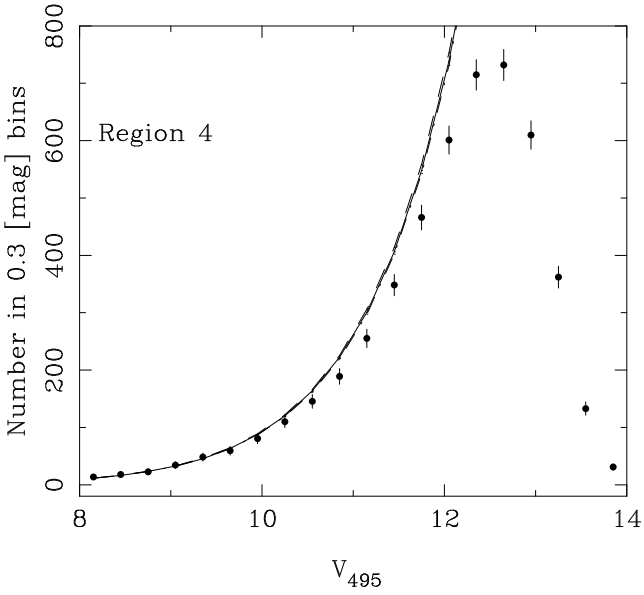
Region 4
Number in 0.3 [mag] bins
0
200
400
600
800
8
10
12
14
V495

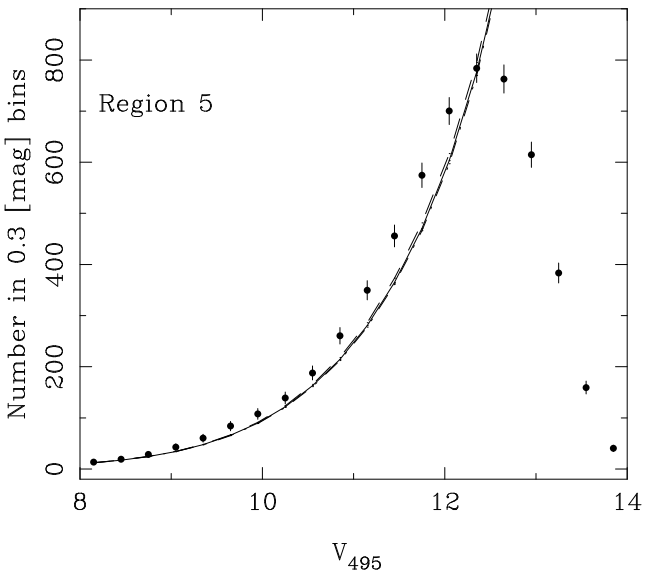
Region 5
Number in 0.3 [mag] bins
0
200
400
600
800
8
10
12
14
V495

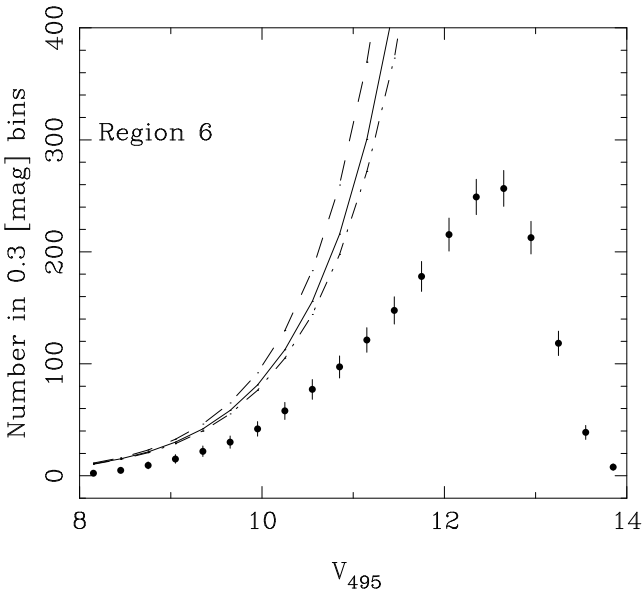
Region 6
Number in 0.3 [mag] bins
0
100
200
300
400
8
10
12
14
V495

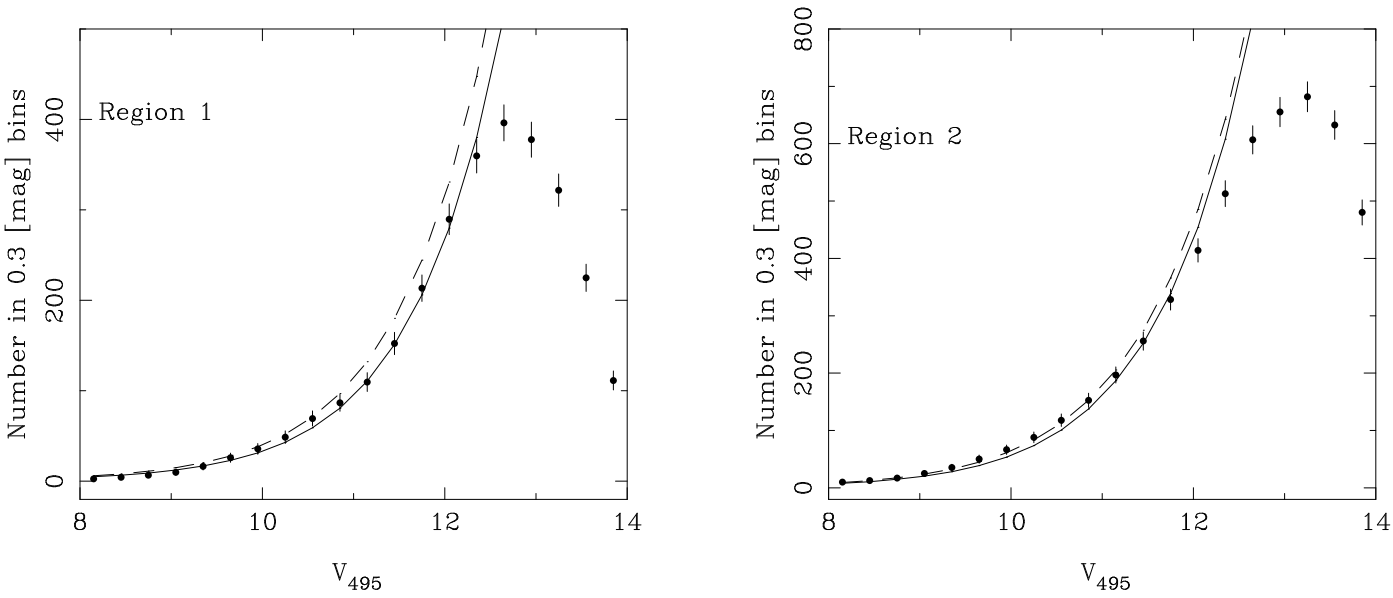
Region 1
Number in 0.3 [mag] bins
0
200
400
8
10
12
14
V_{495}

Region 2
Number in 0.3 [mag] bins
0
200
400
600
800
8
10
12
14
V_{495}

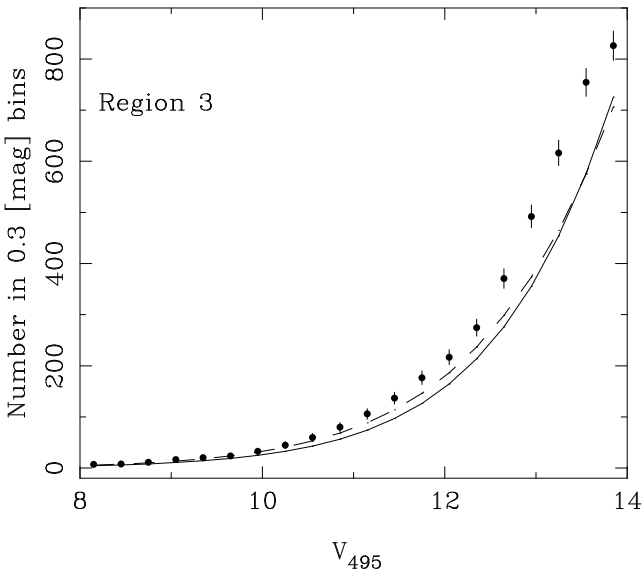
Region 3
Number in 0.3 [mag] bins
0
200
400
600
800
8
10
12
14
V_{495}

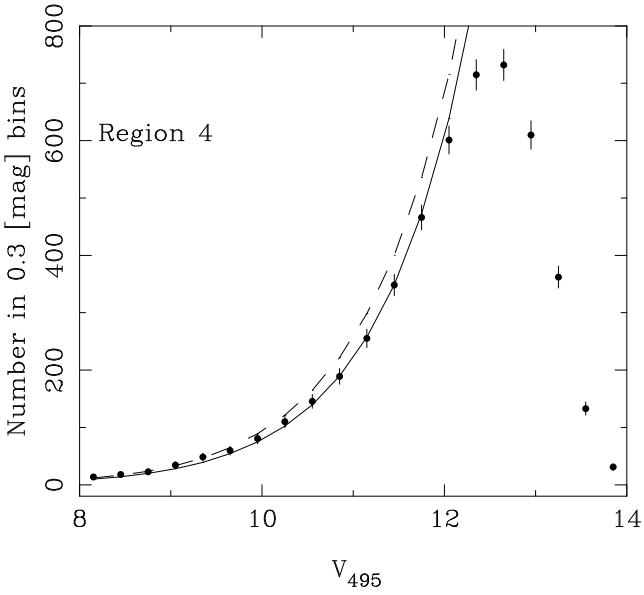
Region 4
Number in 0.3 [mag] bins
0
200
400
600
800
8
10
12
14
V_{495}

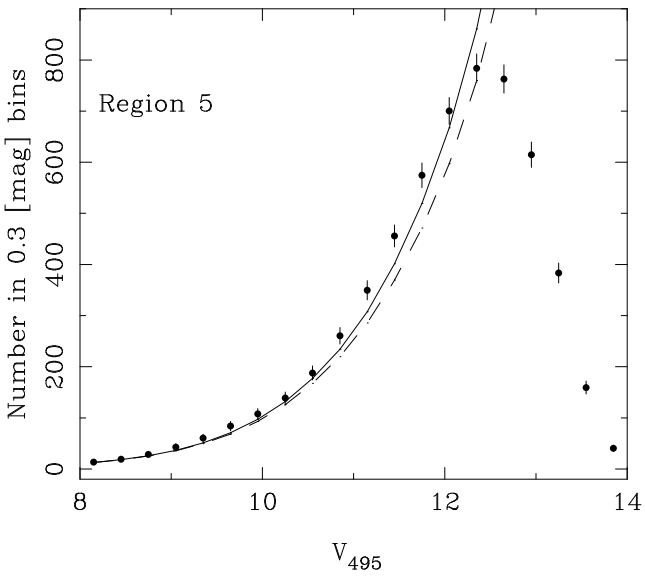
Region 5
Number in 0.3 [mag] bins
0
200
400
600
800
8
10
12
14
V_{495}

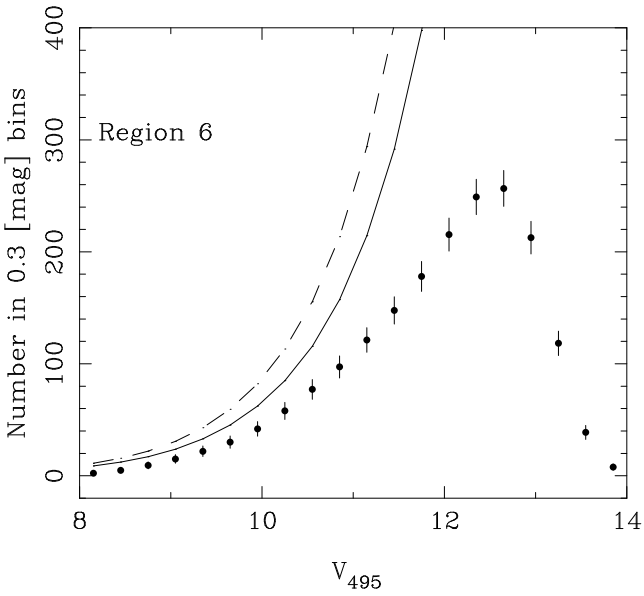
Region 6
Number in 0.3 [mag] bins
0
100
200
300
400
8
10
12
14
V_{495}

This figure "ramfig3.gif" is available in "gif" format from:

http://arXiv.org/ps/astro-ph/9710030v1

This figure "ramfig10.gif" is available in "gif" format from:

http://arXiv.org/ps/astro-ph/9710030v1